Lime - Alumina - Silica Ceramic Processing Incorporating Wollastonite ($CaO \cdot SiO_2$)

by

Raymond Herbert Bryden

A Thesis Submitted to the Faculty of Engineering in Partial Fulfillment of the Requirements for the Degree of

DOCTOR OF PHILOSOPHY

Major Subject: Metallurgical Engineering

TECHNICAL UNIVERSITY OF NOVA SCOTIA

Halifax, Nova Scotia

1996

TABLE OF CONTENTS

LIST OF TABLES

LIST OF FIGURES

LIST OF ABBREVIATIONS AND SYMBOLS

Abbreviations

APE	anionic polyelectrolyte
CAS	lime (Calcium) aluminosilicate C = calcia, calcium oxide, CaO A = alumina, aluminum oxide, Al_2O_3 S = silica, silicon dioxide, SiO_2
CIP	cold isostatic pressing
CPE	cationic polyelectrolyte
CTE	coefficient of thermal expansion
CVD	chemical vapour deposition
DLVO	Derjaguin, Landau, Verwey and Overbeek theory
DTA	differential thermal analysis
EDS	energy dispersive spectroscopy
F*A*C*T	Facility for the Analysis of Chemical Thermodynamics
FWHM	full width at half maximum
HIP	hot isostatic pressing
HP	hot pressing
LAS	lithium aluminosilicate
LPS	liquid phase sintering
MOR	modulus of rupture
MW	(average) molecular weight
PC	personal computer
PVD	physical vapour deposition
RLPS	reactive liquid phase sintering
SEM	scanning electron microscope
SENB	single edge notched beam
SSS	solid state sintering
TD	theoretical density

TGA	thermogravimetric analysis
VGS	viscous gas sintering
XRD	X-ray diffraction

variables

%TD	percent theoretical density; [%]
η	apparent viscosity, viscosity; [mPa·s]
Ψ	potential at distance r; [V]
γ	shear rate; [s^{-1}]
ζ	zeta potential; [V]
Ψ_s	potential at surface; [V]
η_V	Vickers indentor geometric constant
η_{water}	viscosity of water; [mPa·s]
Ψ_z	potential at slip plane, zeta potential; [V]
α	coefficient of linear thermal expansion; [m/mK]
a	indent radius (half of "d"; center-to-corner); [m]
a	particle radius; [m]
c	crack length, (center of indent to end of crack); [m]
c	defect size; [m]
d	height of suspension; [m]
d	square indent diameter (corner-to-corner); [m]
dM/dT	change in mass per change in temperature; [g/C]
ΔT	change in temperature; [C]
e	elementary proton charge; [Coulombs]
E	Young's modulus, elastic modulus; [GPa]
Φ	volume fraction
Φ_s	volume fraction solid

g, G	gravitation constant; [m/s^2]
H	hardness; [GPa]
h	sediment height; [m]
H	suspension height before sedimentation; [m]
H_V	Vickers hardness; [GPa]
I	weight when immersed in fluid; [g]
J_{water}	water transport flux
k	Boltzmann constant
K_c	critical fracture toughness (indentation); [$MPa \cdot m^{1/2}$]
K_{Ic}	critical fracture toughness (mode I); [$MPa \cdot m^{1/2}$]
L_{crit}	critical contact load; [N]
ν	Poisson's ratio
n_i	number of ions per unit volume at distance r
n^o_i	number of ions per unit volume at distance ∞
P	load; [N]
p_{crit}	critical indent or groove size; [m]
P_m	pressure at mold surface
P_s	pressure in suspension
θ	X-ray beam angle; [°]
ρ	density; [g/cc] or [%]
r	distance from particle surface; [m]
R	thermal shock parameter; [C] or [K]
$\rho_{alumina}$	density of alumina; [g/cc]
ρ_{bulk}	bulk density; [g/cc]
ρ_{green}	green density; [g/cc] or [%]
ρ_{LPS}	density after liquid phase sintering; [g/cc] or [%]
$\rho_{mercury}$	density of mercury; [g/cc]
ρ_{TD}	theoretical density; [g/cc] or [%]
ρ_{water}	density of water; [g/cc]

σ	stress; [MPa]
σ_c	compressive strength; [MPa]
σ_t	tensile strength; [MPa]
T	temperature; [C] or [K]
t	time, casting time; [s]
V_{int}	energy; [$kg \cdot m^2/s^2$]
V_s	solid volume fraction
W	weight in air; [g]
x	thickness; [m]
z_i	valence of ion i

ACKNOWLEDGMENTS

The author wishes to thank all those who helped, directly and indirectly, in the completion of this project. This includes the Natural Sciences Engineering and Research Council (NSERC) who supplied the funding. Special thanks to my supervisor, Dr. William Caley for his patience, guidance and input. I also wish to thank my friends, Dana Goski, Dr. Kris Konsztowicz, Paul Bishop, John MacLean, Brent Annesty, Lucy Kanary, Bob MacKay, Jean Merritt, Heather Koeller, Cyril Cole, Bill McManus, and Art Marshall as well as the long list of professors in the Mining and Metallurgy department at TUNS for their help throughout this project.

I also wish to acknowledge the efforts of the Advanced Materials Engineering Center (AMEC), the Dentistry Department of Dalhousie University, and Paul Kingston (Ontario Ministry of Northern Development and Mines).

Finally, I thank my family, Domenica Tatasciore, and her family for their help, generosity, and hospitality.

ABSTRACT

Improvements in mechanical and physical properties of advanced ceramics have been undermined by high processing costs and the reputation of unpredictable reliability, resulting in limited use of these materials in technical, industrial, and recreational applications. It was felt that a lower cost ceramic with desirable properties would open up new areas of application, traditionally dominated by hard or temperature-resistant metals. One potential technique was to use a naturally occurring mineral to develop new ceramic microstructures using a simple processing technique, reducing both raw material and production costs. The system chosen for potential development was an alumina (Al_2O_3) ceramic modified using 20 wt% naturally occurring wollastonite ($CaO{\cdot}SiO_2$). Green body production was carried out using wet processing which was optimized using rheology; the best conditions were found to be a pH of 3.0 using 1500 ppm of BETZ 1190 (dispersant) processed at about 0.35 volume fraction solids in a water-based suspension. Thermal analysis techniques revealed that the best sintering technique involved liquid phase sintering for fifteen minutes at 1500 C, followed by an air quench. This glass-ceramic was then devitrified using a heat treatment of 1032 C for 4 h followed by 1200 C for 4 h. The resulting structure, 68 wt% (60 vol%) alumina, with the remainder consisting of gehlenite and anorthite, had high indentation toughness (4.8 $MPa\sqrt{m}$) and a bend strength of 120 MPa; properties which lend it to economical anti-abrasion applications.

1. INTRODUCTION

1.1 Ceramics - General

The use of ceramics is important in many applications where high temperatures or aggressive chemical environments are encountered. Most ceramics possess high strength (particularly at elevated temperatures in contrast to other materials) but are inherently very brittle. This does not imply that a ceramic material is not strong but that when the fracture stress is exceeded it breaks without requiring any extra deformation energy.[1] New research has investigated numerous methods to enhance ceramic toughness, including fibre, whisker or particulate reinforcement, transformation toughening (ZrO_2), and microcrack toughening (generated by thermal mismatch).[2] Some ceramics incorporate a glassy phase at grain boundaries which fails preferentially when a crack approaches, setting up enhanced toughness due to higher fracture surface area, fibre pull-out or crack bridging phenomena.[3] Often, combinations of ceramic toughening methods are investigated using different materials having different properties. New applications for ceramic materials include wear, corrosion or heat resistant coatings and electronic substrates (due to their low dielectric constants, high dielectric strength, and thermal properties).[4-8]

Ceramics as a class of material include a wide range of materials covering a broad spectrum of properties. Some general properties of these inorganic non-metallics are well established. A summary of some of the advantages and disadvantages of ceramic-based materials follows (Table 1-1):

Table 1-1. Advantages and limitations of ceramics.[4]

Advantages	
High melting point	Good dielectric properties
High stiffness	Thermal/electrical insulators
High hot strength	Semiconductor properties
High compressive strength	Ion-conductor properties
High hardness	Magnetic properties
Wear and corrosion resistance	Biocompatibility
Low density (lightweight)	Abundant raw materials
Limitations	
Susceptible to thermal and mechanical shock	
Gaps in understanding and experience	
Difficult to fabricate	
Poor reproducibility	
High cost	

The large barrier to common use of reinforced or "toughened" ceramics is the high price of materials (some whisker or fiber reinforcements can cost hundreds of dollars per kilogram; see Table 1-2) so an interest has developed [9,10] in incorporating low cost minerals into common ceramics in an attempt to achieve better mechanical or physical properties at a lower cost. The mineral chosen for this study is wollastonite ($CaO{\cdot}SiO_2$ or $CaSiO_3$) [11-14] due to its abundance, availability and relatively low cost (a few dollars per tonne, depending on degree of beneficiation).[9,13] The best choice for matrix material was alumina (Al_2O_3) for similar reasons but also because of the large quantity of research performed over the past 50 years; its properties are very well known, and it is

currently used in many high temperature [4,7,14] and electronic applications [7].

Table 1-2. Properties and price of various ceramic fibres.[4]

Fibre	Type	Tensile Strength [GPa]	Elastic Modulus [GPa]	Density [g/cm^3]	Approx. Cost ['94 $Cdn/kg]
E Glass	Silicate glass	1.7 -3.5	69 - 72	2.55	5
Torayca T300	Carbon	3.53	230	1.76	90
Torayca M40	Carbon	4.41	547		170
Saffil	Alumina	1 - 2	300	3.3	170
Nextel 440	Aluminosilicate	2.07	186	3.05	300
FP Alumina	Alumina	1.38 - 2.10	379	3.95	1000
Nicalon	SiC	2.45 - 2.94	177 - 196	2.55	1400
Tyranno	SiC	2.74	206	2.35	1400

The aim of ceramic processing, in general, and wet processing, in particular, is to reduce the maximum defect size and overall number of defects present. This is important since the Griffith equation states [4,15],

$$\sigma \propto K_{Ic} c^{-1/2} \qquad (1\text{-}1)$$

where c is the maximum defect size, K_{Ic} the fracture toughness, and σ the fracture strength. Thus, if the defect size is reduced, the fracture strength increases.

Optimisation must be carried out on the wet processing before a homogenous product with few or no defects can be guaranteed. This type of testing usually incorporates a rheometer to measure the rheological properties of the ceramic powder suspension (also

called a slurry or slip). The prime variable being monitored is the suspension viscosity, since, in general, at a given solid/liquid concentration a high quality slip has low apparent viscosity and can be easily poured into a plaster mold for consolidation into a green body. Commonly, a high viscosity slurry implies that the suspension conditions are causing the ceramic particles to stick together (flocculation) which tends to produce a porous and undesirable green body when cast. Variables which affect dispersion/flocculation include pH, solids content, and the presence of a polymeric dispersant.

A suspension dispersed only by pH adjustment is said to be electrostatically stabilised; by polymeric dispersant alone, sterically stabilised; and by a combination of both, electrosterically stabilised.[4] Once a green body is optimised, the next step is to sinter the body at high temperatures to reach full density.

Most sintering methods involve only solid state diffusion processes to eliminate pores and to control grain size. Liquid phase sintering (LPS) has some advantages in that the presence of a liquid will dramatically increase mass transport rates (thus densification) and can produce elongated or plate-like grains in the case of alumina.[16-23] The main disadvantage is that during the cooling stage, the liquid will tend to form a glass instead of a more stable crystalline phase, due simply to kinetic barriers.

Crystallisation of a glass, or devitrification, can be accomplished by a heat treatment procedure whereby the material is heated to a temperature at which crystal nuclei form within the glass; once nucleated, the glass may then be heated to a temperature at which crystal growth is strongest. This technique is common in glass-ceramic materials and can

virtually eliminate all glass in the microstructure.[24-26] Also, LPS is limited to 20-25 vol% liquid before structural rigidity is lost and the pre-cast shape forms a semi-solid puddle.[27]

Phase diagrams and thermodynamics software packages, such as the Facility for Analysis of Chemical Thermodynamics (F*A*C*T) can aid in predicting the amount of liquid phase present during sintering.

1.2 CAS Ceramics

One of the most useful ceramic systems involves various combinations of lime, alumina and silica. Thus, it is useful to outline some of the characteristics of each of these components.

1.2.1 Silica (SiO_2)

Silica is the most abundant material in the earth's crust [14], and is most often related to glassy materials and refractories. Silica has many crystallographic forms but the most common is α-quartz which is the phase stable at lower temperatures. Most quartz used for ceramics is beneficiated from sandstone which consists of lightly bonded quartz grains.[28]

The atomic structure of silica is a network of SiO_4 tetrahedra (Figure 1-1), and it may form stable crystalline forms (Figure 1-2a), such as quartz, or may develop into a random

arrangement (no long-range order), which is collectively known as glass (Figure 1-2b). The crystalline forms are very stable in thermally and chemically aggressive environments. Glassy silica-based materials are useful as optical materials or where very low thermal expansion is required.[29]

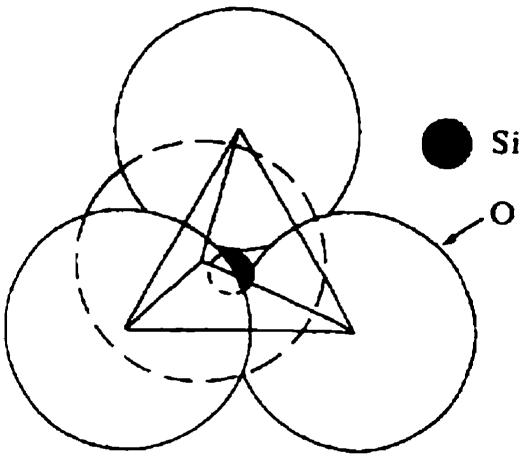

Figure 1-1. Schematic view of a $(SiO_4)^{4-}$ tetrahedron.[29]

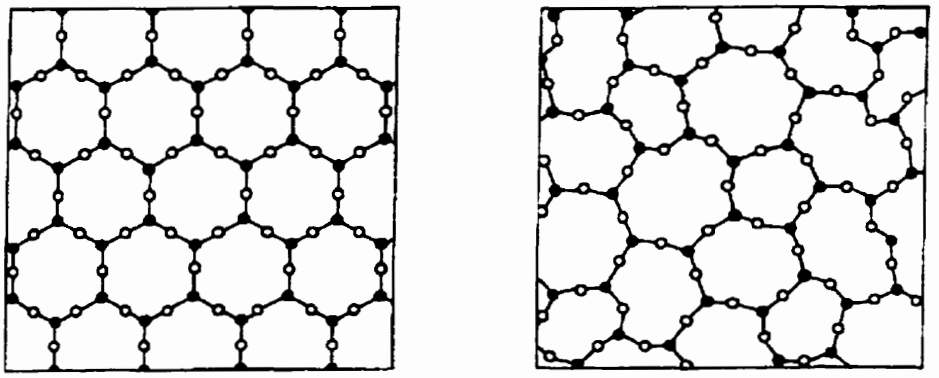

Figure 1-2. Two dimensional diagrams showing SiO_2 as (a) crystalline and (b) amorphous structures.[29]

1.2.2 Lime (CaO)

Lime (sometimes referred to as quicklime) is an oxide with strongly alkaline properties. It is often used as a flux in steelmaking, in glassmaking, and in neutralising acidic water.[14] Lime can also be used as an insecticide and as an industrial alkaline earth addition.[30] Although it is not a naturally occurring oxide (it is produced by calcination of limestone ($CaCO_3$)) its abundance is testimony to its many industrial applications. Other sources of the oxide, such as wollastonite, are sometimes used when alkali additives are required in an industrial process.

Calcium oxide has a cubic crystal of the sodium chloride structure (Figure 1-3). With a melting point of 2590 C, its low cost, and chemical stability in contact with metals, it is well suited for high temperature metallurgy. A great limitation is its reactivity with water which limits use of pure lime refractories, but this problem is most often abated by using

MgO additions to stabilise the material.[31]

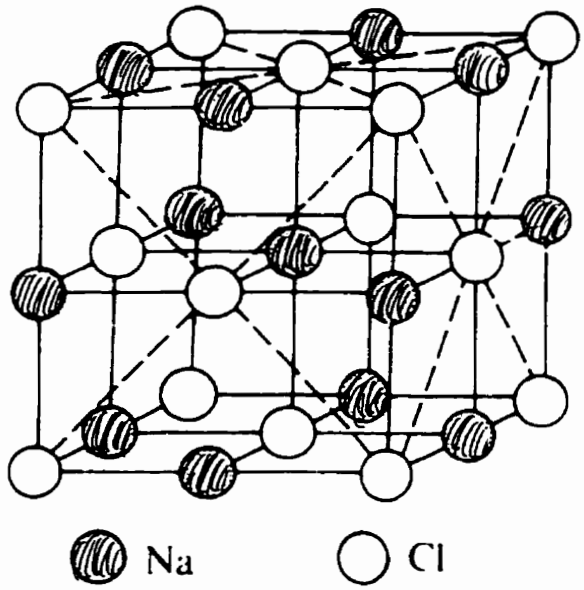

Figure 1-3. Unit cell of NaCl which corresponds to the structure of CaO.[29]

1.2.3 Alumina (Al_2O_3)

Alumina is a well studied oxide which is used as an ingredient in aluminum production (from its hydrated form, bauxite), as an abrasive, a refractory material for high temperature metallurgical processes, a structural ceramic for aggressive environments, and as an electrical insulator [28,29]. Alumina is formed from the Bayer process applied to natural bauxite.[14]

Given its high melting point (2072 C), alumina is a useful refractory material, and its chemical stability, high hardness, strength, and low dielectric constant open up the variety of other applications mentioned above.[14] The structure of α-alumina, the most

common of the three structures (α,β,γ), is shown in Figure 1-4.

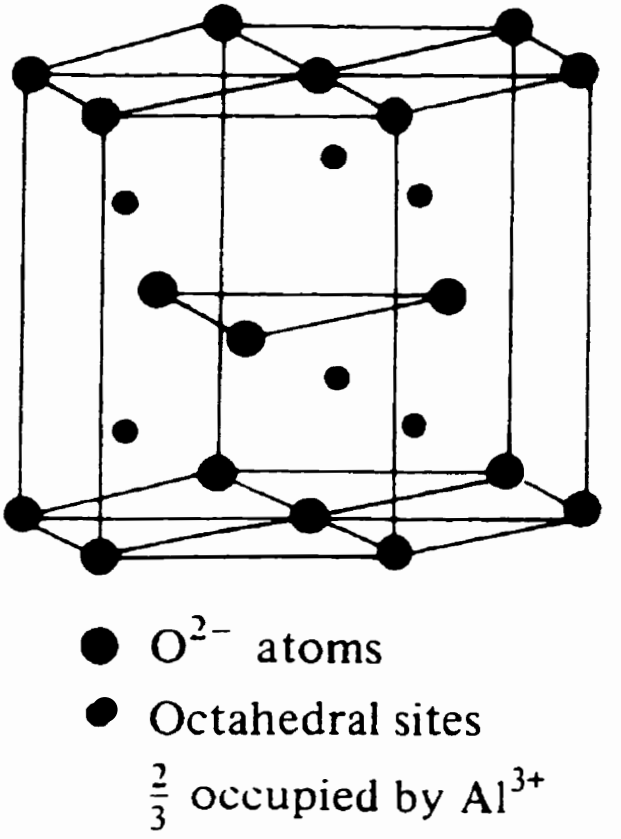

Figure 1-4. Hexagonal close-packed structure of α-Al_2O_3.[29]

1.2.4 Alumina - Silica System (Al_2O_3 - SiO_2)

There has been extensive interest in the alumina-silica system, especially over the past fifty years. This is primarily due to the refractory nature of high-alumina compositions which have high solidus temperatures [31] (Figure 1-5). The phase diagram also shows the stable compound known as mullite ($3Al_2O_3 \cdot 2SiO_2$) [14,24], which has prompted

heated debate, as to whether it is a congruent or incongruently melting compound. Nevertheless, much research has concentrated on this phase, due not only to its chemical and thermal stability, but also due to its dielectric properties which surpass that of alumina.[32]

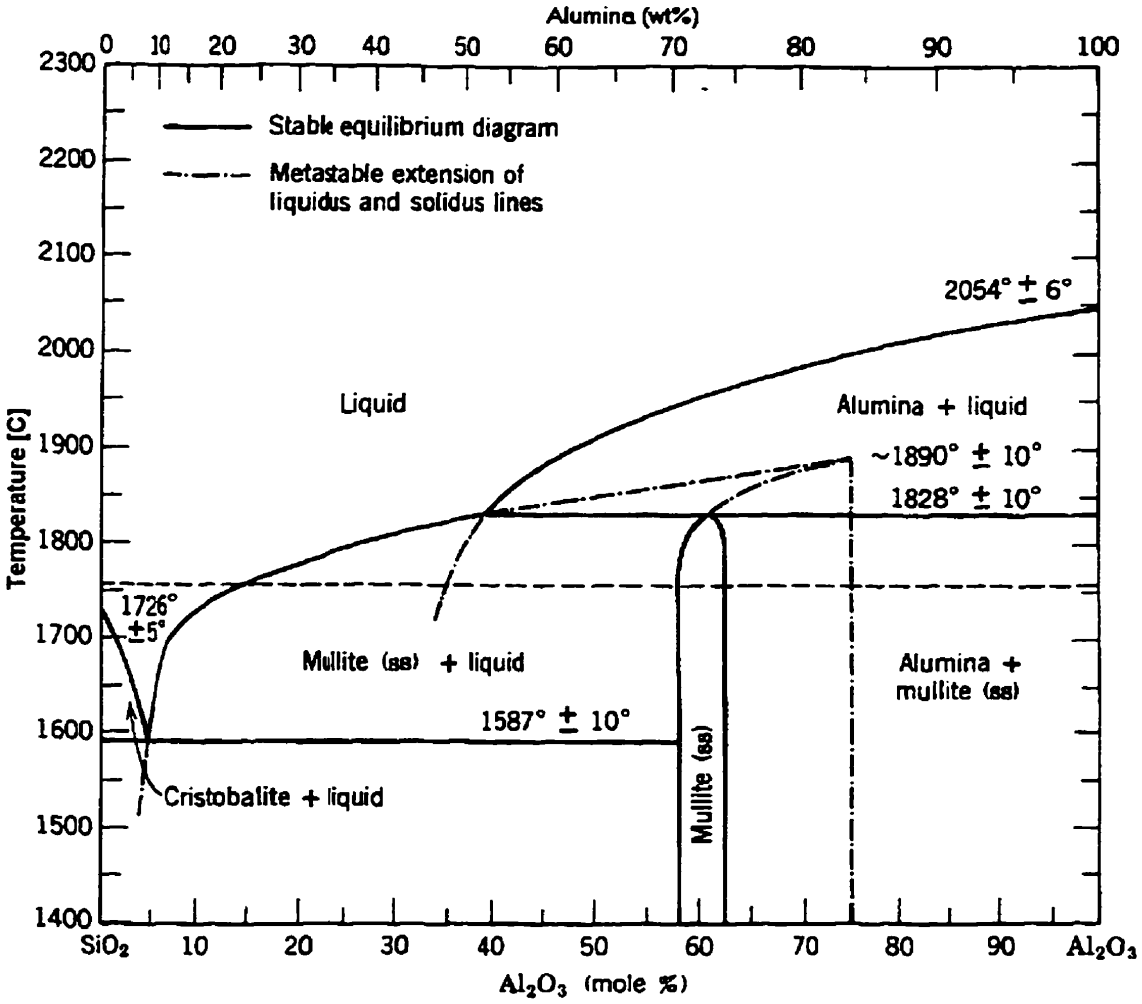

Figure 1-5. Al_2O_3 - SiO_2 binary phase diagram.[24]

Other alumino-silicates include kyanite, sillimanite, and andalusite; all have the same stoichiometric composition of $Al_2O_3 \cdot SiO_2$, but offer differing temperature ranges of

thermodynamic stability. When these minerals are heated to a liquid state they will typically recrystallise into mullite + silica.[28]

1.2.5 Lime - Silica System ($CaO - SiO_2$)

Calcium silicates have many areas of application but are most often of interest in slag chemistry, special glassy materials, and cement components. Many binary compounds exist in this system as can be seen from the phase diagram in Figure 1-6.

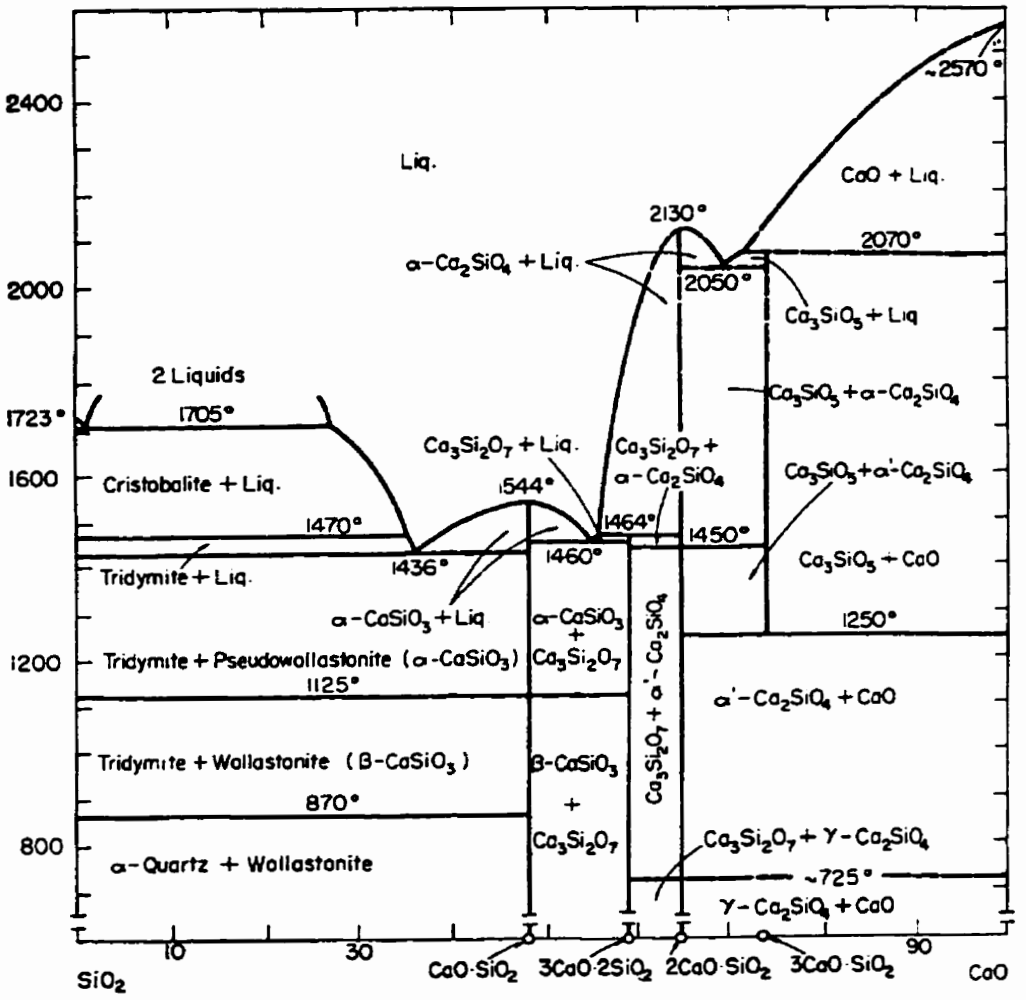

Figure 1-6. CaO - SiO_2 binary phase diagram.[33]

1.2.6 Lime - Alumina System (CaO - Al_2O_3)

Four stable binary compounds form in the CaO - Al_2O_3 system: $3CaO{\cdot}Al_2O_3$, $CaO{\cdot}Al_2O_3$, $CaO{\cdot}2Al_2O_3$ and $CaO{\cdot}6Al_2O_3$ (known mineralogically as hibonite), all of which melt incongruently. A further compound is referred to in older literature as $5CaO{\cdot}3Al_2O_3$, but this has been corrected by some authors to $12CaO{\cdot}7Al_2O_3$.[34] Figure 1-7 shows the

phase diagram for this system, which is most important in the field of rapid setting cements.

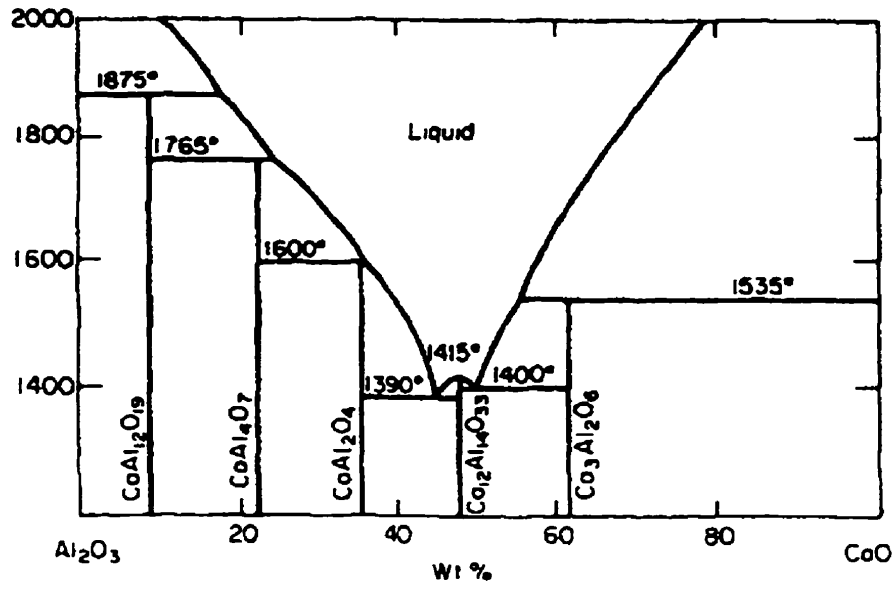

Figure 1-7. Al_2O_3 - CaO binary phase diagram.[35]

1.2.7 Lime - Alumina - Silica System (CAS)

The ternary phase diagram compiles all the complexities of the binary diagrams into one that is further complicated by the appearance of two ternary phases: anorthite ($CaO{\cdot}Al_2O_3{\cdot}2SiO_2$) and gehlenite ($2CaO{\cdot}Al_2O_3{\cdot}SiO_2$). The phase diagram is shown in Figure 1-8. Note also that the diagram contains numerous invariant points, Alkemade lines, binary joins, and eutectics, which make construction and interpretation very difficult. Shown in Figure 1-9 is a topological representation of the CAS ternary system with temperature being the vertical dimension of the model.[29]

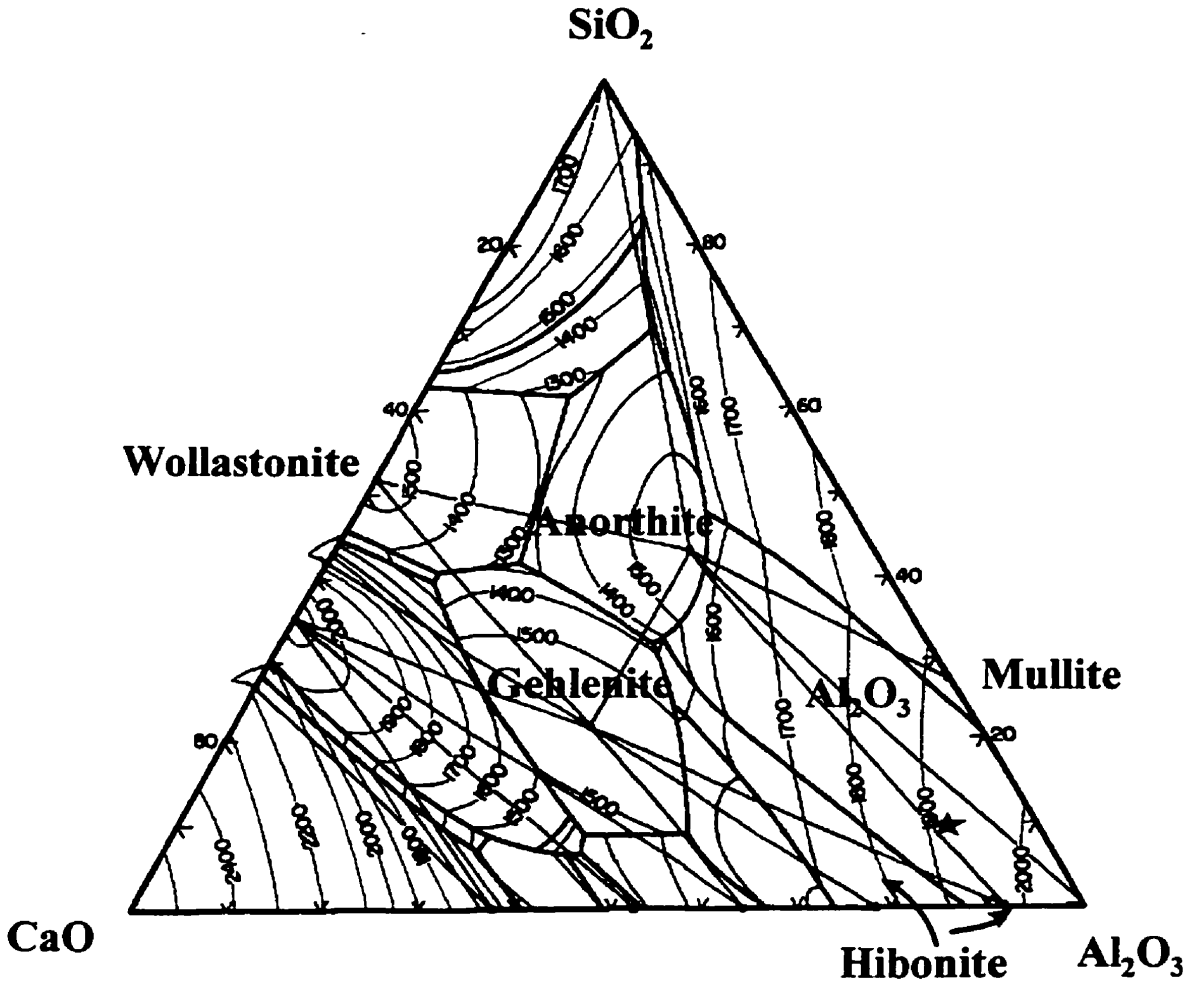

Figure 1-8. CaO - Al_2O_3 - SiO_2 ternary phase diagram with relevant phases labelled (modified figure of ref.[36]). The ★ shows the chosen system composition (corresponding to 80 wt% alumina + 20 wt% wollastonite).

Figure 1-9. Topographical representation of the CAS ternary system.[29]

In this thesis the following abbreviations will be used for simplification of the discussion: "C" = CaO; "A" = Al_2O_3; and "S" = SiO_2, and subscripts will signify the stoichiometry. For example, anorthite, $CaO{\cdot}Al_2O_3{\cdot}2SiO_2$, will be denoted as CAS_2. The complexity of

the CAS diagram with respect to the number of different phases which may be present means that it is possible to manufacture a large number of materials with widely differing properties.

(a) CAS Cements and Slag

The CAS system is very important in cement and concrete production and, as such, makes an inexpensive form of strong, stiff, and resilient materials which may easily be mixed, poured, formed into a desired shape, and allowed to set to achieve ultimate potential strength.[29]

Most building structures, city infrastructure, walkways, and foundations rely heavily on cement, and the most common is Portland cement. Figure 1-10 shows the region on the CAS phase diagram where Portland cements are found (note that 2-4 at.% FeO is also present). Also shown is the region of high-alumina cements, which are renowned for their ability to set quickly and achieve maximum strength after only 24 hours.[34] Other cements are possible between these two regions but these compositions set very rapidly and are thus impractical for common usage.

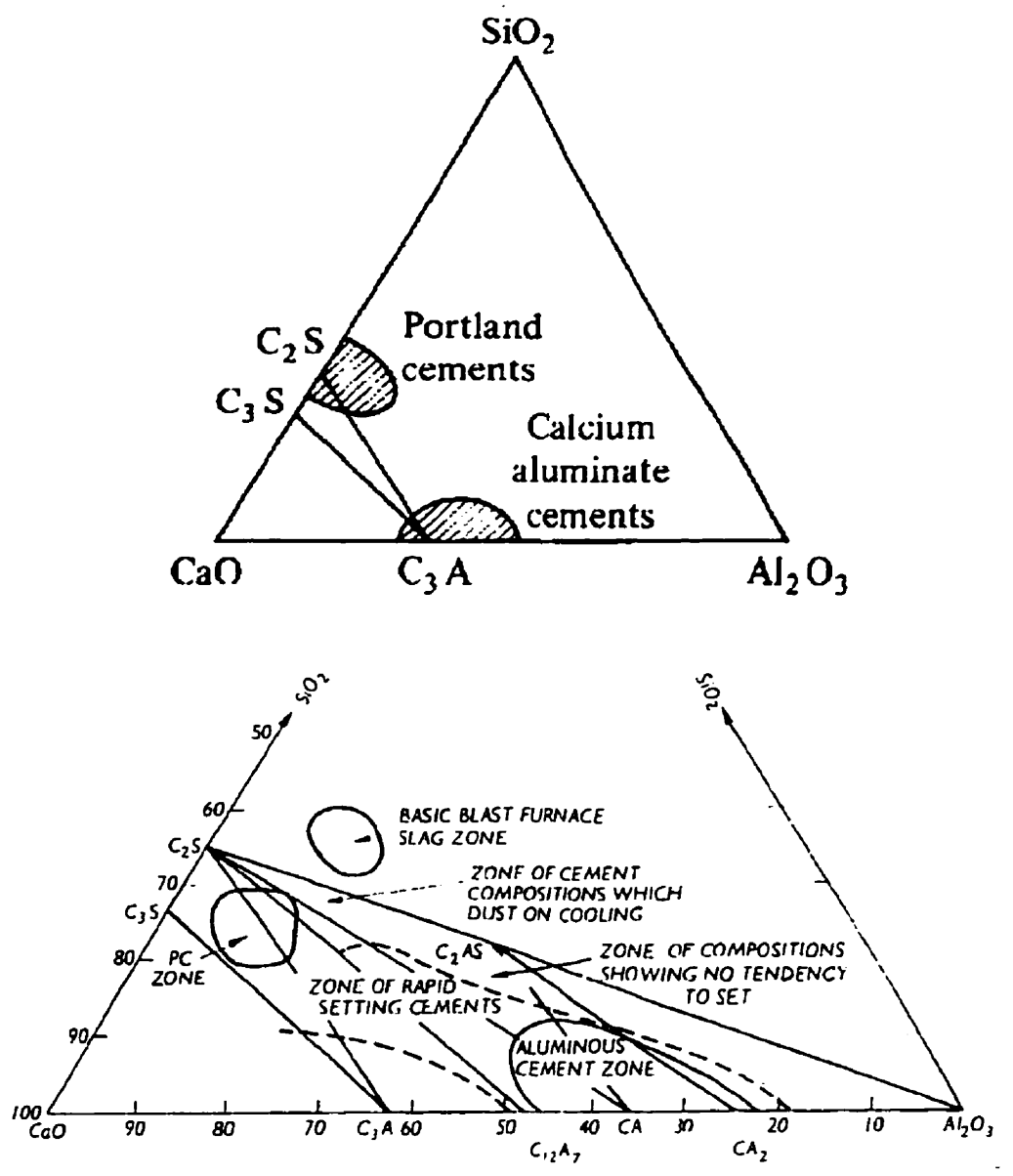

Figure 1-10. CAS ternary diagrams showing cement compositions.[29]

The cement bond formation involves a reaction of some of the constituents with water. The normal stages of setting are hydration, solution saturation, recrystallisation, and precipitation of colloidal silica.[29] The hydration stage gives off heat which may be

reduced by the presence of iron ($4CaO \cdot Al_2O_3 \cdot FeO$). Gypsum ($CaSO_4 \cdot 2H_2O$) is another common additive which will slow down the reaction to allow for forming processes.[34] High alumina cement is used without a retardant and sets due to formation of hydrated alumina from the C_3A phase. Not only is this cement advantageous from a fast set standpoint, but also is more resistant to sea water and exhibits less fluxing in refractory mortars.[29]

One source of the components used in Portland cement is blast furnace slag from integrated steel mills.[34] The CAS slag composition (Figure 1-10) corresponds to a low melting point region (<1400 C), so is quite fluid at steelmaking temperatures.

(b) Important CAS Glasses

Figure 1-11 is a sketch of the various areas of interest in glass and glass-ceramic research over the past 50 years. The dotted line was defined as an area of stable glass formation from a melt of 1600 C, and simply corresponds to the liquidus line at that temperature.[37] Referring to Figure 1-11, area 1 is the high silica compositions used for glass products, particularly mercury lamp housings, and became important during WW II, when a shortage of boron made borosilicate glasses too expensive. However, their high melting point limits current application of such CAS glasses, though they tend to limit ion migration and are used for glass-metal seals since their thermal expansion can match that of metals.[38]

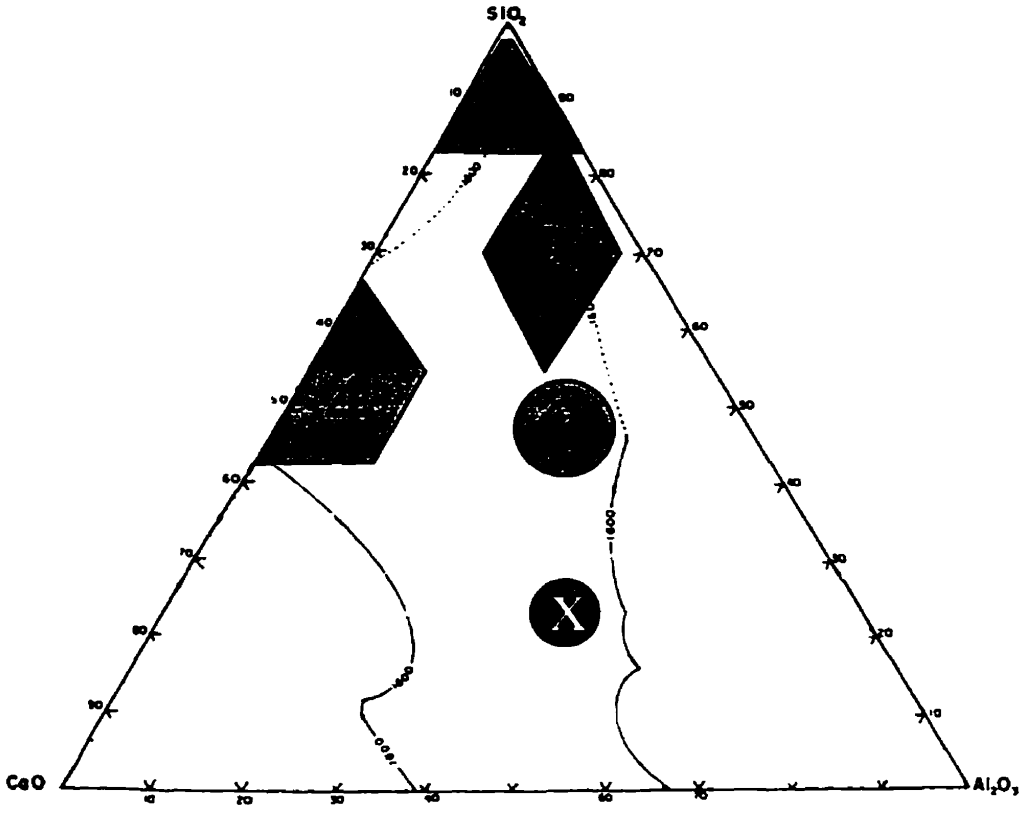

Figure 1-11. CAS ternary showing important glass compositions (see text). The region denoted with the "X" is the anticipated CAS liquid/glass composition after LPS of the alumina - wollastonite green body.

Area 2 represents the range of compositions investigated by Stookey [39], who claimed the first glass-ceramic patent in 1960. It is believed that Corning [38] uses these compositions for some highly specialised applications (ignition tubes, glass resistors, electron tubes, and infrared transmitting glass domes for heat-seeking missiles). Glass-ceramics are materials which tend to solidify as glasses but are processed in such a way as to generate a controlled amount of crystalline grains to achieve higher strength, stiffness, and thermal stability.[38] The crystallisation may be done by simple manipulation of

cooling rates or by nucleation on another phase, such as TiO_2.[40,41]

Area 3 is an anorthite rich area which has been extensively researched in Russia over the past few decades. These compositions can be fully crystalline or be of a primarily glassy character, depending on the processing, but in general have attractive dielectric properties, coupled with low thermal expansion coefficients.[42,43]

Finally, area 4 represents wollastonite-based materials, which commonly form a glassy phase, in spite of the fact that calcium silicate itself is considered a poor glass former.[24] Materials of these compositions have been developed for porcelains, glazes and other vitrified materials for firing at lower temperatures.[13,14] Often, a large degree of wollastonite and anorthite is present in the resulting microstructure.[44,45] These materials tend to have low water adsorption, and exhibit low firing shrinkage.[14] Other wollastonite rich materials are being investigated for medical implants such as bone replacements, since they are non-toxic and bond well with natural bone.[46] The main criterion for this application is reported to be a minimum strength of 200 MPa.

1.3 Advanced Ceramics

Advanced ceramics include many novel materials produced in the past 20-30 years, involving specific combinations of ceramic components, and new production and processing methods. The driving force behind advanced ceramic development centers on the need for mechanical strength at high temperatures or in environments susceptible to chemical attack. Other applications require the low thermal expansion offered by most

ceramics relative to metals, or specific dielectric requirements for electric/electronic devices.[7,47-50]

The primary limitation of ceramic use is inherently low toughness, so the greatest amount of research has been directed towards development of toughening mechanisms.[2,3] Very little literature had dealt with mechanical toughening of CAS ceramics (excluding toughening of concrete, and mullite) until the past few years when Corning made available a high toughness material made of silica-rich CAS glass-ceramic [51] reinforced with SiC fibres.[51-56]

USSR/Russian research over the past few decades had concentrated on wollastonite and anorthite-based porcelains and ceramics for use as electric insulators.[57] Current work on mullite-based glass-ceramic substrates for electronic packaging is also promising. The requirements of such an application is to have a low dielectric constant, high dielectric strength, adequate mechanical properties (for process handling), and a thermal expansion coefficient similar to silicon (3.0×10^{-6} K^{-1}). Mullite-based substrates seem to exceed the more commonly used alumina in most of these areas.[32,58]

1.4 Green Body Production

Production of a suitable ceramic green body depends upon the optimisation of a number of individual techniques, each of which contributes to the final mechanical properties which can be achieved.

1.4.1 Wet Processing

Wet processing involves both ceramic particle interactions and methods of evaluating the extent of particle dispersion such as the use of rheometric procedures.

(a) Particle Dispersions

Solid-in-liquid dispersions are found in many fields including foods, paint, inks and dyes, pharmaceuticals, cosmetics, detergents and ceramics. Proper control of the suspension is critical in each field in order to ensure best results and quality of the product. This is particularly true for ceramics which are susceptible to failure when improper processing leads to an inhomogeneous structure. Defects as small as 10 micrometers can lead to uncontrolled crack development and failure.

As late as the 1950's very little was known about ceramic particle interactions in suspension, and techniques for processing were somewhat of a black-art which required an experienced processor who had a "sense" of the ceramic suspension to interpret what modifications were required to optimise the slurry.

Around that time some background work in other areas of aqueous suspension research gave rise to new work defining particle interactions within a suspension. Today, this field has matured to a point where a broad understanding of suspension behavior exists and new processing agents and techniques are being found and optimised regularly.

(b) Rheology

Optimisation of a ceramic powder dispersion is accomplished by adjusting process variables, such as pH or dispersant concentration, and measuring the flow properties of the equilibrated suspension. Solution conditions such as these have a dramatic effect on the interaction between particles, particularly when solids concentrations are high. When particles remain separated, such as by electrostatic repulsion, steric hinderance, or by combinations of the two, then the apparent viscosity is low. When repulsive action is overcome by stronger attractive forces, especially van der Waals forces, then particles tend to form flocs or agglomerates which raise the consistency and make the suspension appear thicker.[59-62] When suspensions are cast into green bodies, a well-dispersed slurry forms a dense, homogenous particulate structure, whereas a flocculated suspension has large voids in the microstructure of the green body which lead to flaws in the final sintered product. Thus by measuring the flow properties, one can establish the best treatment conditions to produce optimum particle repulsion.

One simple way of doing this is by creating a low concentration suspension (e.g., 0.05 vol. fraction solids) under various treatment conditions and allowing the suspension to sit in a vial for an extended period (e.g., 20 h). By definition, well-dispersed suspensions tend not to settle since Brownian forces keep individual submicron particles aloft, and those that do settle due to gravity form a dense layer at the bottom of the vial.[63] Poorly-dispersed suspensions produce a sediment more quickly, since particles join together in large clusters and settle. As well, the clusters tend to have large void spaces which cause a very low density, spongy sediment. Thus, by measuring the proportion of sediment

height (h) to suspension height (H) over a defined time period, one can crudely classify particle interaction (i.e, low h/H = well dispersed; high h/H = poorly dispersed).

Another more reliable and widely-used technique is to measure applied stress over a range of shear rates for given suspension conditions. This gives an indication of particle interaction since suspensions under shear produce particle interactions.[60,64,65] Suspensions with high particle repulsion will tend to flow very easily, offering low shear stress over all shear rates. Conversely, particles with low or no repulsion may form a structure ar rest or at low shear rates. At higher shear rates, this structure will break apart causing a decrease in required stress as indicated by a decrease in viscosity. This behaviour, known as pseudoplastic or shear thinning, is common for most concentrated powder suspensions, and particularly for those with low repulsive interparticle forces.[62]

1.4.2 Slip Casting

The most flexible wet forming method for ceramic production is slip casting. This method involves pouring the suspension onto a plaster of Paris mould so that the suspending medium (water) is absorbed leaving behind a consolidated layer of ceramic particles on the surface of the plaster. Consolidation rates follow a square root function and cast thickness is limited to a couple of centimetres for submicron alumina suspensions.[66-70] Another limitation is the pore size distribution; pores are generally fine near the plaster but grow as the distance from the surface increases. This can lead to warpage during sintering since a porous green microstructure will shrink more than a dense one. This can be minimised by intentionally causing light flocculation in the slurry

(which ensures uniform pore distribution throughout the compact) or by introducing light agitation to the system during casting.

1.5 Densification

Densification techniques have historically been limited to cementitious bonding (e.g., concrete) and kiln firing (sintering). Today these have been expanded to include sol-gel processing, cold isostatic pressing (CIP) + sintering, reaction sintering, liquid phase sintering (LPS), hot pressing (HP), hot isostatic pressing (HIP), chemical vapour deposition (CVD), physical vapour deposition (PVD), flame spraying and plasma spraying.[4,24] The latter four methods are limited to production of ceramic coatings and shall not be elaborated on.

Sol-gel processing is popular in that the reactions can be tailored to produce desired phases and ratios of products of various grain sizes.[4] This technique is prohibitive, however, in that the reaction product is highly porous and must undergo repetitive processing to increase density to reasonable levels. The pressing techniques are limited to small simple shapes; thus, the final cost is somewhat prohibitive and production volumes are low.

1.5.1 Sintering

Sintering techniques are the most flexible and most inexpensive densification method for ceramic production. The mechanisms of densification depend on the materials undergoing

the treatment but is dependant on five main variables: heating rate, sintering temperature, sintering time, atmosphere, and cooling rate.

For most systems involving solid state sintering of fully dried powder green bodies, heating and cooling rate and atmosphere present are not reported, but are assumed to be reasonably slow (e.g., 5-25 K/min, performed in air). Alteration of heating rate may be necessary if certain phase changes are anticipated which may need to proceed isothermally before further sintering can be accomplished. If the product contains a liquid phase at the sintering temperature, is susceptible to thermal shock, or requires further heat treatment, then cooling rates may be critical to develop a reliable, stress-free or crack-free product.

In some cases, the atmosphere can be altered to aid in pore removal (some gases transport through ceramic grains much faster than others), either by changing relative gas pressures during sintering or by applying a vacuum. A high partial pressure of oxygen may also limit development of a glassy phase during anticipated liquid phase sintering.[71]

In the case of the alumina - wollastonite system, chemical reactions are inevitable at sintering temperatures, and liquid regions develop easily above 1400 C according to the phase diagram.[36] In some cases the presence of a liquid phase is undesirable since it virtually guarantees the development of a glass phase in the final product. However, for systems which may be difficult to densify, the presence of a liquid phase dramatically increases densification rates since diffusion and mass transport are orders of magnitude faster when compared to solid-state sintering. Further, devitrification of the resultant glass

can leave a fully dense, crystalline ceramic.

Reaction sintering simply implies that chemical components within a green body react at sintering temperatures to produce new species; in some cases, the reaction involves development of a liquid phase at the process temperature; this is known as reactive liquid-phase sintering (RLPS). In this work, since wollastonite is certain to react with alumina, producing a CAS liquid above 1400 C (sintering temperatures for all studied compositions), the densification technique is anticipated to be RLPS.

1.5.2 Reactive Liquid Phase Sintering

Should a liquid phase form, three options exist: (1) accept that a glassy phase will form in the product and accept the inferior mechanical properties, (2) slowly cool the samples from the sintering temperature to promote crystallisation of the glass, and/or (3) further process the product by crystallising the glass with a secondary heat treatment (devitrification).

If the purpose is to improve mechanical strength or toughness, then option (1) is inadequate. However, glass-ceramics may have other attractive properties which make option (1) viable. For instance, lithium aluminosilicate (LAS) glass-ceramics have excellent thermal shock resistance, and other alumina-based glass-ceramics have attractive dielectric and thermal properties which make them useful for substrates for electronic components.[26,48,72,73]

The second option, slow cooling, may be unpredictable since crystal nucleation may vary from sample to sample; thus replication of microstructure may be difficult from one day to the next. Further, full crystallisation may be incomplete or unreasonably slow.

For best mechanical strength and toughness, a devitrification treatment is sometimes necessary. For most liquid phase sintering regimes this first involves quenching the product to produce a homogenous glass, followed by a nucleation heat treatment which develops high numbers of nuclei in the bulk of the glass phase. Finally, the temperature is quickly ramped to a higher level at which crystal growth is known to occur. This technique is known to remove most or all of the glassy phase from systems in which crystallisation is possible.[24,25]

Finding the temperatures at which bulk nucleation and crystallisation occur may be facilitated by using differential thermal analysis (DTA) techniques.[74-80] This normally involves examining crystallisation peaks which may appear on a DTA scan, and then applying various systematic nucleation treatments to observe changes in crystallisation peak magnitude, breadth, and shift. If a peak shifts to lower temperatures, and grows larger and sharper, the bulk nucleation treatment has been successful. In this way, both the nucleation and the corresponding crystallisation temperatures can be found. Further analyses involving isothermal studies may be done to find the most effective devitrification technique.

1.6 Characterisation

Once a ceramic has been densified and fully processed, it is necessary to evaluate the physical and mechanical properties it may possess. In the field of structural ceramic research this most often involves density, microstructure, composition, toughness, strength, and modulus of elasticity measurements. Abrasion resistance is dependant on many of the preceding characteristics, and may serve to open up applications of a newly developed material in wear intensive environments. Often, thermal shock resistance is also a desired attribute; thus, it may also be desirable to find the thermal expansion coefficient of a material. Finally, if there is an interest in possible electronic applications it may also be worthwhile to measure the dielectric constant, dielectric strength, and resistivity. For the purposes of this investigation, however, only the structural aspects of a material are of interest.

1.6.1 Density

Density may be measured using the Archimedes principle using mercury to find the bulk volume (change in mass when sample is fully immersed yields amount of mercury displaced) and when divided by the sample mass, the bulk density is found. Knowing the proportions of the constituents present in the sample, the theoretical density (TD) may be calculated and compared to the bulk density to find the percent theoretical density (%TD) of the ceramic product.

1.6.2 Microstructure

One of the best instruments to characterise the microstructure of any ceramic material is a scanning electron microscope (SEM). This is due primarily to its excellent resolution at very high magnifications (more than 50,000X), whereas an optical microscope has a practical limit of about 2000X. As well, an SEM has much greater depth-of-field in comparison to optical microscopes, vital in examining surface morphology, porosity, and fracture surfaces.

X-ray microprobe analysis of the ceramic can be performed with a suitably equipped SEM. This technique, when calibrated using reference standards, can give a quantitative analysis of the oxide compounds excited by the electron beam.

To perform true qualitative analysis, the ceramic can be tested using an X-ray diffraction unit which can establish which compounds are present and, to a limited extent, the relative amounts of each.

1.6.3 Mechanical Evaluation Techniques

Once the physical aspects of a ceramic are known, the next step is to determine the mechanical properties. When a large enough sample is prepared, it may be machined into appropriate sizes to evaluate the mechanical strength of the material. Specimens can be cut using a diamond saw and refined using grinding and polishing techniques.

Three main strength characteristics of a ceramic are: compressive strength (σ_c), tensile

strength (σ_t), and modulus of rupture (MOR).[81] Most ceramics have high compressive strengths compared to most materials and thus this parameter is of limited practical value. However, tensile strength of ceramics is characteristically sensitive to the grain size and the presence of flaws, both internal and at the surface. Typically, tensile strength is almost an order of magnitude lower than compressive, and is therefore much more critical in most design situations. Unfortunately, it is difficult and expensive to obtain reliable tensile data since specimens need to be finished to a high tolerance using diamond machining and any slight surface imperfection, warpage or misalignment cause scatter in the results. As a result, ceramic strength is rarely measured or reported.

The modulus of rupture test is performed by applying a force to a bar set up in a four-point bend configuration. This technique has garnered much support recently, but results can be sensitive to sample misalignment and warpage.[82]

An even more important material parameter is the fracture toughness (or resistance to crack propagation) of the ceramic. This is because of the inherent brittleness of most traditional ceramics, and investigations in improving ceramic toughness are responsible for much of the research performed on ceramics in the past two decades. Along with the many types of reinforcement and crack deflection mechanisms which have been developed, there has also been research into evaluation of toughness itself.

Material toughness depends on the response of a material to crack initiation and propagation. The type of crack that develops depends on how the force in applied. There

are three standard modes of crack development (Figure 1-12) but the most widely reported and valued is the mode I failure and its corresponding critical fracture toughness, K_{Ic}.

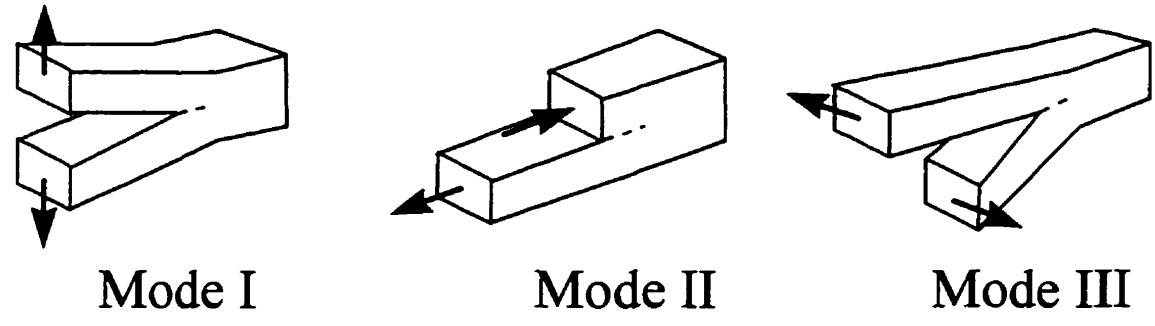

Figure 1-12. Displacement modes for material fracture.

The two most common techniques of toughness evaluation are by single-edge notched beam (SENB) using a four-point bend apparatus [83,84] and a simple Vickers indentation technique.[83,85-87] The latter test yields a critical fracture toughness characteristic called K_c since this method does not entail true mode I fracture. This parameter can be compared to K_{Ic} and many models have been developed to produce K_c values from indentation data which come close to this value.

The indentation toughness test is easily performed by using the same samples prepared for microscopy and performing standard Vickers hardness tests at various sites in the samples. The impressions made by the diamond indent generate cracks at the corners where stresses are more concentrated. The progression of the crack depends on the toughness of the material. Numerous studies have been done to develop models which

translate crack length (measured using an SEM), indent size and applied load into K_c values. Evaluations of many of these models [86,87] have shown that some are more applicable to alumina-based materials; specifically, the Evans and Charles [88] and the Lankford [89] models. Another reference [83] cited two other preferred models (the Miyoshi [90] and the Marshall and Evans [91] models), and a final model was suggested by Anstis *et al.*[85] All have been shown to give close estimates of the mode I fracture toughness parameter, K_{Ic}.

Other mechanical properties such as Young's modulus, E, and Poisson's ratio, ν, can be measured using an ultrasonic system which measures the propagation and reflection of sound waves through a small sample. The response of the material depends on the stiffness and the strain in different directions. Measurement of these parameters is important in characterising other properties of the material, such as indentation toughness, thermal shock parameter, and even the modulus of rupture.

Some of the above-mentioned properties can be also used to establish parameters related to the abrasive wear resistance of the ceramic. This property could be useful since similar ceramics are frequently used in high-wear applications.[4]

As a final evaluation, the thermal expansion coefficient may be measured using a dilatometer which measures the change in length of a sample when heated, relative to a known standard, such as alumina. Knowledge of the coefficient of thermal expansion (CTE), or, in this case, coefficient of linear thermal expansion (α) is vital in that high

temperatures can induce large thermal stresses within a material with a high CTE. If such a sample undergoes high heating and cooling rates, failure is almost inevitable. When this characteristic is known, an estimate of the resistance of the material to a thermal shock can be made.[4]

2. THEORY

2.1 Particle Surfaces in Aqueous Suspension

When ceramic particles are introduced into water the natural surface charges interact with any ions which may be in solution. Two reactions are possible; the first involves interaction between metal ions at the surface and aqueous hydroxide ions,

$$M^{-} + [OH]^{-} \leftrightarrow MOH \qquad (2\text{-}1)$$

whereas the second involves metal oxide ions at the particle surface and hydrogen ions in solution,

$$MO^{-} + [H]^{+} \leftrightarrow MOH \qquad (2\text{-}2)$$

Depending on the atoms present on the particle surface, the ions in the solution will equilibrate to satisfy the above reactions. Surfaces with more negative charges will attract more $[H]^{+}$ ions and shift the system to a higher pH. If more acid is added, the system is forced to a lower pH and the surface must accept more $[H]^{+}$ ions to maintain equilibrium. This sets up a charge imbalance at the surface and causes counterions (in this case, $[OH]^{-}$) to become attracted. Further, the abnormally high concentration of counterions draws in more $[H]^{+}$ setting up what is known as a double layer [92,93] as shown in Figure 2-1.

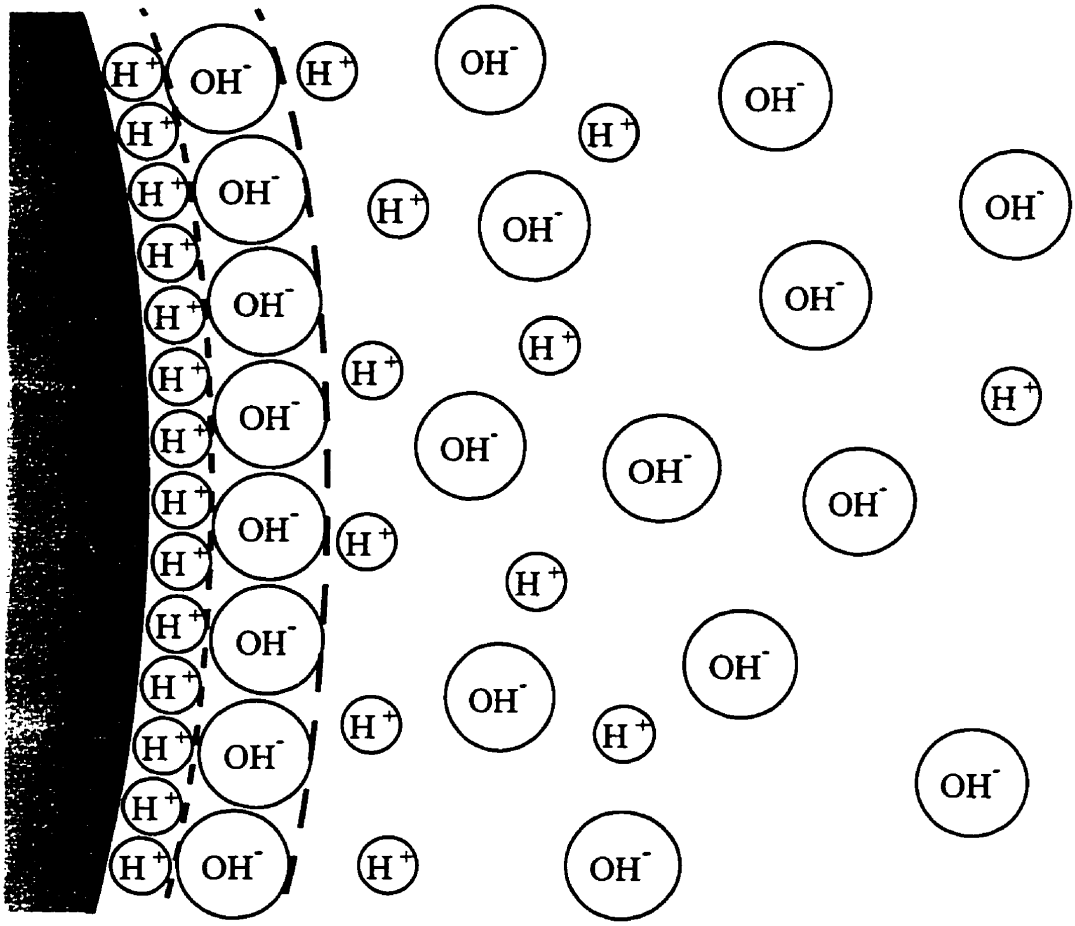

Figure 2-1. Two dimensional representation of interactions of ions in solution with charges on the particle surface.

Moving from the first ionic layer out into the solution, the relative electrical potential decreases until equilibrium is re-established. The distance away from the surface that this electrostatic effect reaches is dependent upon the surface charge and the ionic concentration of the solution. Modeling of ion distribution around a charged particle is commonly done using the Boltzmann distribution [94],

$$n_i = n_i^0 e^{-z_i e\psi / kT} \qquad (2\text{-}3)$$

where n_i and n_i^0 represent the number of ions per unit volume at a distance r and ∞ respectively, z_i is the valence of ion i, e is the elementary (proton) charge, ψ is the potential at distance r, k is the Boltzmann constant, and T is the absolute temperature. Thus, there is exponential decay of the ion concentration away from the surface.

The outside of the double layer represents the slip plane of the particle surface, and various charge measurement techniques (e.g., electrophoresis) actually measure the voltage at this distance and not the physical particle surface directly. This voltage is known as the ζ-potential (Figure 2-2). The double layer thickness can be compressed by increasing ionic (e.g., salt) concentration of the solution.

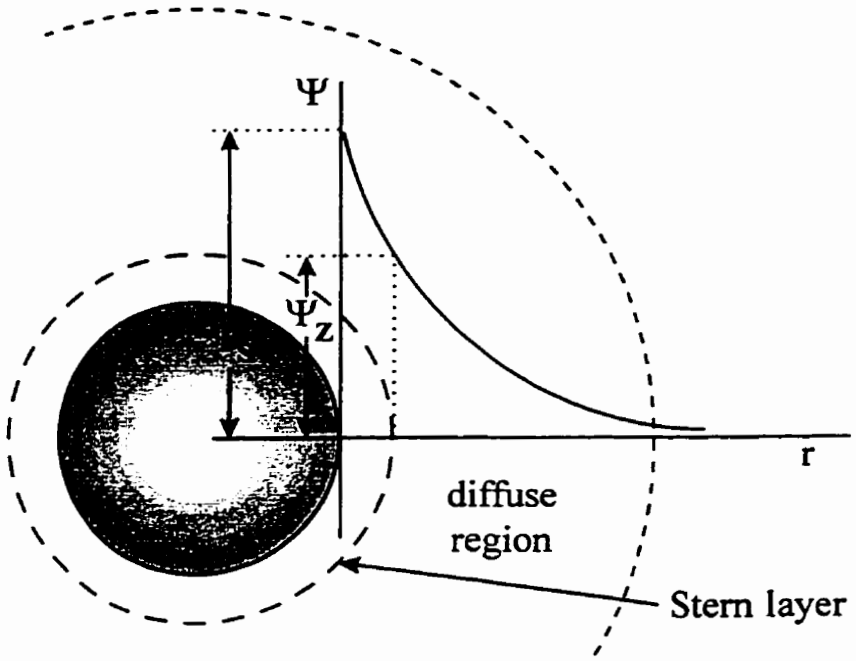

Figure 2-2. Schematic representation showing electrical potential as a function of distance from particle surface and the position of the ζ potential (shown as Ψ_z) at the slip plane.

The Derjaguin-Landau-Verwey-Overbeek (DLVO) theory [92,93] explains how particles interact in the presence of surface charges. Van der Waals forces tend to draw particles together, especially when the particles are submicron, while surface charges on like particles tend to supply a mutually repulsive force. These both diminish with increasing separation distance.

An example of a well dispersed electrostatic system is given in Figure 2-3. The plots at the top show the counteracting attractive and repulsive forces (the bold line represents the total interparticle force) and the bottom plot shows the resulting energy versus distance relation.

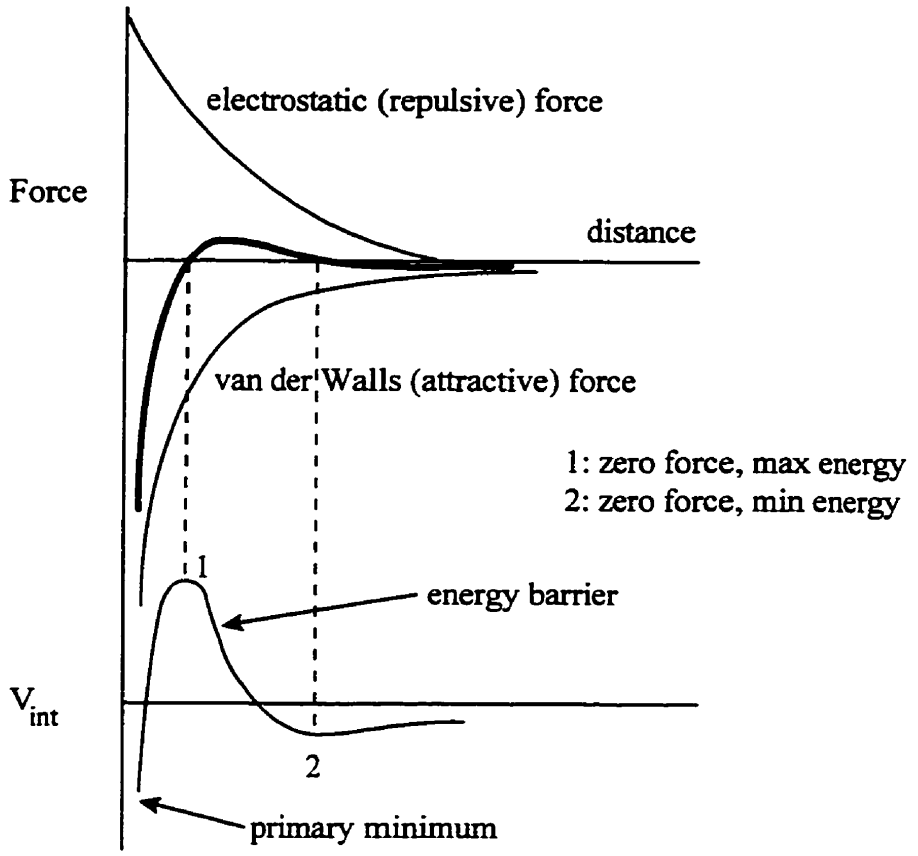

Figure 2-3. Interparticle force versus distance from particle surface in an electrostatically stabilised system according to the DLVO theory. The corresponding energy (V_{int}) versus distance relation is given immediately below.

As can be seen, when particles in a well dispersed suspension come together, they approach an energy barrier and assume the zero-force/(secondary) minimum energy distance (2). If particles are brought into intimate contact, beyond the energy barrier (1) and into the primary minimum, then the particles are irreversibly joined, forming an undesirable agglomerate.

In the absence of electrostatic forces, dispersion is still possible if a polymeric dispersant is used (Figure 2-4). In this case, called a steric dispersion, the long polymer chains become attached to the particle surface and form a mechanical barrier to particle contact. Thus, the primary minimum is moved far enough away so that the particles can remain free to move within the aqueous system.

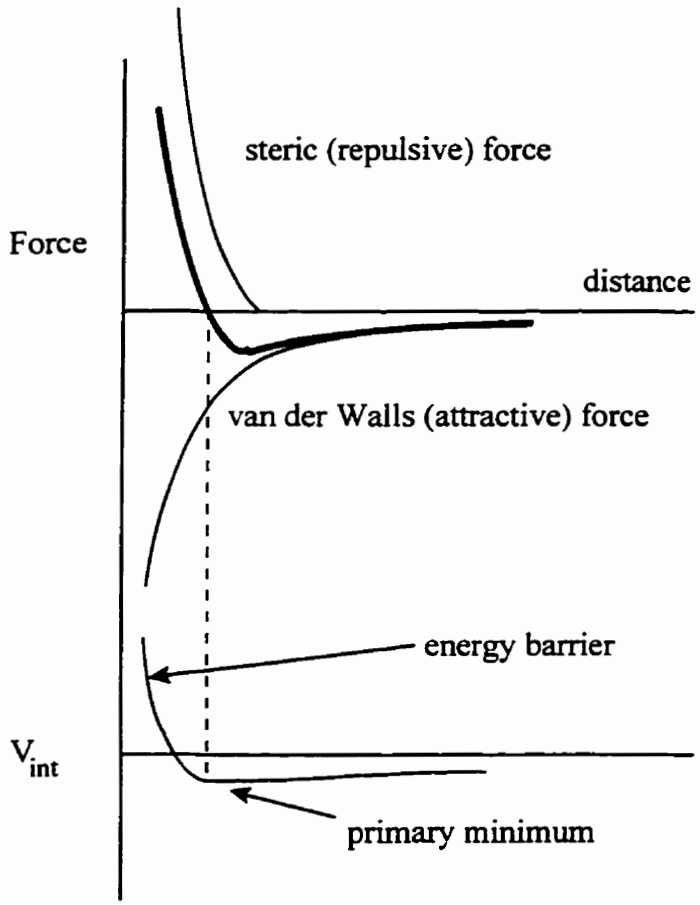

Figure 2-4. Interparticle force versus distance from particle surface relation for a sterically stabilised particle suspension. The corresponding energy plot is given below.

In electrosteric dispersions, both electrostatic and steric repulsive forces are available to maintain particle separation (Figure 2-5). The regime is necessary for difficult systems with particles prone to strong flocculation.

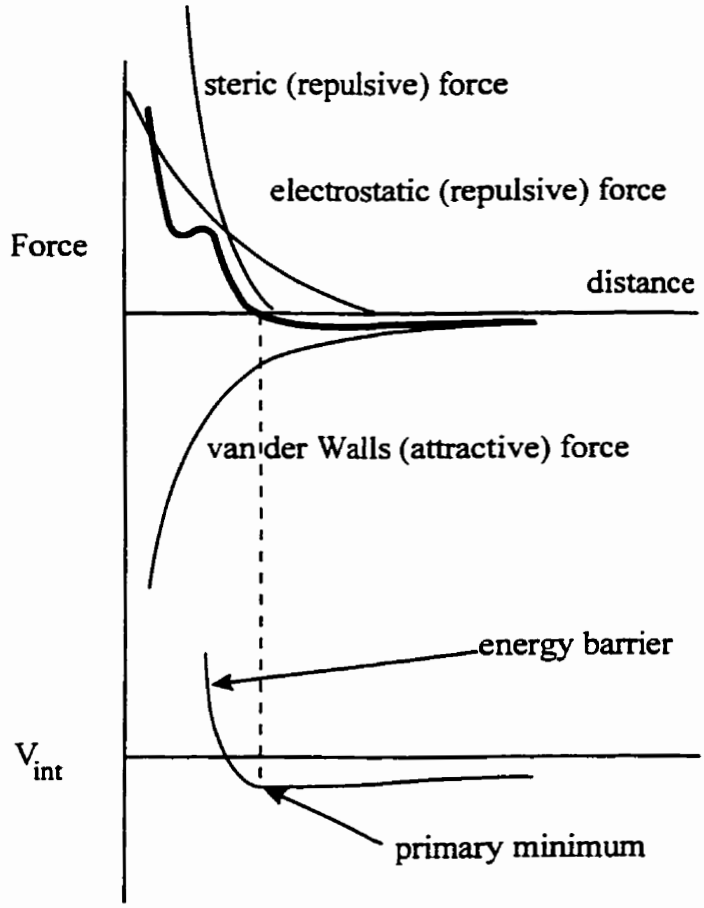

Figure 2-5. Interparticle force versus separation distance for an electrosterically stabilised system. The corresponding energy curve is shown below.

Polymeric dispersants are often ionic in nature (called polyelectrolytes) and may attach to charged sites on the particle surface. As well, some dispersants are charged on the unattached end of the chain so that they spread out (repelling other polymer chains

attached to the same particle and other particles within the system). This effect is dependent upon the ionic conditions of the system, and can result in an excellent dispersion.

2.2 Rheology

Rheology is the study of the deformation and flow of materials, and involves examining how materials respond to applied mechanical forces.[95] Rheological characterisation of ceramic suspensions helps to determine optimum processing methods to best achieve high density, and homogeneous cast bodies from stable suspensions. When studying the rheological properties of fluid suspensions, it is necessary to become familiar with the science of rheological measurement (rheometry).

2.2.1 Fluid Behaviour

The behaviour of fluids undergoing simple shear may be characterised in four ways: Newtonian, shear thinning, shear thickening, or plastic.[95-98] For Newtonian fluids, viscosity, η, is a material constant and not dependent on shear rate. Shear thinning fluids exhibit decreasing viscosity with increasing shear rate, whereas shear thickening (dilatant) fluids have the opposite behavior (Figure 2-6). Fluids which have plastic characteristics require a certain amount of stress (yield stress) in order to disrupt the solid-like structure and begin to flow in response to further stress or strain.

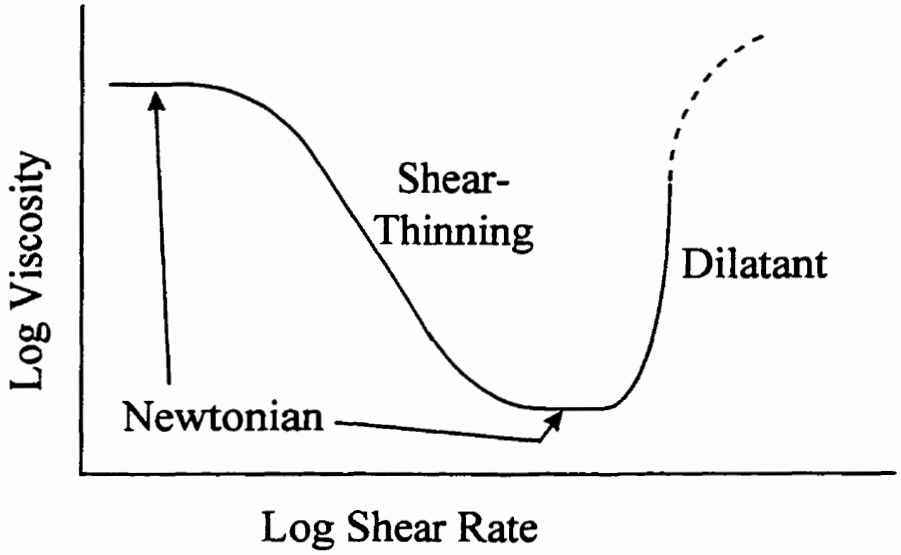

Figure 2-6. A typical steady shear rheogram for a particle suspension. Fluid behaviours are labelled according to the slope of the curve.

Newtonian flow is common but occurs only in suspensions with very low solids fraction. Also, Newtonian conditions may only occur at certain extreme ranges of shear rate.[97]

Shear thinning fluids may be plastic or pseudoplastic. Plastic shear thinning (Herschel-Buckley) and Bingham fluids require a finite or yield stress to initiate flow and then become shear thinning. Pseudoplastic fluids do not appear to possess a yield stress (Figure 2-7).

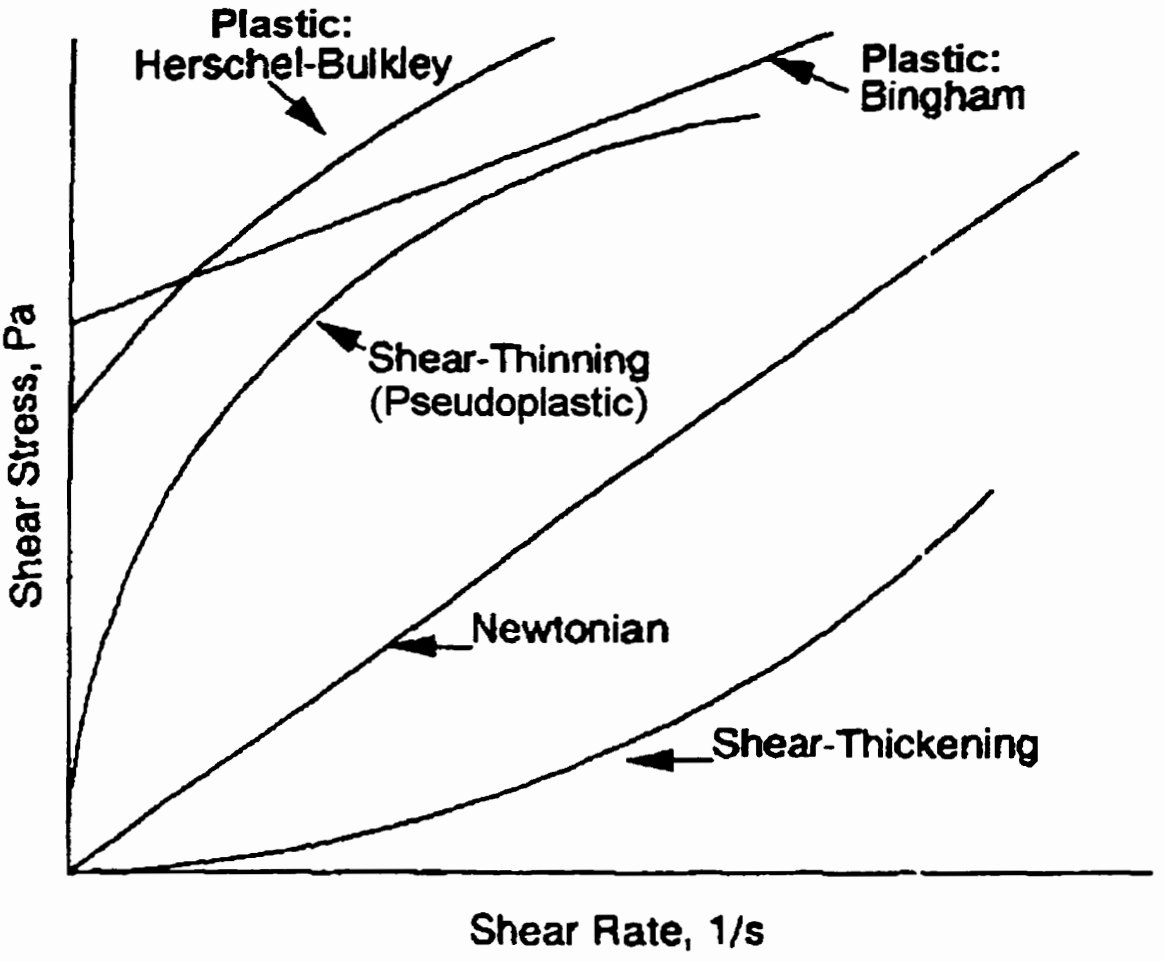

Figure 2-7. Types of fluid behaviour in response to increasing shear rate.[98]

Shear thickening materials are sometimes known as dilatant since the particles impact each other at high shear, and an influx of the fluid medium is required to fill the inter-particle voids.[97] This effectively increases the solids content of the suspension such that normal flow behavior is hindered and much higher stress is required to yield to increasing strain. This behavior is observed in highly loaded suspensions which have high inter-particle repulsive forces, and often the shift to dilatancy is sudden and dramatic,

transforming the fluid to a dense solid seemingly instantaneously, after a critical shear rate is reached.

Non-Newtonian fluids often have time dependent characteristics, in which its apparent viscosity may decrease over time at a constant shear rate. This behaviour is known as thixotropy. Finally, rarely, a fluid may be rheopectic, having an increased viscosity with time. Tests for these behaviors include measuring stress with step changes in shear rate.[96]

2.3 Slip Casting

Slip casting, also known as colloidal filtration, is a process by which an aqueous suspension of ceramic powders is consolidated into a dense "green" body. Normally this process involves pouring the suspension into a plaster mold, at which point the fluid media is absorbed into the mold, leaving behind a solid layer. The thickness of the ceramic deposited on the mold, x, is a function of casting time, t:

$$x \propto t^{1/2} \tag{2-4}$$

The casting rate slows due to the increased distance the fluid must travel to reach the plaster interface and the decreasing fluid concentration gradient (Figure 2-8). The practical thickness limit for standard slip casting of dense aqueous suspensions is generally less than one centimeter. Lightly flocculated systems have faster fluid transfer (due to the low density nature of the cast body) and can achieve greater thicknesses (several centimeters) with low overall density. As well, pore size distribution is more uniform in comparison with well-dispersed systems, which tend to have high density

close to the plaster interface and increasing pore size and frequency as a function of distance away from this interface. Such a condition may lead to warpage of the ceramic body upon sintering, due to differential shrinkage.

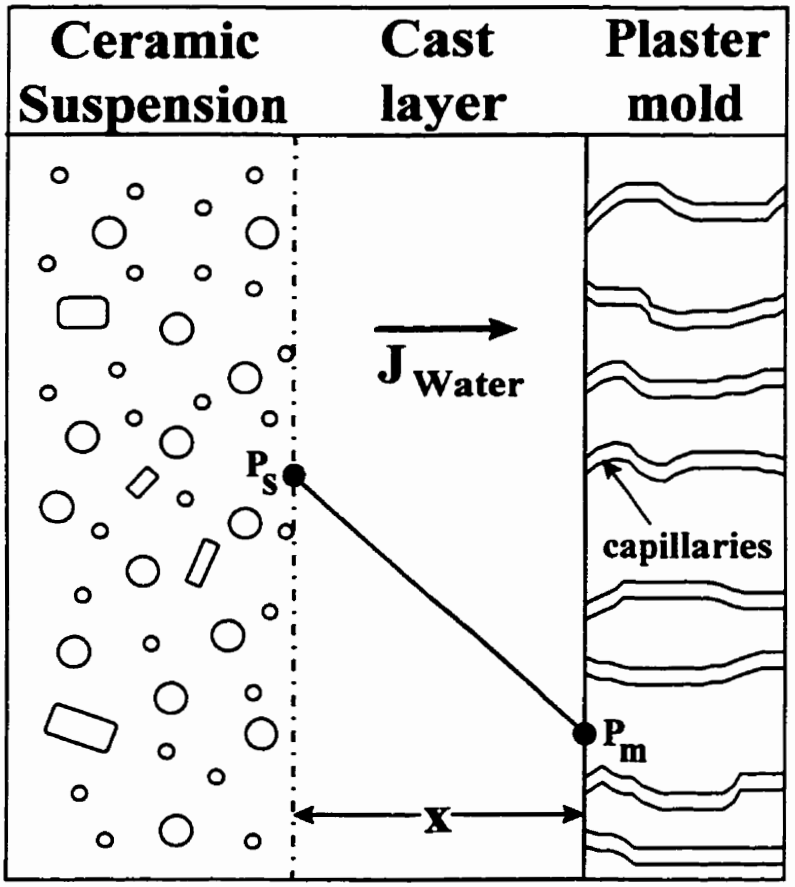

Figure 2-8. Schematic two dimensional representation of a slip casting procedure in progress. J_{water} is the flux of water transport from the suspension to the mold, x is the cast thickness, and P_s and P_m are the pressures within the suspension and mould, respectively.

For a liquid phase sintered body, microscopic pores are not a significant concern compared to macroscopic pores caused by entrapped air bubbles during casting. Large

pores tend to form voids which cannot be removed under standard heat treatment conditions and can act as strength-limiting flaws.

2.4 CAS Phase Equilibria

The lime-alumina-silica phase diagram is very involved and contains many binary and ternary compounds. For this study, the CAS ternary published by Gentile and Foster [36] will be taken as an adequate reference for the system. Modifications involving F*A*C*T thermodynamic software will also be considered.

Figure 2-9 shows the alumina-rich end of the CAS ternary as well as species which may be expected to form during high temperature reaction sintering of the alumina - wollastonite green body. The overall system composition is within the alumina stability field and is indicated by the star (★) symbol.

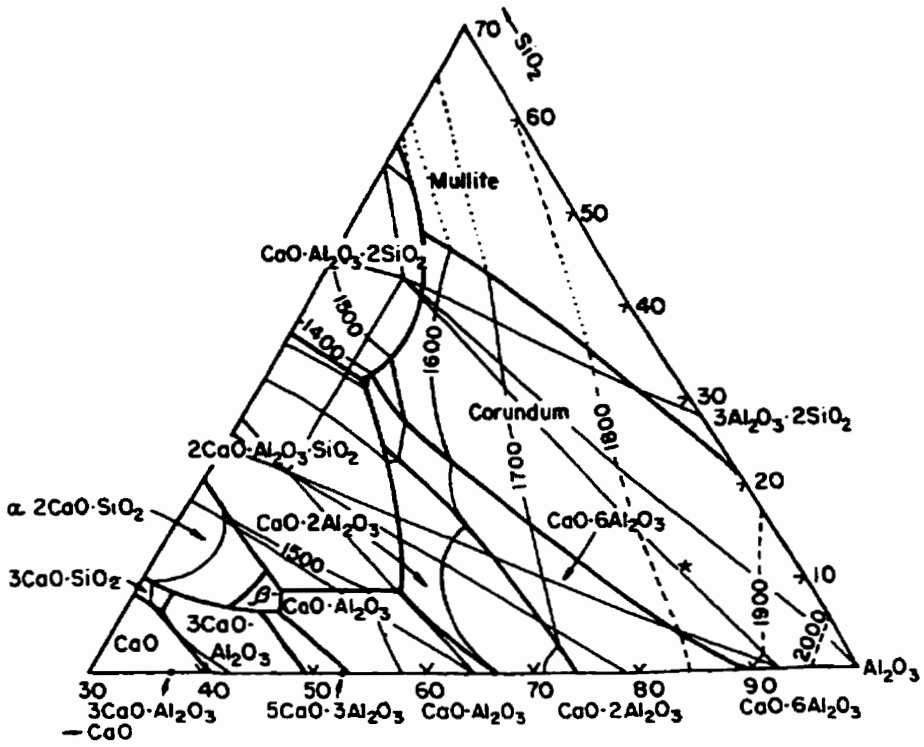

Figure 2-9. Alumina rich end of the CaO - Al_2O_3 - SiO_2 ternary phase diagram.[99]

As this composition is within the alumina-hibonite-anorthite phase triangle, these are the anticipated crystalline reaction products under equilibrium conditions. Using the lever rule it was determined that the final structure should contain 58 wt% hibonite, 24 wt% anorthite, and 18 wt% alumina. An isoplethal study of the system reveals that at temperatures above 1405 C, a liquid phase exists and the amount present relies upon the temperature of the material. Upon cooling, the hibonite is expected to begin to crystallise at 1425 C followed shortly thereafter by crystallisation of anorthite at 1405 C. Below this temperature the system should be 100% solid. The conversion of much of the alumina into hibonite seems unreasonable from a kinetic standpoint and thus extensive hibonite

formation was not expected. A more reasonable estimate of the final structure might contain 60-70 wt% alumina, 15-20 wt% hibonite and 5-15 wt% anorthite.

In many silicate systems, particularly the CAS system, glass formation instead of crystallisation is anticipated. The extent of glass formation is normally difficult to predict, but relies heavily upon the presence of nucleation sites and rate of cooling. Thus the thermodynamic predictions of the final crystal proportions may be inaccurate.

One method to control the amount of glass present in the final product is to use a quench + devitrification technique. Should the semi-solid ceramic be quenched from the liquid-phase sintering temperature, the resulting structure should contain only crystalline alumina grains and glass having a composition of approximately 40 wt% alumina - 31 wt% silica - 29 wt% calcia according to the phase diagram. Since amorphous phases tend to have poor mechanical properties, they are often crystallised using a post-sintering heat treatment.[24] This crystallisation, if carried to completion, should develop the products expected using the ternary diagram.

However, other factors may also affect the final products and microstructure. Should one component have high diffusivity in comparison with another, then one phase may be favored during crystallisation, resulting in a disproportionate amount created in the overall product. Further, kinetics of formation of some expected compounds may be so slow that they may not even be present in the devitrified ceramic.

As a result, caution must be used when relying upon microstructure predictions using published (equilibrium) thermodynamic data for guidance.

2.5 Densification

Once dry, a green body can undergo the final stage of production, high temperature densification, or sintering. This step is intended to remove porosity and form strong intergranular bonds. If no liquid phase forms at the process temperature, it is known as solid state sintering.[100] In this case, bulk and surface diffusion control the rate of densification. Sintering can be broken down into three distinct stages. The first involves formation of bonds and "necks" between touching particles, and a minor degree of particle rearrangement. The second stage is where most of the densification takes place. Here, most of the grains form into their final shape and diffusion from the particle bulk to the surface, and from the grain surface to a lower energy area (e.g., toward a pore, or away from a stress) occurs. As a result, the interconnected network of pores is either filled or eliminated.

Once the pores are isolated, the final stage of solid state sintering, pore removal, takes place. This stage is significantly slower, and is hindered because the pores and gases within must be removed though the ceramic itself, whereas in the previous step it was removed mostly though the existing pore network. Practical limitations of time and temperature may limit the degree of final pore removal which, in turn, limit the final density or the quality of the ceramic (pores may act as stress concentrators which can reduce the strength and toughness).

If a liquid phase is present at the process temperature, then liquid phase sintering (LPS) results.[101-103] To simplify the understanding of this type of densification process, a ternary phase chart (Figure 2-10) was developed by Kwon and Messing.[103] This shows the area in which liquid phase sintering takes place. Assuming a green body with 40% porosity, and the formation of a liquid volume less than 0.74 V_s, the path to full density and final solidification is shown in Figure 2-10. The three proposed stages of liquid phase sintering are (I) rearrangement, (II) solution-precipitation, and (III) pore removal. The LPS process begins at point "O".

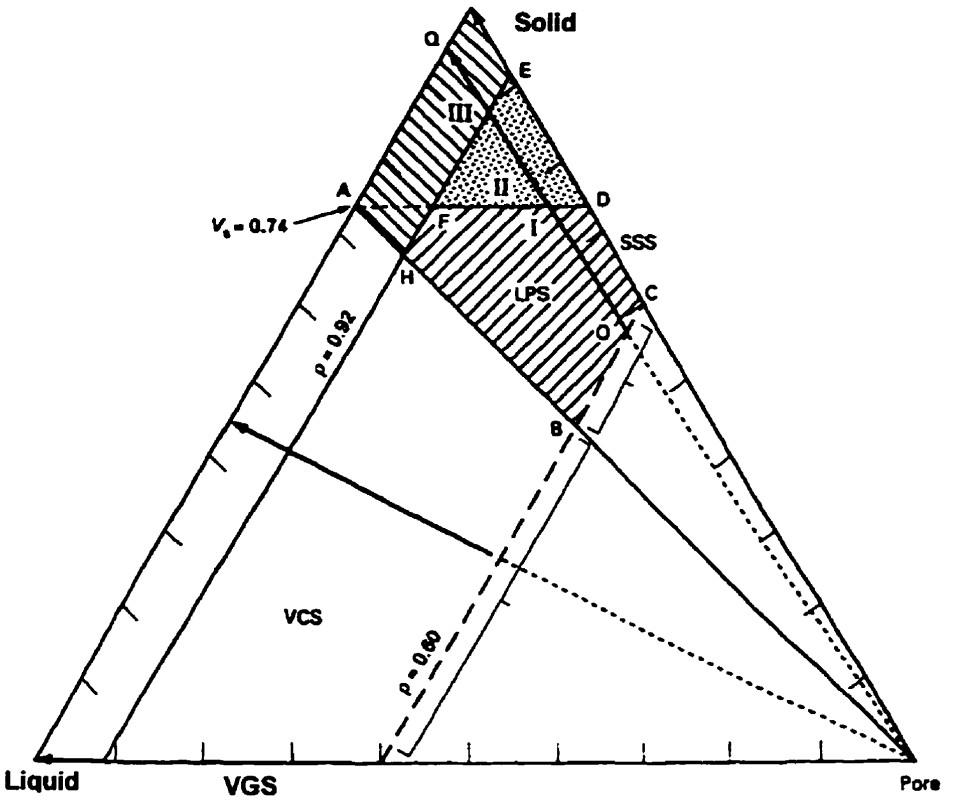

Figure 2-10. Ternary diagram representing solid, liquid and gaseous phases in the process of liquid-phase sintering.[103]

Once the capillary forces rearrange the structure of the solid grains (stage I), stage II begins and chemical concentration gradients become the primary densification driving force. Areas of grains with high surface energy dissolve into the liquid and are relocated into areas with lower concentrations of the constituent (Figure 2.11(a); path 1). Once there, the liquid either remains (filling up a pore, for instance) or precipitates onto a lower surface energy area of a grain. In paths 2 and 4 liquid constituents are driven from pore areas to grain contact areas. The last possibility, path 3, involves relocation of solid by

local dissolution - re-precipitation. The corresponding concentration gradients are shown in Figure 2.11(b).

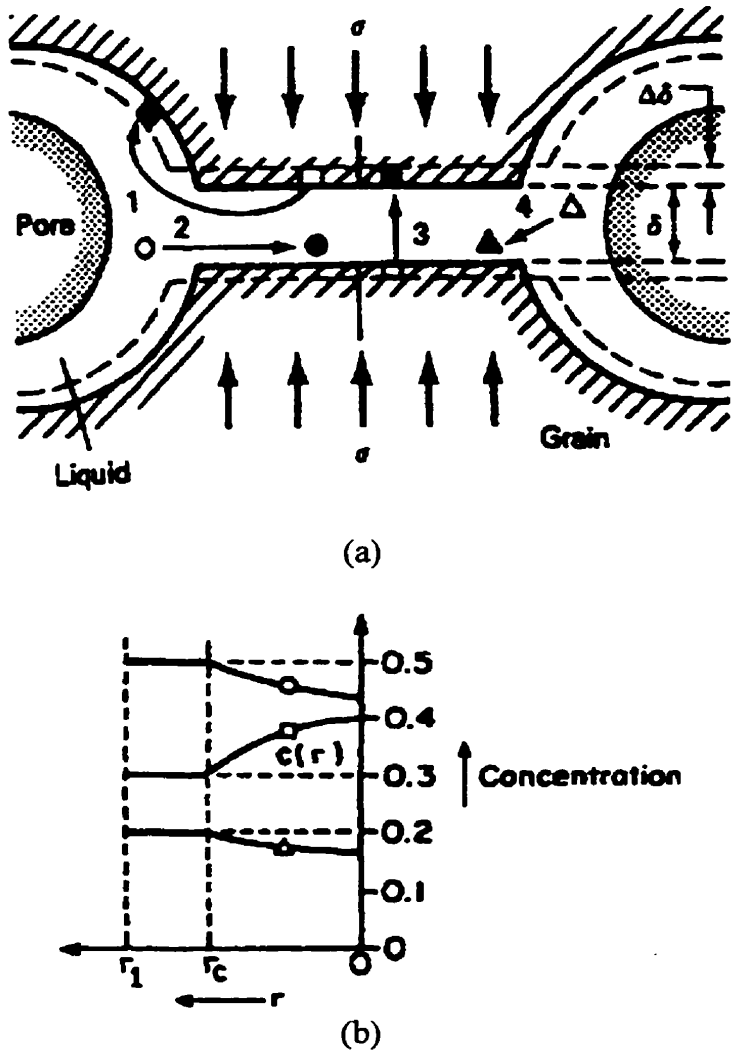

Figure 2-11. (a) Mass transport paths possible during liquid-phase sintering; (b) corresponding concentration gradients (r represents distance).[103]

In this way, certain LPS ceramics, particularly the system being studied, produce grains with defined morphologies; in the case of alumina in a lime - alumina - silica liquid, the alumina grains take on a lath or plate-like shape [16-22].

Creation of ceramics using liquid processing is common in silicate-based systems. To ensure high strength, the resulting glass phase is crystallised using a post-sintering heat treatment involving formation of crystal nuclei within the glass, followed by crystal growth at a slightly higher temperature (Figure 2-12). This method will be utilised in this study to crystallise the glass resulting from the liquid phase present during the sintering stage.

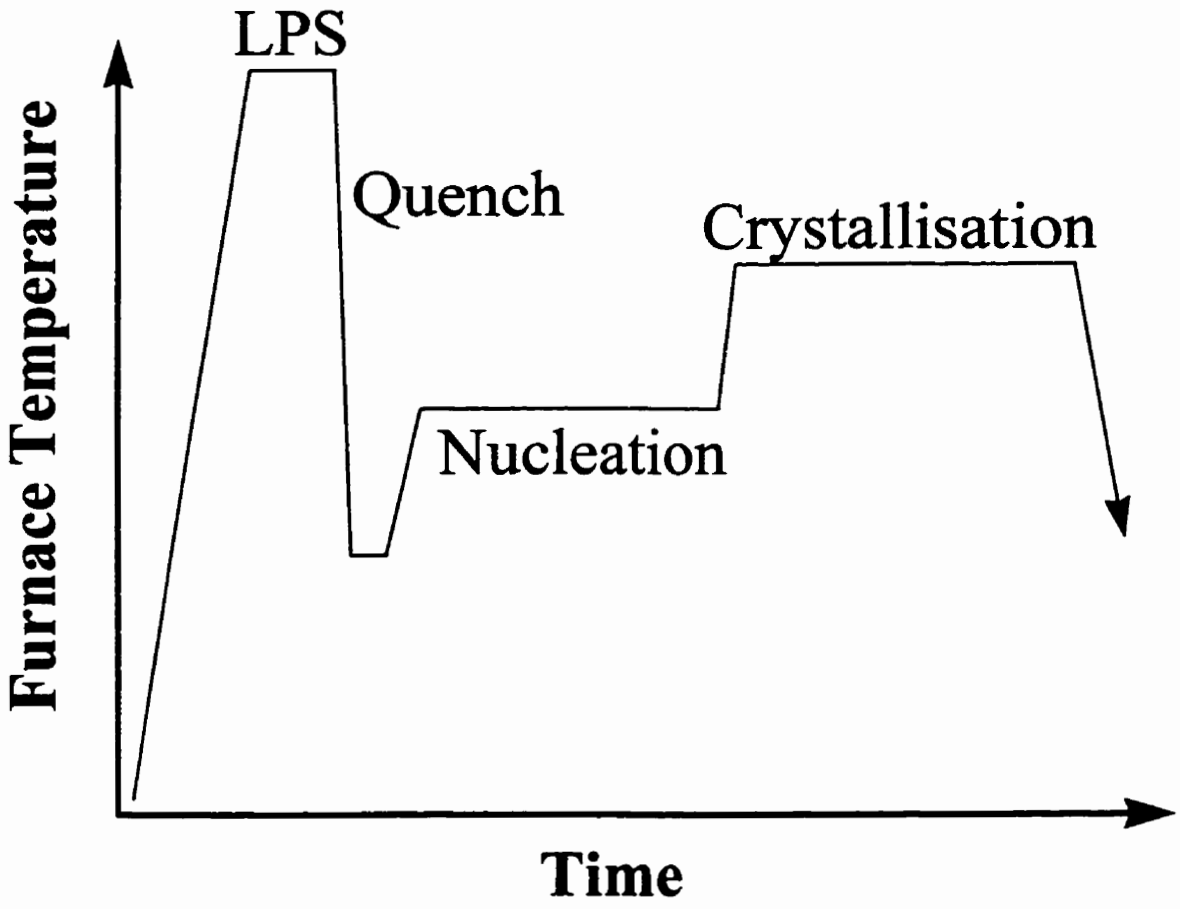

Figure 2-12. A typical processing treatment for (high temperature) liquid-state ceramic production.

2.5.1 Thermal Analysis

Thermal analysis is useful in understanding high temperature processes as chemical reactions can be identified, along with the temperatures at which they occur. Thermal analysis methods used in this study involve monitoring temperature changes (differential

thermal analysis) or weight changes (thermogravimetric analysis) as a sample is heated.[78]

2.5.1.1 Thermogravimetric Analysis (TGA)

Thermogravimetric analysis measures changes in sample mass as temperature is increased. This technique identifies reactions in which a volatile products are created. In the specific case of the alumina-wollastonite system, it is limited to showing burn-off of an organic residue which originated during beneficiation of the wollastonite, or production of a liquid phase which interacts with the surrounding atmosphere. Other TGA phenomena do not apply (e.g., dissociation of a solid compound).

2.5.1.2 Differential Thermal Analysis (DTA)

Differential thermal analysis is a technique which monitors changes in temperature compared to a stable sample, as both are heated at a set rate. Reactions within the material can cause heat to be absorbed or given off; leading to a decrease or increase in the temperature with respect to the standard. By monitoring temperature differences, endothermic and exothermic reactions are observed and the temperature at which they occur is found. When reactions are anticipated at high temperatures, it is helpful to find the precise temperature at which the reactions take place. This is because reaction kinetics may be slow so the sintering schedule can be adjusted to remain at reaction temperatures until reactions are complete.

A new use of DTA was developed recently for research involving devitrification of a glass.[74-77] The devitrification process involves two distinct stages: nucleation and crystal growth. Both of these have optimum rates for specific ranges of temperature (Figure 2-13). Often, DTA is able to establish the crystallisation temperature since the change of phase involves production of heat (latent heat of fusion). However, the development of nuclei inside the glass involves no detectable heat gain or loss.

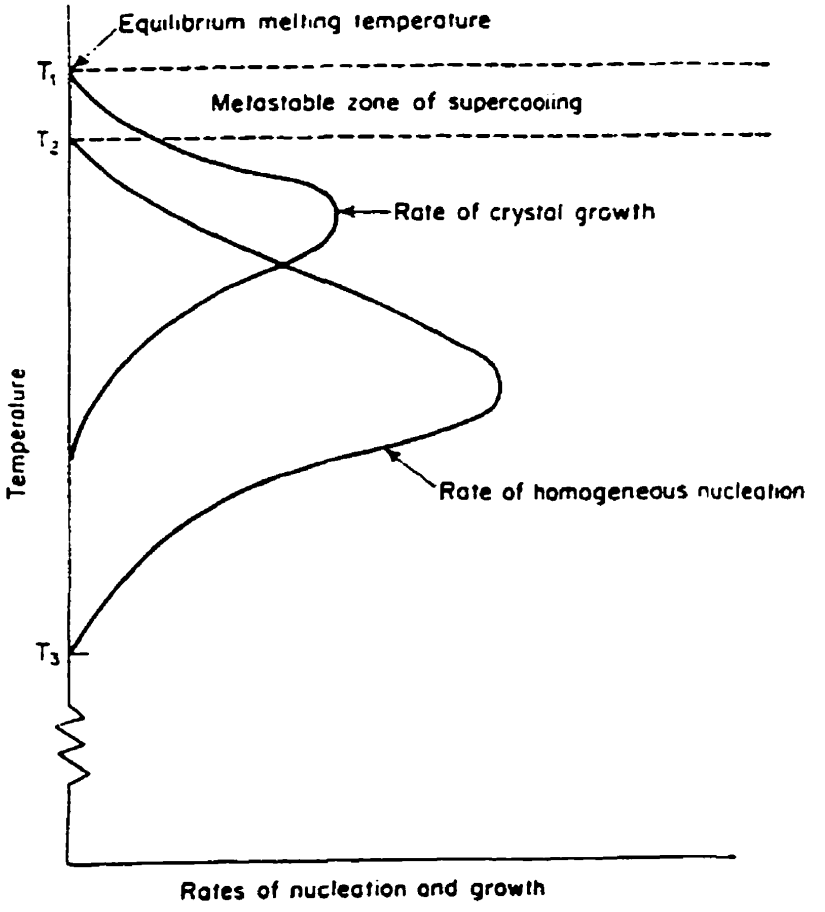

Figure 2-13. Rates of nucleation and crystallisation as a function of temperature.[24]

Indirectly, the nucleation process can be elucidated by DTA. Crystallisation can be promoted and accelerated by the presence of a large concentration of nuclei. Conversely, the dissolution of bulk nuclei can drastically inhibit crystallisation of the glass. Thus, by monitoring changes in the crystallisation peak when preceded by different nucleation treatments, the optimum nucleation temperature can be found.

These changes can be measured in four ways: peak height [75,76], peak breadth [75], peak shift [74,76], and cumulative peak area (reflects a combination of the previous three). When the optimum nucleation temperature is approached, the greater quantity of nuclei will cause a higher crystallisation peak magnitude, over a shorter temperature range (breadth) and crystallisation will occur at a lower temperature. Should the nucleation temperature be too high, nuclei will dissolve and the peak exhibits behavior characteristic of a non-nucleated glass.

2.6 Properties

Once the ceramic is prepared it is necessary to evaluate relevant material properties. Those chosen for study depend on the anticipated microstructures. For instance, if a dense, crystalline product has entrained ceramic whisker shaped grains, then mechanical properties such as strength and toughness would be essential topics for evaluation. However, a porous ceramic with extensive glass phase might have favorable dielectric or thermal shock properties.

Since the material under investigation is anticipated to have a high density, due to liquid phase sintering, and has a fully crystalline nature after processing, then mechanical properties, such as tensile strength, modulus of elasticity, and Poisson's ratio are of prime interest. As well, knowledge of the thermal expansion coefficient gives a useful indication of a ceramic's thermal shock resistance.

2.6.1 Physical Properties Characterisation

To rationalise and explain the mechanical performance, it is necessary to report on various physical aspects of the material. In particular, what the ceramic is composed of (X-ray diffraction), what the microstructure is like (microscopy) and how dense the material is (bulk density measurement).

2.6.1.1 X-ray Diffraction

To determine the actual compounds formed in the ceramic product, it is common practice to make use of an X-ray diffraction unit which projects a filtered beam of a specific wavelength at the sample and a "sweep" is made whereby the beam is reflected off the sample over a range of angles. The detector picks up variations in intensity of the reflected beam which are translated into a strip chart of "intensity" vs. "angle". By noting at which angle peaks occur, one can determine the atomic spacing of the crystals present in the microstructure (Bragg's Law).[104] Lattice spacings of numerous compounds are indexed according to relative intensities of the peaks found. Thus a "fingerprint" of each phase present in the structure is generated.

2.6.1.2 Bulk Density

Measurement of bulk density is performed using Archemedes' principle of buoyancy which states that when a body is immersed in a fluid, its apparent loss in weight (upthrust) is equal to the weight of fluid displaced. The reported theoretical densities of the relevant compounds are given in Table 2-1.

Table 2-1. Theoretical densities for selected oxides.[105] CAS Glass density estimate based on published values for a silica-rich CAS glass.[51]

Material	Alumina Al_2O_3	Wollastonite $CaO{\cdot}SiO_2$	Hibonite $6Al_2O_3{\cdot}CaO$	Anorthite $CaO{\cdot}Al_2O_3{\cdot}2SiO_2$	Gehlenite $2CaO{\cdot}Al_2O_3{\cdot}SiO_2$	CAS glass
$\rho_{theoretical}$ [g/cc]	3.98	2.7-2.9	3.9	2.73-2.76	3.03	≈2.6

2.6.2 Mechanical Properties Characterisation

Material properties such as Young's modulus and Poisson's ratio are important parameters which can easily be measured using ultrasonic techniques. Other structural properties which are of interest in this thesis are the indentation fracture toughness, hardness, and modulus of rupture (MOR). As well, thermal expansion, though regarded more as a physical property, is of interest for thermal shock consideration. Finally, abrasion resistance can be investigated by combining many of the measured properties.

2.6.2.1 Ultrasonic Measurement

By introducing sound waves into a material's structure while measuring the kinetics of wave propagation, it is possible to determine the shear modulus, bulk modulus, elastic modulus and Poisson's ratio.[106] For this investigation, only the latter two are of direct interest. Polished samples with parallel faces are subjected to measurement by transmitting sound waves through the ceramic using a piezoelectric transmitter/sensor arrangement which, when attached to an oscilloscope, yields information on the speed of sound through the material in the measurement direction. Through this, the above mentioned properties can be calculated.

2.6.2.2 Hardness

Measurement of hardness is performed upon flat polished ceramic specimens under various indentation loads. A diamond pyramid indentor leaves behind a square indent in the surface which can be measured via light microscopy or under an SEM for more accurate analysis. The size of the indent is a direct function of the hardness of the material [83],

$$H_v = 1.85437 \cdot P \cdot d^{-2} \qquad (2\text{-}5)$$

where H_v is the Vicker's hardness, P is the applied load in Newtons, and d is the diameter of the square indent (corner to opposite corner) in meters. It is known that there tends to be some general relation between strength (particularly compressive) and hardness. Thus, a quick hardness test can give a broad indication of the expected strength when related to known materials such as alumina.

2.6.2.3 Indentation Fracture Toughness

Traditionally, fracture toughness of ceramics is performed by four-point bend compression of a single-edge notched bar sample.[81-89] This technique has been supplemented by a fast and easy method using a Vickers indentation unit.[83,85-91] By applying a known force to a ceramic sample using a Vickers diamond, the resulting impression usually generates cracks at the corners of the indent (Figure 2-14).

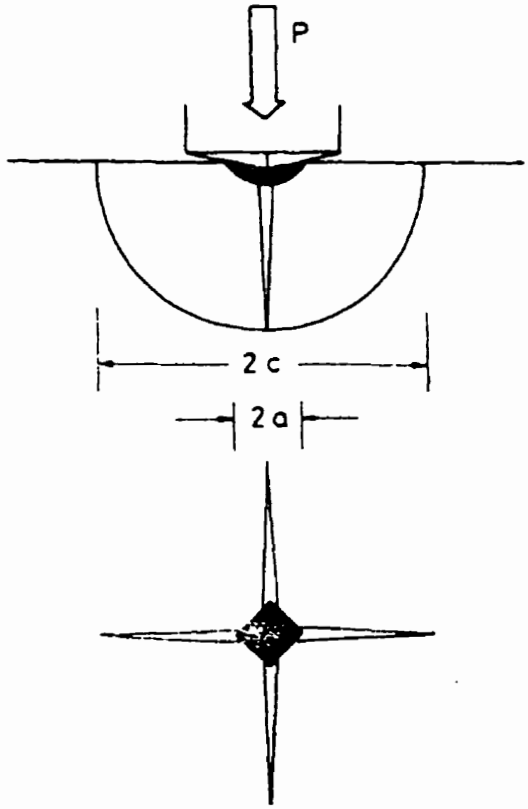

Figure 2-14. Side and overhead representations of crack formations in a brittle material formed during a Vickers indentation.[85] The value a represents half of the indentation diameter (corner to corner) and c is the total crack length measured from the center of the indent.

By measuring the length of the cracks, the size of the indent and knowing the force used, one can employ various models tailored for specific ceramic types. Five empirical models (developed using physical data correlated with the proposed relation) will be discussed and employed for this investigation, based on recommendations by other authors.[83,85-87] Ponton *et al.* [87] suggested two models for alumina-based ceramics:

(i) *Evans and Charles (EC)*: $K_c = 0.0824 \cdot P \cdot c^{-3/2}$

(ii) *J.Lankford (JL)*: $K_c = 0.0363 \cdot (E/H_v)^{2/5} \cdot (P/a^{1.5}) \cdot (a/c)^{1.56}$

Both models exhibited high correlation to measured K_{Ic} values for alumina ceramics.

Other models which will be used for this study were suggested in a VAMAS round-robin report by Quinn *et al.* [83], for evaluation of ceramic fracture toughness,

(iii) *Miyoshi, Sagawa, and Sassa (MS)*: $K_c = 0.0264 \cdot (E^{0.5}) \cdot (P^{0.5}) \cdot (c^{-1.5})$ a

(iv) *Marshall and Evans (ME)*: $K_c = 0.036 \cdot (E^{0.4}) \cdot (P^{0.6}) \cdot (c^{-1.5}) \cdot (a^{0.8})$

A final model was suggested by Anstis *et al.* [85],

(v) *Anstis, Chantikul, Lawn and Marshall (AC)*: $K_c = 0.016 \cdot (E/H_V)^{1/2} \cdot (P/c^{3/2})$

Each model is expected to give values of toughness which can be related to prepared alumina samples which have well known toughness values. Thus, improvement in

toughness can be used to evaluate the new material should the computed K_c values come under question.

2.6.2.4 Modulus of Rupture

Measurement of ceramic strength is commonly done using bend strength techniques. Tensile tests are rarely done due to the difficulty in machining appropriate ceramic pieces, and ensuring no misalignment during the test. Rectangular bend specimens are much easier to prepare and can be tested without any fear of misalignment of the test structure which would nullify the result.

Three-point bend tests are not relied upon since the application of maximum stress is limited to the volume directly beneath the opposing pin (Figure 2-15(a)) and thus strength values tend to be abnormally high. The most common technique for ceramic strength characterisation is the four-point bend since it applies maximum measurement force over a greater volume of the sample (Figure 2-15(b)) and thus strength-limiting flaws have a much greater impact on the ultimate strength values. The results, although lower than the three-point method, are much more representative of the true strength of the ceramic material.[84] ASTM C 1161-94 [107] is the accepted test procedure for evaluating the ceramic bend strength, also referred to as the modulus of rupture (MOR).

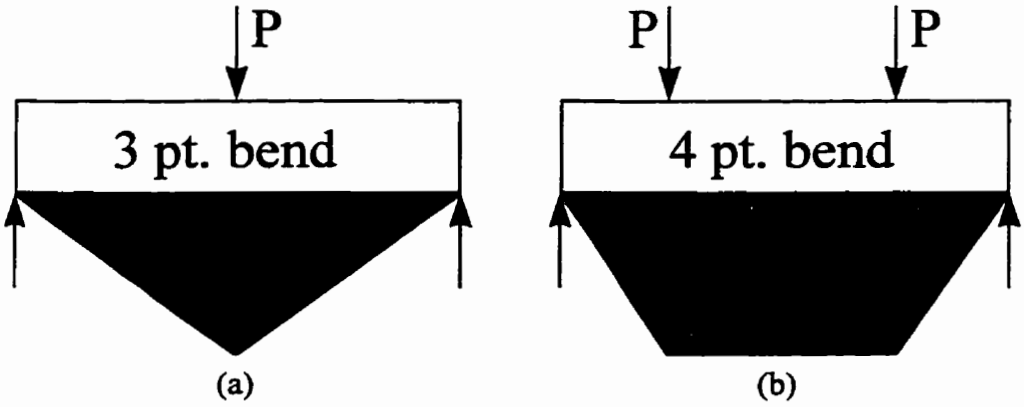

Figure 2-15. Schematic diagram showing applied stress distribution in (a) 3 point and (b) 4 point bend tests.

2.6.2.5 Thermal Shock

Thermal shock resistance need not be measured directly but can be predicted using various physical and mechanical properties. This thermal shock parameter, R, can be used to give an indication of sensitivity of a material to drastic temperature changes [4,108],

$$R = \frac{\sigma(1 - \nu)}{\alpha E} \tag{2-6}$$

where σ is the tensile strength, ν is Poisson's ratio, α is the coefficient of thermal expansion, and E is Young's modulus. The parameter gives an indication of the maximum allowable ΔT for steady heat flow before a crack initiates due to thermal stresses.

2.6.2.6 Abrasion Resistance

Wear properties depend upon many factors involving environmental conditions in which the material is set to perform. Again, this parameter need not be measured directly (since wear data depends upon the application conditions), but can be interpreted through various physical and mechanical characteristics. One interpretation developed for brittle materials found that the critical indentation or groove size, p_{crit}, and critical contact load, L_{crit}, was directly related to fracture toughness and hardness.[109]

$$p_{crit} \propto \left(K_c/H\right)^2 \tag{2-7}$$

$$L_{crit} \propto K_c \cdot \left(K_c/H\right)^3 \tag{2-8}$$

Furthermore, it can be shown that the hardness and toughness character of a material need to be optimised for the given situation. Curves for brittle materials which relate abrasion resistance to material hardness and toughness are shown in Figure 2-16. In region I better wear resistance is obtained with increasing fracture toughness and decreasing hardness. The optimum condition is shown in region II, while in region III high fracture toughness is not as relevant as increased hardness.

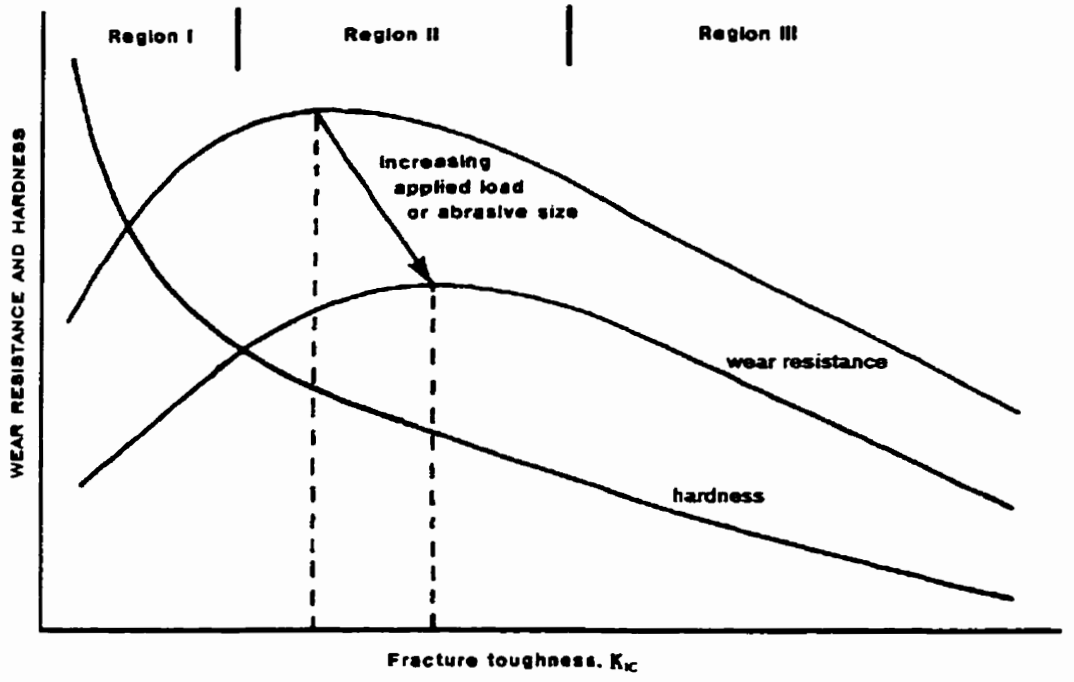

Figure 2-16. Schematic relationship between wear resistance, hardness and fracture toughness.[109]

These relations can be used only as a guide for evaluating material response, however, and true data can only reliably be found by introducing the material in a simulated or real abrasive environment to truly characterise the wear resistance for the given application. Such a rigorous experiment is beyond the scope of this thesis, and evaluations using only models of abrasion of brittle materials will be employed with alumina used as a control.

3. EXPERIMENTAL

3.1 Pre-Processing

Prior to preparing dense aqueous alumina-wollastonite suspensions, each component was subjected to a number of preparatory procedures.

3.1.1 Wollastonite

The wollastonite was obtained from a deposit near Marmora, ON [12] and supplied courtesy of Cominco Ltd. Previous testing [110-111] showed that the acicular nature of the raw wollastonite (Figure 3-1) powder with an aspect ratio of about 10:1, compounded by its large grain size (30 μm) relative to the alumina (0.45 μm) had produced aqueous suspensions with differential sedimentation and an unreasonably high yield stress. This made it impossible to produce a homogenous composite green body. Thus, a grinding operation was deemed appropriate to reduce the size of the large wollastonite grains.

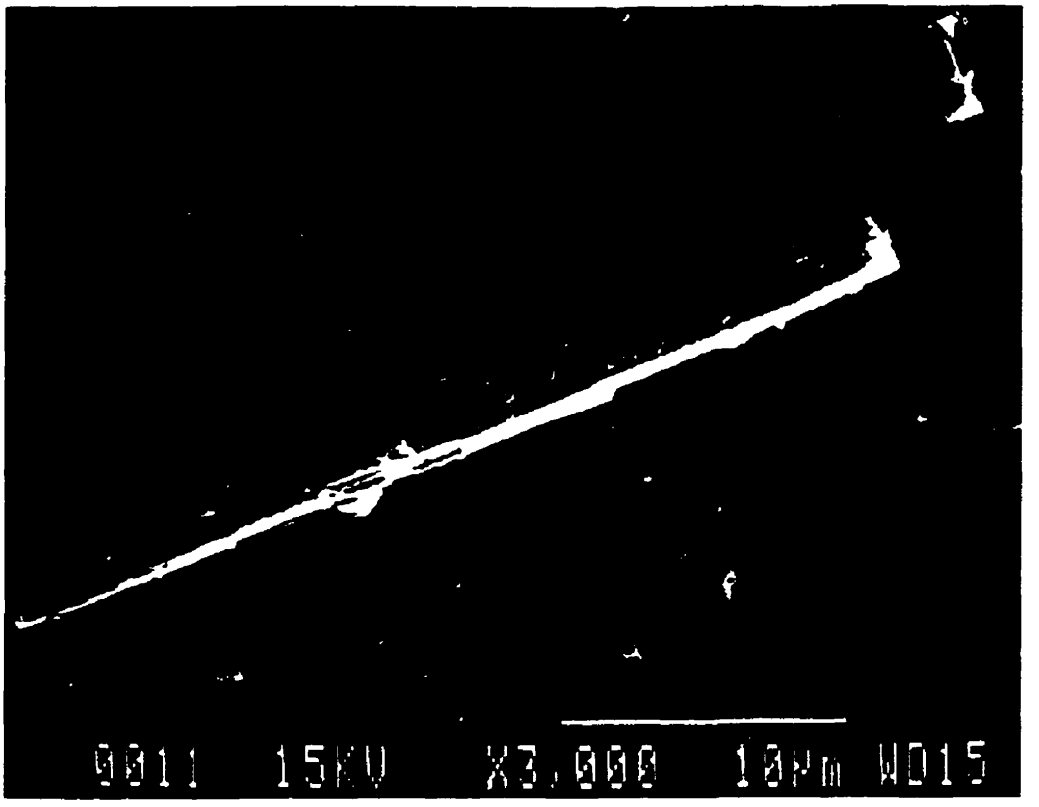

Figure 3-1. Micrograph of wollastonite showing a large, high-aspect ratio grain.

3.1.1.1 Grinding

The chosen size reduction method was to crush the wollastonite using a shatterbox mill with a ceramic-lined mortar and pestle. An effective method to avoid clumping of the mineral during shatterbox crushing was to add a few drops of an acetic acid/methanol mixture to the powder before grinding (a technique used for shatterbox grinding of lime-based ores). Particle size analysis was performed using a Malvern Master Particle Sizer M3.1 (Malvern Instruments, Inc., Southborough, MA) for a series of grinding times to establish the best reduction method.

3.1.1.2 Roasting

The received wollastonite was believed to retain an organic surface residue as a result of the flotation process used during beneficiation. As well, the use of acetic acid and methanol during dry grinding presented the possibility of having unpredictable surface interactions during wet processing. Therefore, a twelve hour roasting stage at 850 C was included to burn off any undesirable organic materials from the particle surface.

3.1.2 Alumina

The as-received alumina powder (Reynolds RC-HP, 0.050% MgO, surface area 8.2 m^2/g; Reynolds Inc., Bauxite, AR) was felt to be ready for processing, although hard agglomerates larger than 5 μm (usually resulting from calcination during production) were removed by sedimentation during the wet-processing procedure (see §3.2.1).

3.2 Wet Processing

As outlined earlier, the most versatile ceramic body formation technique is via wet processing and slip casting. This involves preparing a particle suspension, often using water as the fluid medium, and optimising the dispersion before slip casting. To find the optimum conditions it is necessary to perform various rheological experiments, in this case sedimentation and viscosity measurement, on prepared suspensions.

3.2.1 Suspension Preparation

(a) Alumina Suspensions

Alumina (500 g; 0.45 μm average particle size) was mixed with 0.5 L of deionized water treated with 0.4 mL HNO_3 using a high speed blender, producing a suspension of approximately 0.20 vol. fraction solids. This suspension was pH adjusted to ~4.

It was desired to remove agglomerates to improve the quality of the post-sintered microstructure. A 5 μm limit was felt reasonable to remove the most threatening agglomerates without losing a significant proportion of the finely dispersed alumina. Using Stokes' Law as an estimate [105,112],

$$time = \frac{9\,\eta_{water}\,d}{2ga^2(\rho_{alumina} - \rho_{water})} \qquad (3\text{-}1)$$

With a water viscosity, $\eta_{water} \approx 1.0$ mPa·s at room temperature, gravitational acceleration, $g = 9.81$ m/s^2, particle diameter, $a = 5.0 \times 10^{-6}$ m, and given the dimensions of the flat-bottomed container (and thus the height of the slurry, d), a time of 8 minutes for 600 mL of suspension was computed to provide a supernatant free of agglomerates which are greater than 5 μm diameter. The supernatant was drained off and mixed on a planetary mixer (model 2TC, Turbula, Glen Mills Inc., Maywood, NJ) for at least one hour.

(b) Wollastonite Suspensions

The wollastonite suspension was prepared at 0.05 vol. fraction solids (lower than the

alumina slurry due to its strong alkalinity and larger particle size: 4.5 μm average). This was accomplished by adding the wollastonite powder to an appropriate quantity of water which was treated with 0.3 vol% HNO_3 to compensate for the expected shift to high pH with incorporation of the alkaline wollastonite. This mixture was blended at high speed for 1 min and set to mix on a planetary mixer for at least 1 h to ensure complete homogenization.

(c) Composite Suspensions

The wollastonite suspension was directly added to the alumina suspension in a measured proportion (most composite suspensions were prepared to 20 wt% wollastonite - 80 wt% alumina). The new composite suspension was re-adjusted to pH = 4.0, and a polymeric dispersant (if any) was added and set to mix on the planetary mixer for at least 4 h.

Once homogenized, the suspension was centrifuged on a Sorvall superspeed RC-2 (Ivan Sorvall, Inc., Norwalk, CT) centrifuge (~5000 G; 20 min) to remove excess water. The resulting sediment cake was refluidised with the aid of a small amount of water and acid additions and was re-mixed for at least one hour.

3.2.2 Rheological Testing

Many techniques for fluid characterization are available to optimise ceramic suspensions. The rheological tests employed in this study were limited to a simple sedimentation experiment and viscosity measurement (shear stress as a function of shear rate).

3.2.2.1 Sedimentation

A simple technique used by Hirata *et al.* [63] was chosen to obtain an initial indication for the appropriate pH range to work with. Suspensions are prepared at a low solids fraction (0.05 vol. fraction solids) and adjusted to the desired measurement pH using HNO_3 or NH_4OH. Once homogenized, the suspensions are poured into vials of similar dimensions. The overall suspension height is measured and the vial is left stationary for twenty hours. The larger particles or flocculated structures will settle out, forming a noticeable sediment at the bottom of the vial. Sediments of flocculated powders tend to form quickly with very low density, while well-dispersed systems either resist settling out or settle into very dense sediments. Thus sediment height gives an indication of dispersion quality; little or no sediment indicates a well-dispersed system, while a high sediment height suggests poor suspension conditions.

3.2.2.2 Viscosity

Viscosity testing was carried out using a Brookfield LVTDV-II digital viscometer (Brookfield Engineering Labs, Inc., Stoughton, MA), attached to a personal computer for data collection. A BASIC program (Appendix A) was developed to input viscometer data (stress, shear rate, spindle type) and compute a running average and standard deviation for each data point with at least 50 measurements taken during the test (Figure 3-2). The strip chart-type output allowed for monitoring of time-dependent behaviour (e.g., thixotropy).

Measurements were made with a coaxial cylinder arrangement at 25 C using two spindles (SC4-18, SC4-31) and the small sample adapter using 8-10 mL of suspension. Suspension pH, and solid content (weight loss on heating method) was recorded after each run.

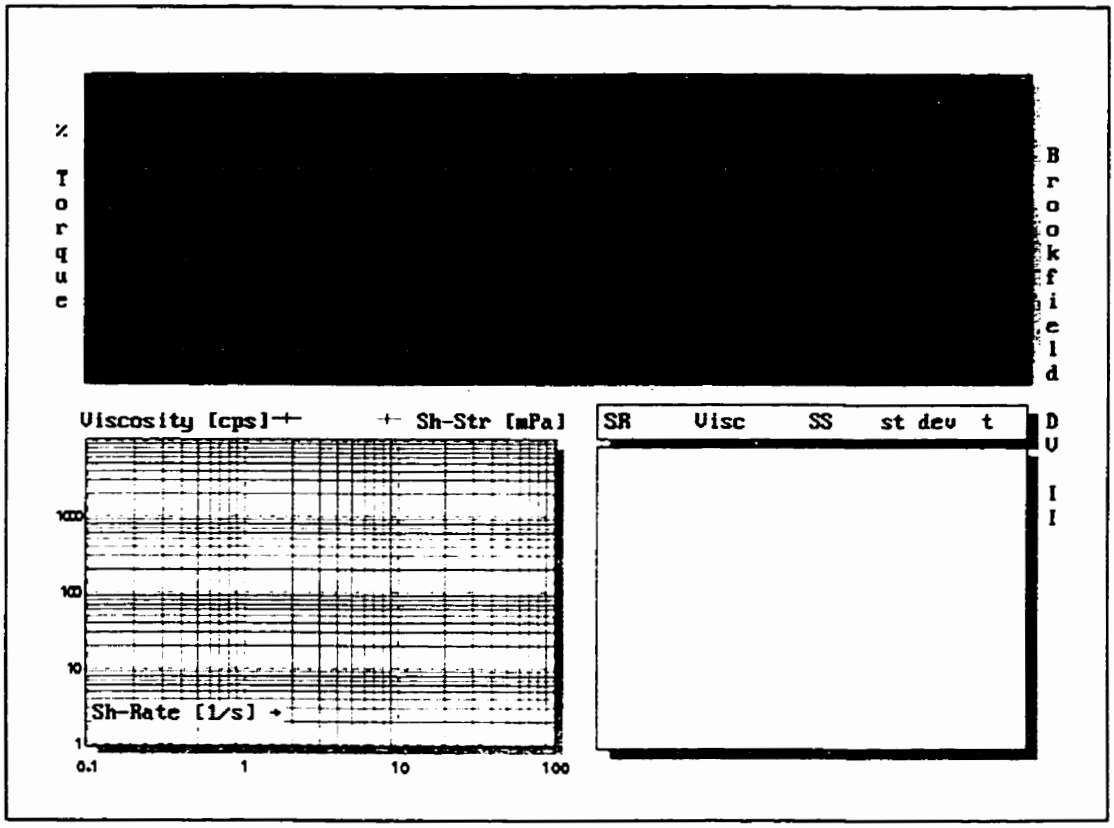

Figure 3-2. Computer output screen showing torque versus time strip chart at the top, log apparent viscosity versus log shear rate at lower left, and tabulated results are displayed at the bottom right during a test.

(a) Shear Rate

Shear rates of 0.10 - 79 s^{-1} were possible using this setup (Table 3-1). At each shear rate, a measured average (>50 readings) of shear stress during at least one full rotation of the spindle was computed along with the standard deviation.

Table 3-1. Shear rates as a function of rpm settings and spindle type for the Brookfield LVTD-II digital viscometer.[113]

	Rpm [min^{-1}]	0.3	6	1.5	3	6	12	30	60
Shear Rate for [s^{-1}]	Spindle 18-R13	0.396	0.792	1.98	3.96	7.92	15.84	39.6	79.2
	Spindle 31-R13	0.102	0.204	0.510	1.02	2.04	5.10	10.2	20.4

(b) pH

As discussed earlier, the interparticle forces, and resulting suspension viscosity, can be tailored by altering suspension ionic conditions (pH). By measuring the viscosity of suspensions having differing pH values, optimization of the suspension pH can be performed.

Adjustment of pH was performed by addition of HNO_3 (nitric acid) to shift to acidic conditions, or NH_4OH (ammonium hydroxide) to move toward alkalinity. The suspensions were fully homogenized and equilibrated before being measured. The pH was recorded directly after completion of the viscosity characterization.

(c) Dispersant

For the study of the effect of dispersant additions, polyelectrolytes were added before pH adjustment to ensure consistent interaction of the polymers with the particle surface. Each dispersant was tested over a wide range of concentrations at the optimized suspension pH. Once the appropriate concentration was found, the pH was "re-optimized" using the new concentration of dispersant.

Based on work by other researchers [114-120], several anionic polymeric dispersants were chosen for evaluation for the alumina - wollastonite composite suspensions. Of those, preliminary work showed that Darvan C (ammonium polymethacrylate; MW=8,000-10,000 Daltons; R.T. Vanderbilt Corp., Norwalk, CT), Darvan 821A (sodium polymethacrylate; MW=8,000-10,000 Daltons; R.T. Vanderbilt Corp), Dolapix PC-75 (structure unpublished; Zschimmer and Schwarz GmBH & Co., Germany), and Emphos CS361 (structure and source indeterminable) showed the most promising results even at concentrations as low as 10 ppm (with respect to solids).

Recent publications [121-122] suggested that a high concentration (up to 3000 ppm) of a cationic polyelectrolyte, BETZ 1190 (quaternized polyamine epoxychlorohydrin; MW=10,000-12,000; Betz Metchem, Horsham, PA) is effective in dispersing composite suspensions by moving the isoelectric point of each of the solid powders well out of the dispersed suspension pH ranges, thus minimizing heteroflocculation (dissimilar particle attraction). Therefore, this polymer was also investigated in this study.

3.2.3 Green Body Testing

Verification of the quality of a dispersion was done by simply creating a green body through slip casting the suspension used in the viscosity experiments. The density of the consolidated bodies was a clear indicator of the suspension quality.

3.2.3.1 Slip Casting

Dissolved and entrapped air needed to be removed from the suspension before casting to avoid voids in the green body. Figure 3-3 shows the degassing apparatus used. The suspension was sealed in the flask and air was evacuated using an aspirator attached to a water tap. After bubbling had subsided, the system was vented and the suspension was carefully handled to avoid further introduction of air by turbulent action or mixing.

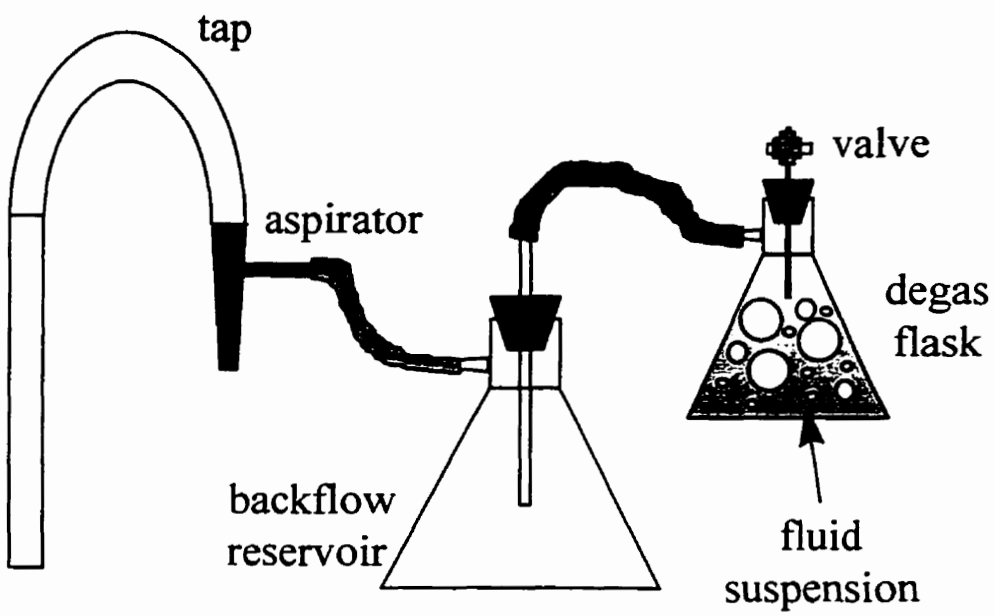

Figure 3-3. Diagram of degassing apparatus used to remove entrapped or dissolved air within the suspension.

Slip casting was performed on plaster plates using 2.5 cm plastic rings to contain the slurry. Consolidation time depended on the conditions of the slip. Once casting was complete the green bodies were oven dried at 110 C for at least 2 h.

3.2.3.2 Density Measurement

Green density measurements were performed using a mercury densitometer (Archimedes method).[123] Measurements were carried out according to pH and dispersant conditions of the suspension. This was done by fully immersing the sample in mercury and measuring the change in mass of the sample. By knowing the temperature, the density of the mercury, and the change in mass, the volume of the displaced mercury (i.e., sample

volume) can be calculated,

$$\rho_{bulk} = \frac{W}{(W - I)\rho_{mercury}} \tag{3-2}$$

where ρ_{bulk} is the bulk density, W is the weight in air, I is the weight when suspended in mercury, and $\rho_{mercury}$ is the density of mercury at the measurement temperature.

If the densities and relative amounts of the compounds present in the sample are known, then the theoretical density can be determined. Then the bulk density can be contrasted to the theoretical to yield the percent theoretical density (%TD)

$$\%TD = \left(\frac{\rho_{bulk}}{\rho_{theoretical}}\right) \times 100\% \tag{3-3}$$

which also reveals the amount of porosity present,

$$\%Porosity = 100\% - \%TD \tag{3-4}$$

3.3 Densification

After the green body is prepared, the final production stage is to sinter the body at high temperatures to approach full density and strength. To find the best sintering regime it is useful to perform thermal analysis on the sample under evaluation.

3.3.1 Thermal Analysis

Thermal analysis of this system included equilibrium phase prediction using a thermodynamic software program combined with thermogravimetric analysis and differential thermal analysis.

3.3.1.1 Thermodynamic Considerations (F*A*C*T)

Thermodynamic calculations were facilitated by the use of F*A*C*T software.[124] By setting up a half-reaction equation corresponding to the starting materials before sintering, the expected equilibrium products can be found when the temperature and pressure are specified. The program relies on thermodynamic data from an extensive chemical database.

3.3.1.2 Thermogravimetry

Measuring the change in mass as a function of temperature can reveal important reaction temperatures, such as the formation of a liquid phase, which causes a loss in weight due to volatilisation. The instrument (CAHN TG-171) was ramped at 10 K/min from room temperature up to 1600 C. The sample was placed in a small alumina reaction crucible and suspended within the vertical furnace.

3.3.1.3 Differential Thermal Analysis

Alumina powder was sintered in a small, narrow - necked alumina crucible (6 mm dia.) with a 0.010" R-type thermocouple embedded in it, thereby forming the reference

junction. The samples were an 80 alumina - 20 wollastonite mixture of similar mass (1.6 g), dimensions and configuration as the reference. The set-up is shown schematically in Figure 3-4.

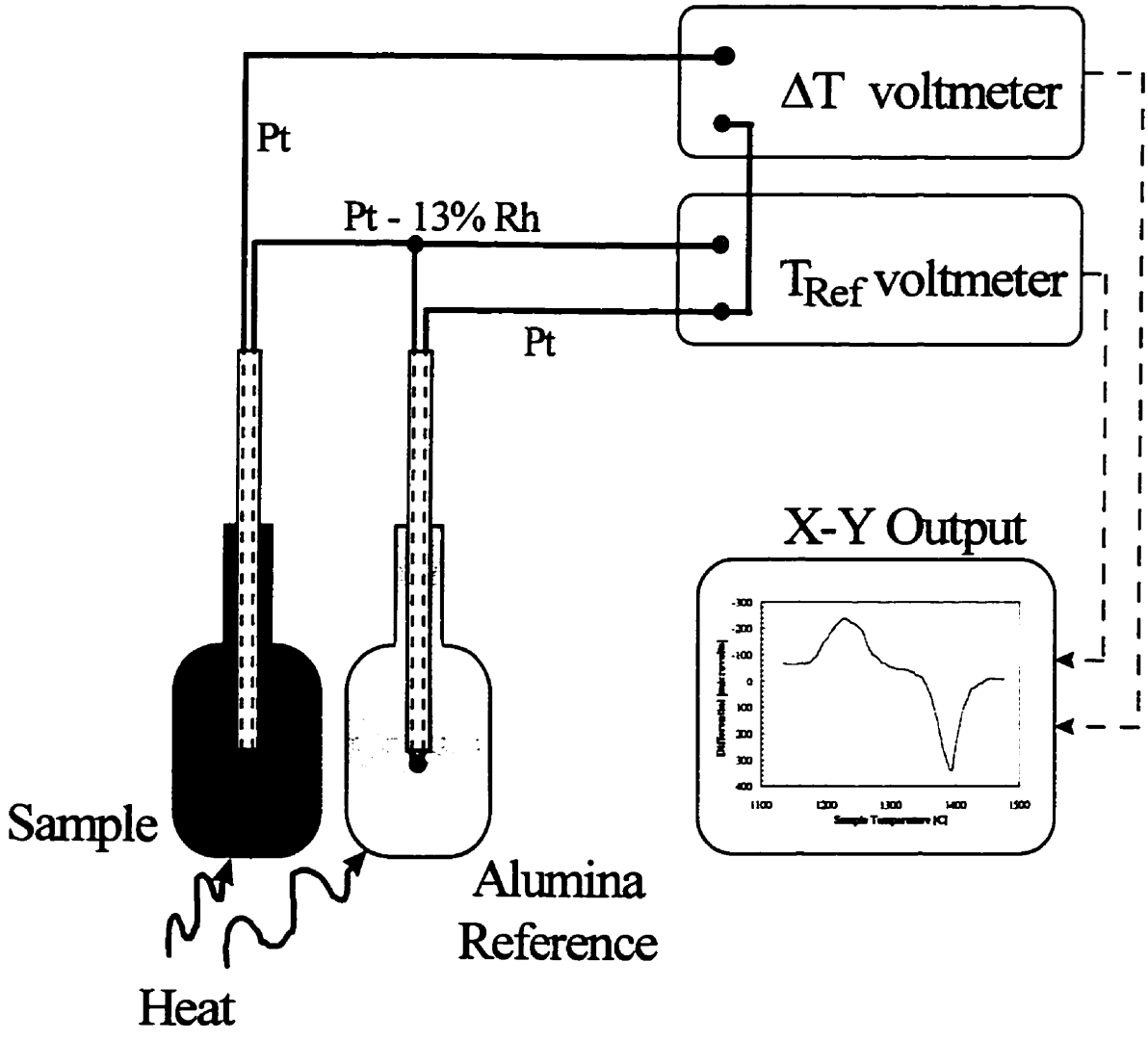

Figure 3-4. Schematic diagram of DTA setup showing narrow-neck sample crucibles and wiring plan.

The platinum wires of each probe served as the ΔT voltage input, measured using a millivoltmeter. The voltage of the reference thermocouple, corrected for ambient temperature, was measured concurrently to produce a ΔT versus T output graph. Ramp rates were maintained at 0.41 $K \cdot s^{-1}$ for every run. The technique for defining the peak temperature from a DTA scan suggested by Todor [79], was employed. This method entails creating a line representing the background level of the scan as well as an intersecting best-fit line through the linear portion of the leading edge of the peak (Figure 3-5). The intersect temperature at point C is taken to be the true peak temperature.

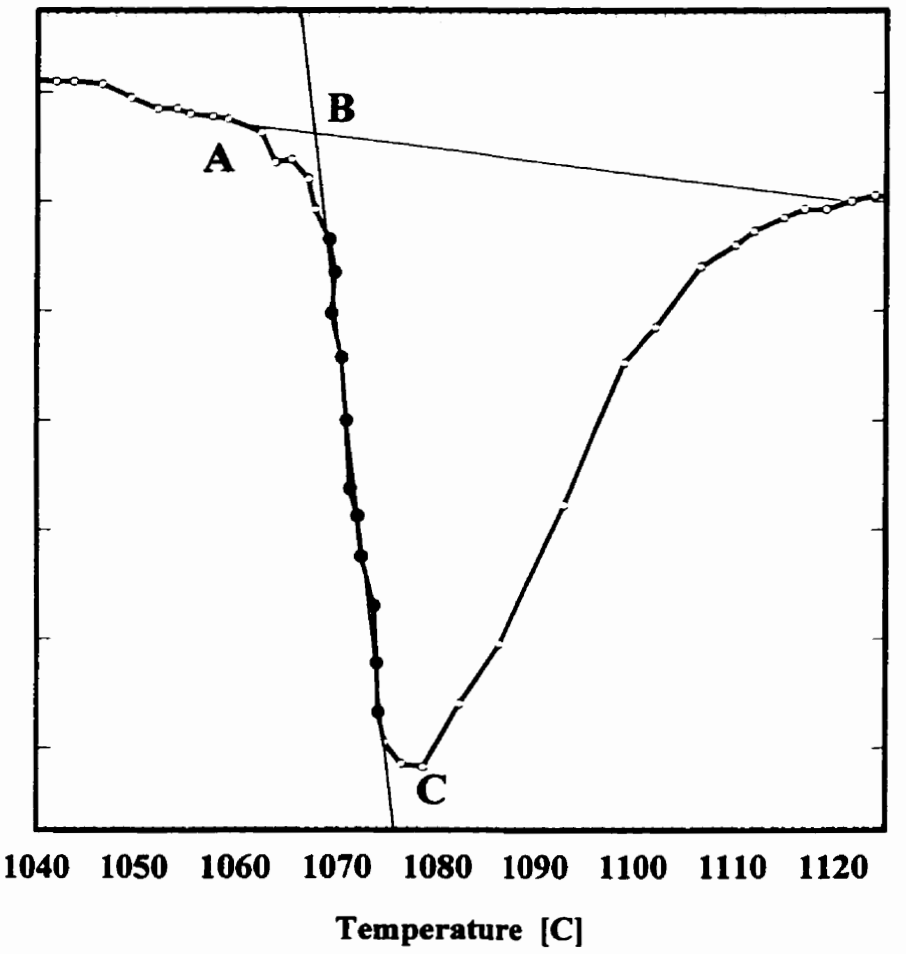

Figure 3-5. Sample DTA plot showing selection of peak temperature: initiation of peak at A; intercept between background level and best-fit line at B; and peak maximum at point C. The vertical axis represents differential temperature in arbitrary units.

This method is preferred since it is not sensitive to differences in heating rates, which skews the shape of the peak and shifts the peak maximum (Figure 3-6). Calibration runs were performed using K_2SO_4 which undergoes a structural transformation at 585 C and

melts at 1069 C. Several runs were performed to demonstrate that the DTA was highly accurate over a broad temperature range (Table 3-2).

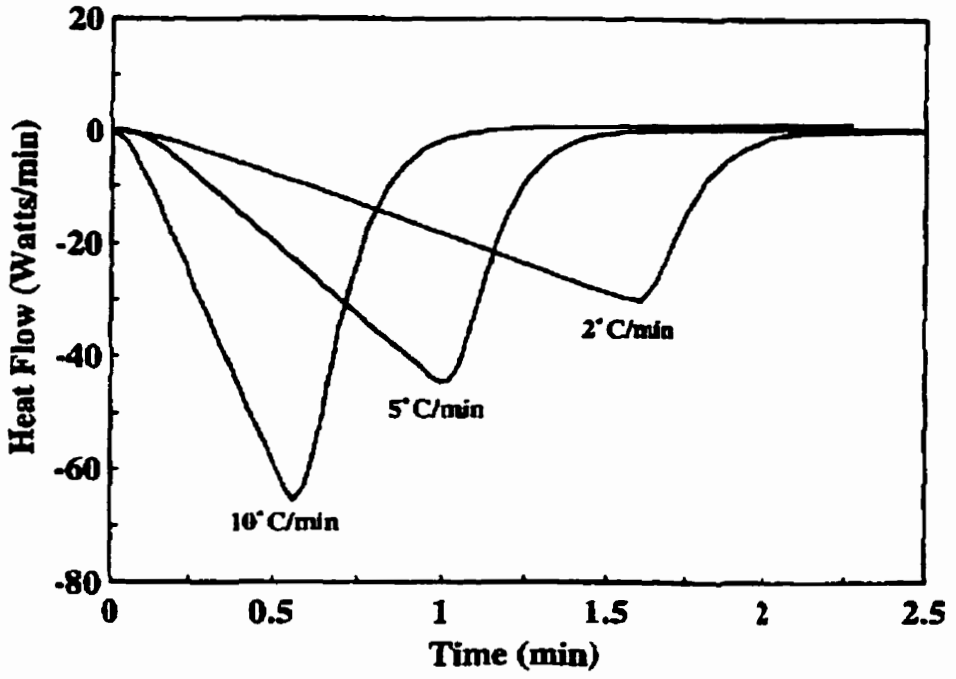

Figure 3-6. DSC curves which illustrate the effect of heating rate on thermal analysis peaks.[78]

Table 3-2. DTA calibration results using K_2SO_4 as a standard. Actual temperatures reported from reference.[79]

Calibration Experiment	K_2SO_4 Structural Transformation Peak Temperature [C]	K_2SO_4 Melting Peak Temperature [C]
run #1	585.0	1069.5
run #2	n/a	1066.0
run #3	584.1	1067.8
average	584.6	1067.8
actual	583 ± 2	1069.1 ± 0.3
% error	≈0	0.1

Reaction stages consisted of one hour ramps to 1510 C followed by an air quench (accomplished by removing the samples from the hot furnace). Two hour nucleation treatments were included in the secondary ramp schedule, after which the DTA scans were performed. A schematic drawing of the experimental furnace schedule is given in Figure 3-7.

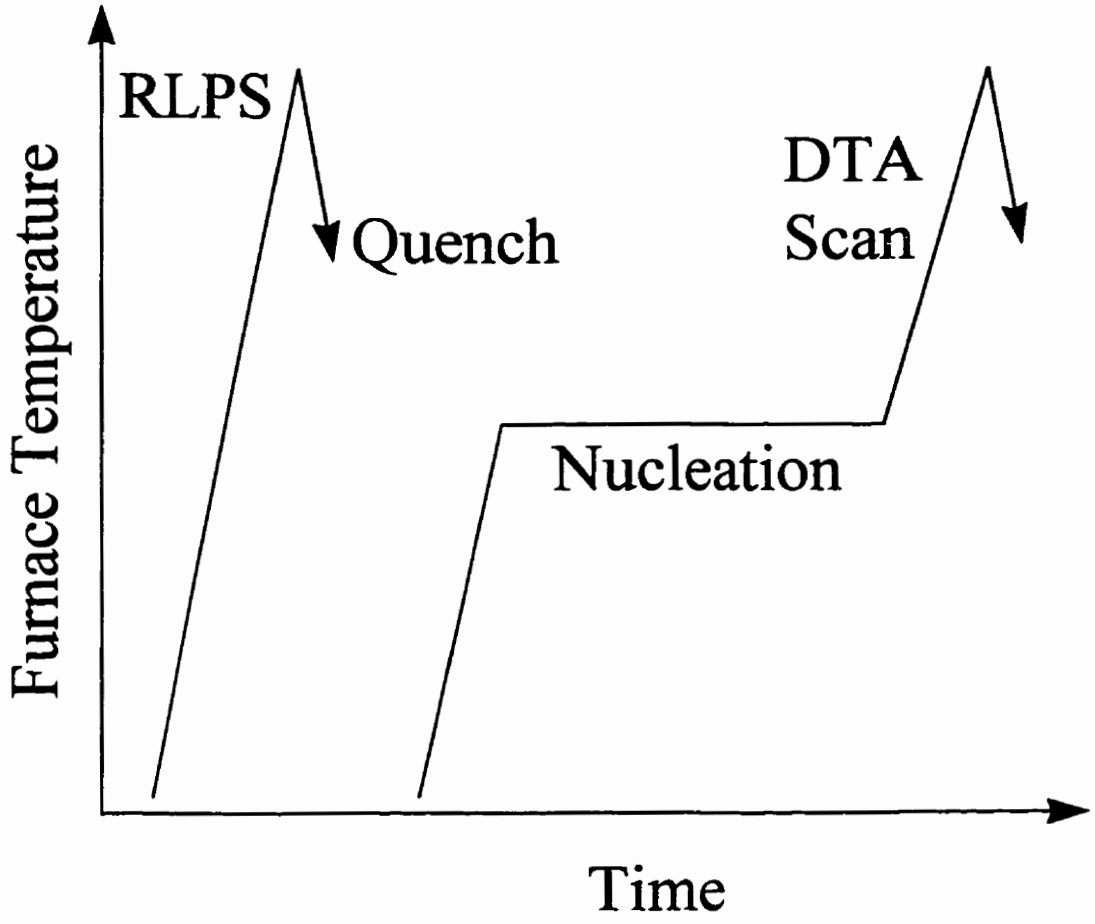

Figure 3-7. Schematic diagram representing the furnace schedule used for DTA nucleation temperature determination.

3.3.2 Sintering / Devitrification

The furnace employed for the sintering and devitrification procedures was a Lamont elevator furnace having an approximate volume of 0.031 m^3, using 20 $MoSi_2$ heating elements (Figure 3-8). A monitoring R-type thermocouple was added to the base near to where the samples were sintered so that a close estimation of sintering temperature could

be made (Figure 3-9).

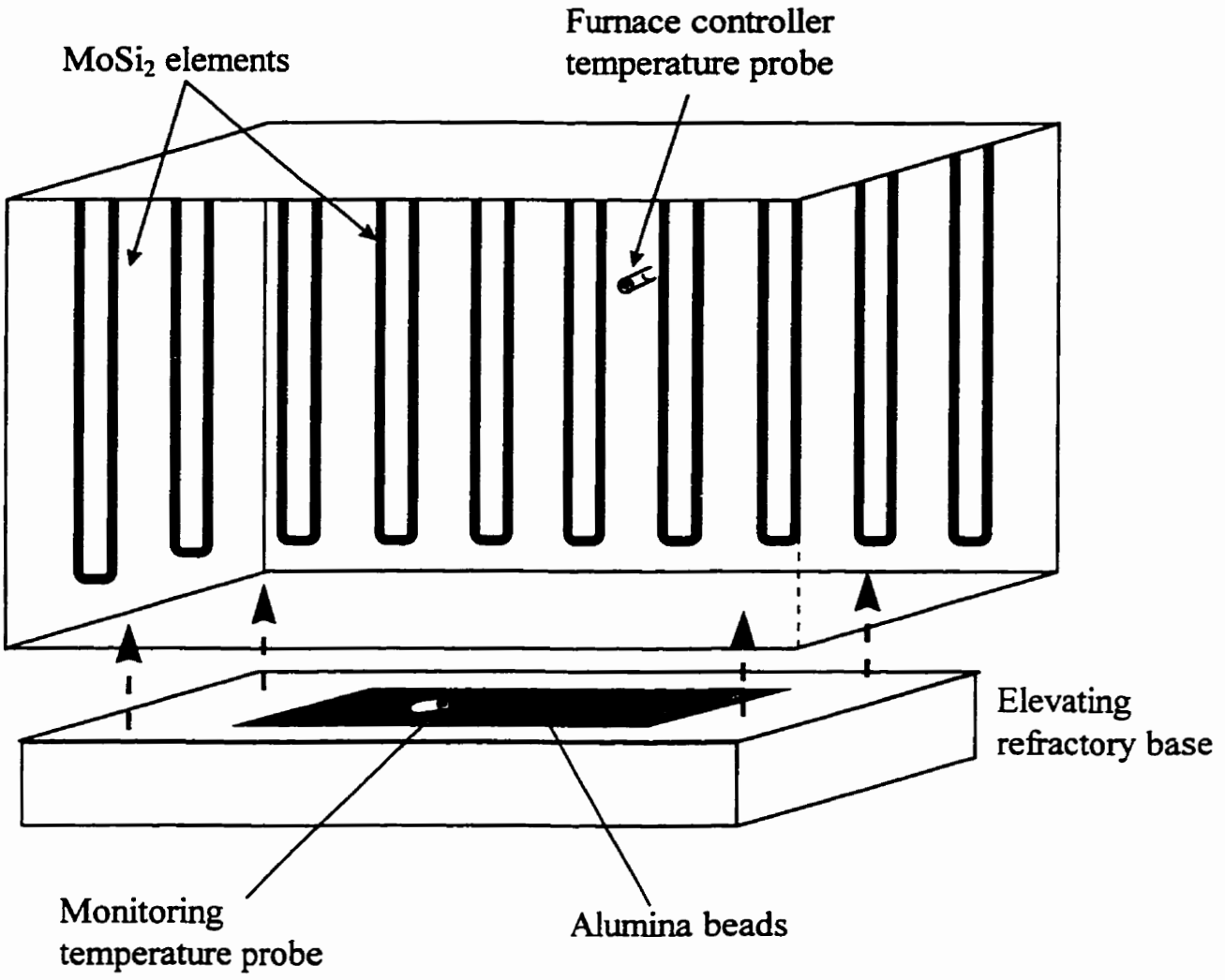

Figure 3-8. Cut-away diagram of the Lamont elevator furnace employed for the sintering and devitrification procedures.

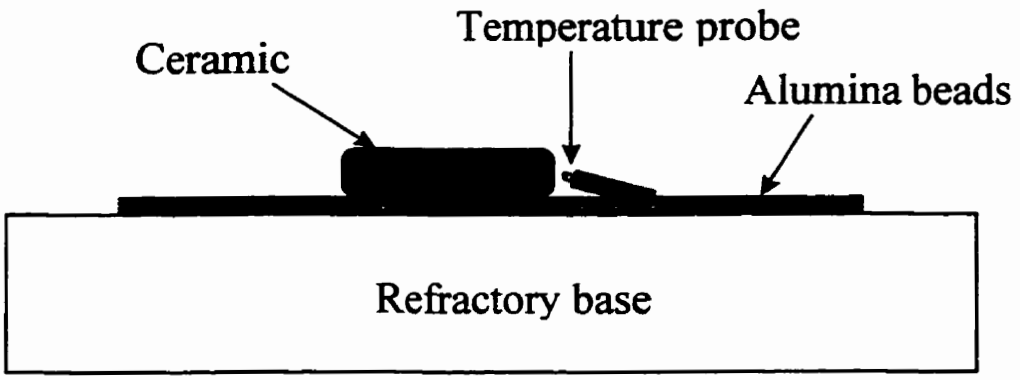

Figure 3-9. Side view of furnace base showing arrangement of ceramic sample and monitoring thermocouple.

Alumina control specimens were ramped to 1560 C at 6.5 C/min and held for five hours, followed by slow cooling. CAS sintering technique was established through DTA experimentation.

3.4 Characterisation

Newly developed materials need to be characterized in terms of the properties which would make it desirable for production. This CAS ceramic is believed to have beneficial mechanical and physical properties which would make it useful in structural applications which currently use more expensive ceramics or metals. As a result, the mechanical strength, hardness, and toughness as well the physical properties such as thermal expansion, microstructure, composition, and density are all of interest.

3.4.1 Physical Testing

To fully characterize the ceramic it was necessary to perform various physical tests including microscopy, electron probe microanalysis (EPMA), X-ray diffraction, dilatometry, and densitometry.

3.4.1.1 Densitometry

Density measurement of sintered ceramics was performed using the same technique described for green body evaluation (§ 3.2.3.2).

3.4.1.2 Microscopy and EPMA

Microstructures are best examined when a ceramic is ground and polished to a smooth finish. This is usually accomplished by starting with a coarse grinding belt, followed successively by finer grinding papers (120 - 600 grit), and finally finishing with diamond polishing on nylon laps with diamond polishing fluids from 9 - ¼ μm. Usually 2 - 10 minutes per step are required to ensure a smooth finish, depending on the hardness of the ceramic. Some further treatment is usually required to enhance visibility of grain boundaries under the SEM. For most ceramics this entails either an aggressive chemical etch (e.g., boiling phosphoric acid) [125] or a prolonged heat treatment lasting several hours at about 50 K below the sintering temperature (thermal etching).[24]

At this point, the sample is mounted on a stub and coated with a thin conductive material (a sputter coating of a gold-palladium alloy, or a light carbon coating formed by an

evaporation technique; both of the order of 10 nm in thickness). Representative micrographs at various magnifications are taken to characterise the microstructural features (e.g., grain size, morphology).

The same samples may also be prepared for EPMA, although a carbon coating is more appropriate for this type of analysis. The probe operates under a similar principle as an SEM although it includes detectors which can measure the X-rays given off when the sample is impinged by a focused 20 kV beam. The detector sends data to a computer which has software to convert beam energies to quantitative amount of elements. Corrections (which assume only the presence of oxides) are accounted for during calibration using oxide standards. Thus the output includes the relative amounts of the oxide compounds totalling 100% by weight. When the totals do not add to 100% it indicates that the area excited by the beam is not flat, not facing the detector, or there is some contamination or beam instability (caused by electrostatic charging of the sample).

This type of analysis is ideal for identifying specific crystalline compounds or glassy phase compositions. Unfortunately, porous and ultrafine grained materials are difficult to reliably characterise using this technique.

Using a Philips X-ray unit with a Cu target and a Ni filter, a monochromatic X-ray having a characteristic wavelength of 1.542 Å impinged the samples. A scan was carried out over a wide angular range (2θ = 15° - 70°) and the intensity of the reflected beam was recorded on a strip chart. The angles at which peaks occur can be translated into d spacings using

Bragg's Law.[104] A series of d spacings are characteristic of only one compound, and can be found using a number of X-ray diffraction data sources.

3.4.1.3 Dilatometry

Measurement of length change as a function of temperature can be performed using a standard dilatometer apparatus to yield the coefficient of thermal expansion, α. Alumina and devitrified CAS samples of 25 x 5 x 5 mm were prepared and measured at a heating rate of 10 K/min using a dilatometer with platinum as a standard. A schematic view of the apparatus is shown in Figure 3-10.

Figure 3-10. Schematic view of the dilatometry apparatus.

3.4.2 Mechanical Testing

Mechanical testing of the CAS ceramic included ultrasonic measurement (elastic properties), Vickers indentation hardness and toughness, and bend strength (modulus of

rupture) measurement. Each procedure is straight-forward and well established in the field of ceramic research.[4]

3.4.2.1 Ultrasonic Testing

Ultrasonic testing was performed upon alumina and CAS ceramic samples which were polished on parallel sides. Three samples of each were measured at a frequency of 10 MHz. The piezoelectric transmitter and sensor arrangement allowed for quick and easy determination of the elastic modulus (E), Poisson's ratio (ν), bulk modulus (K), and shear modulus (G). This is possible by measuring the speed of sound waves transmitted through the material using an oscilloscope.

3.4.2.2 Vickers Hardness

Diamond indentations were made using a LECO V-100A (Leco Corp., St. Joseph, MI) indentation test unit using loads of 5 and 50 kg (49 N and 490 N respectively) with a fifteen second dwell time. Samples were ground and polished to a smooth finish, having parallel top-bottom planes. Indent diagonal measurements were made using a calibrated eyepiece and were checked using an SEM at 1,000-4,000X magnification. The relation for determination of Vickers hardness [83,126], H_v, is

$$H_v = \frac{1.85437 \times P}{d^2} \qquad (3\text{-}5)$$

where, P is the applied indentation load in Newtons and d is the indentation size (corner to corner) in meters.

3.4.2.3 Vickers Indentation Toughness

Indentation of brittle materials allows a fast and useful method to determine the fracture toughness, since the diamond edges tend to generate cracks visible at the polished surface. Various models have been developed to interpret the crack length as a measure of toughness and some review papers discuss the applicability of each. For this study, five models have been selected based on their assessment by review authors.[83,85-87]

1) Evans and Charles (EC) - f(load, crack length),

2) Lankford (JL) - f(load, E, Vickers hardness, indent size, crack length),

3) Moyashi, Sagawa, and Sassa (MS) - f(load, E, indent size, crack length),

4) Marshall and Evans (ME) - f(load, E, indent size, crack length),

5) *Anstis, Chantikul, Lawn and Marshall (AC)* - f(load, E, hardness, crack size).

In all cases it is important to know the applied load and the crack length measured from the center of the indentation. An SEM is useful in getting accurate measurements and so before indentation the sample is polished flat and sputter coated with gold-palladium. The samples are indented and examined as soon as possible in the SEM. Time delay between indentation and measurement is kept as short and uniform as possible (under 20 minutes for SEM measurements) since slow crack growth can decrease accuracy.

Measurement of the size of the indentations (diagonal), d, or the half-indent size, a, (measured from the center to the corner and is thus d/2) is also necessary for many of the

models.

3.4.2.4 Modulus of Rupture

Four point bend testing was carried out according to ASTM standard C 1161-94 [107] (equivalent to MIL STD 1942). Sample configuration B (Figure 3-11) was the chosen setup since it is the most commonly reported of the three sample sizes [82]. The test unit was an Instron model 4502 mechanical tester (Instron Corp., Canton, MA) with strain rate set to 0.50 mm/min controlled using LabVantage software.

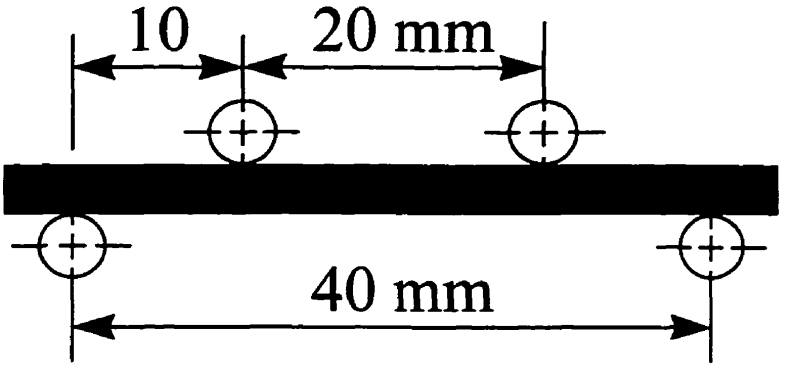

Figure 3-11. Sample configuration (B) for modulus of rupture 4-point flexure test.

Load versus displacement data was collected via a personal computer. Stress (modulus of rupture) and modulus of elasticity calculations were based on simple beam loading equations.[107]

4. RESULTS

4.1 Pre-Processing

Previous work [110,111] showed that the size and shape of the raw wollastonite grains produced composite suspensions with poor casting qualities. The results of particle size analysis of the raw powders are shown in Figure 4-1. As the lower measurement limit of the laser size analysis unit is 1.2 μm, the fine alumina powder is extrapolated on the graph to coincide with the analysis supplied by the manufacturer (average particle size = 0.40 μm). Clearly, with an average particle size of 30 μm, the wollastonite is unreasonably large in comparison with the alumina which causes differential sedimentation rates and hence, non-uniform body composition, and the acicular shape (Figure 3-1) produces a high yield stress [110] which makes a slip cast body with very low density.

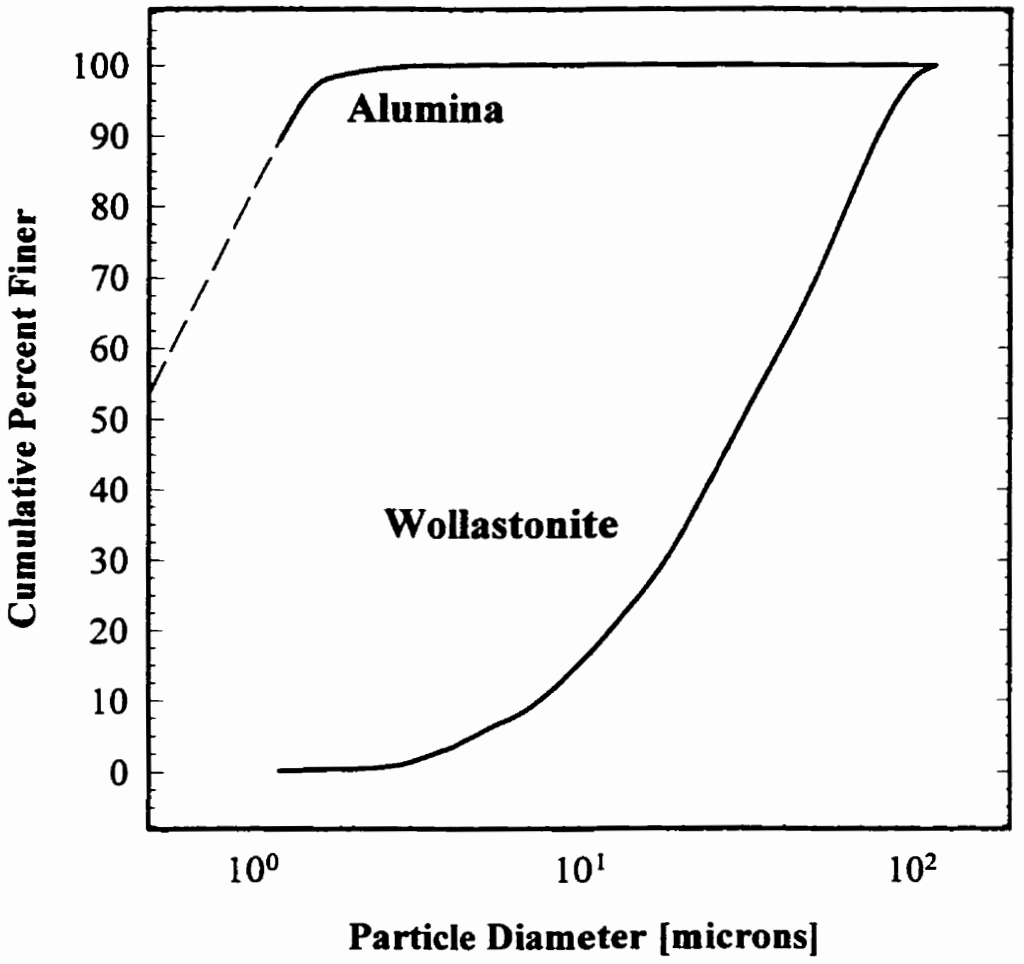

Figure 4-1. Particle size analysis of alumina and wollastonite as-received powders.

A shatterbox unit was employed to further crush the mineral, and a few drops of a dispersant (50% ethanol - 50% acetic acid) was added to the 8-12 grams of wollastonite (per batch) to prevent caking of the wollastonite along the walls of the pestle. The caking of the mineral makes it difficult to remove the processed powder and it is believed to reduce grinding effectiveness. It was found that a log-log relation existed between final particle size and communition time (Figure 4-2). However, longer grinding times tended

to heat up the system which evaporated the dispersant and resulted in caking of the product, and longer times also had less of an effect on size reduction. As a result, 10 minutes was chosen as an appropriate communition time to produce reasonable size reduction (30 μm → 4.5 μm) before heat build-up made processing excessively difficult.

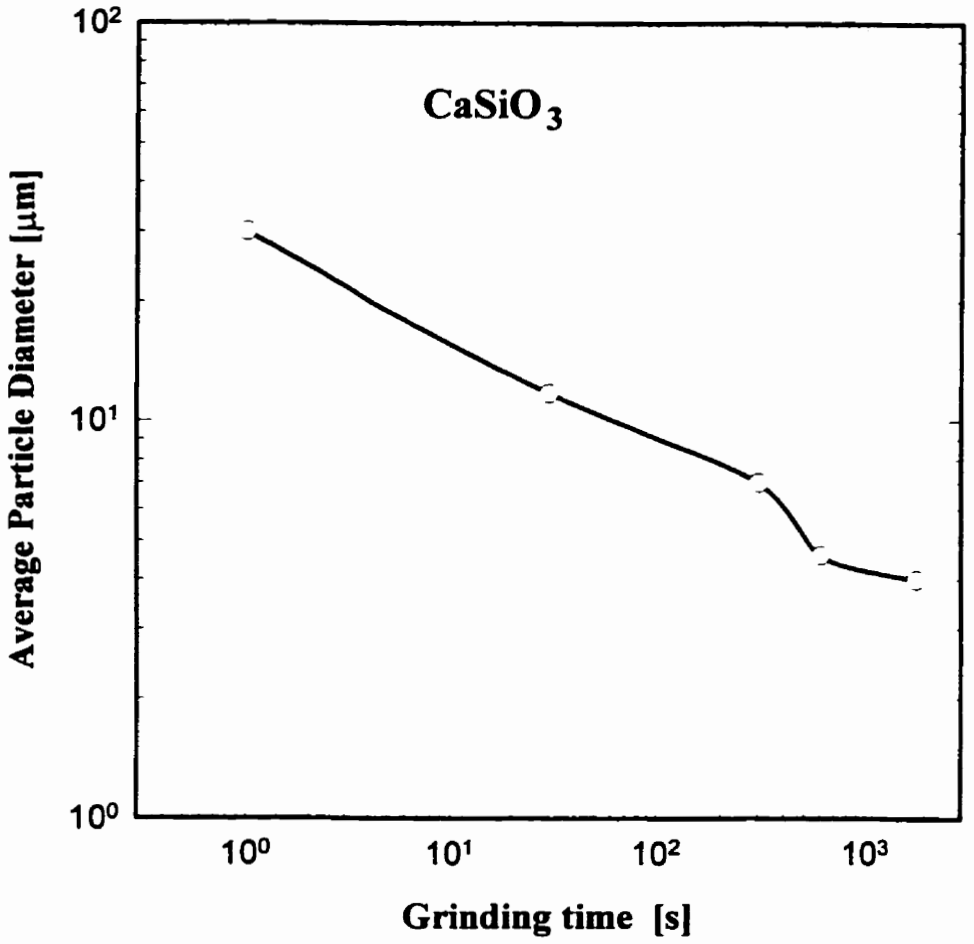

Figure 4-2. Average particle size of wollastonite as a function of grinding time in the shatterbox mill.

As well, the aspect ratio of the commuted grains was greatly decreased from about 10:1 to 3:1 (Figure 4-3) which reduced the possibility of a high yield stress in the suspension.

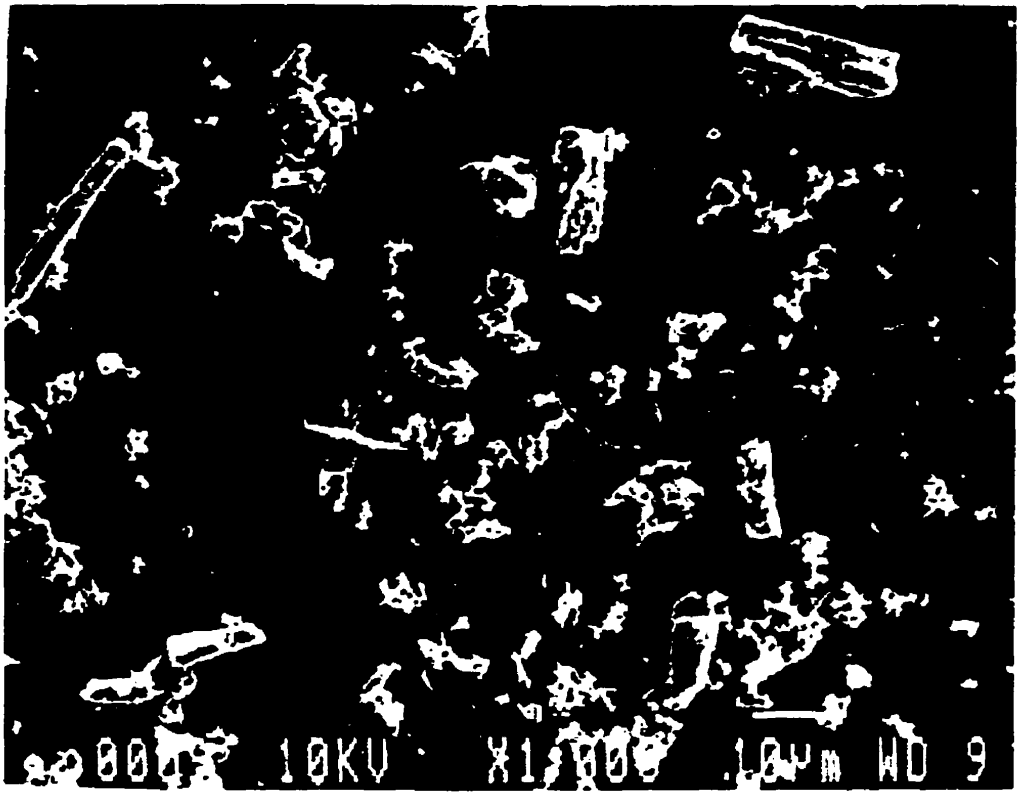

Figure 4-3. SEM micrograph of wollastonite powder after 10 minutes processing in the shatterbox mill.

Particle size analysis of the shatterbox-processed wollastonite is contrasted to the alumina powder and the raw wollastonite in Figure 4-4. The reduced size and aspect ratio of the wollastonite was expected to create more favorable co-dispersion conditions with the submicron alumina powder. Conversely, the added surface area of the alkaline wollastonite was expected to make suspension pH control and stabilization more difficult.

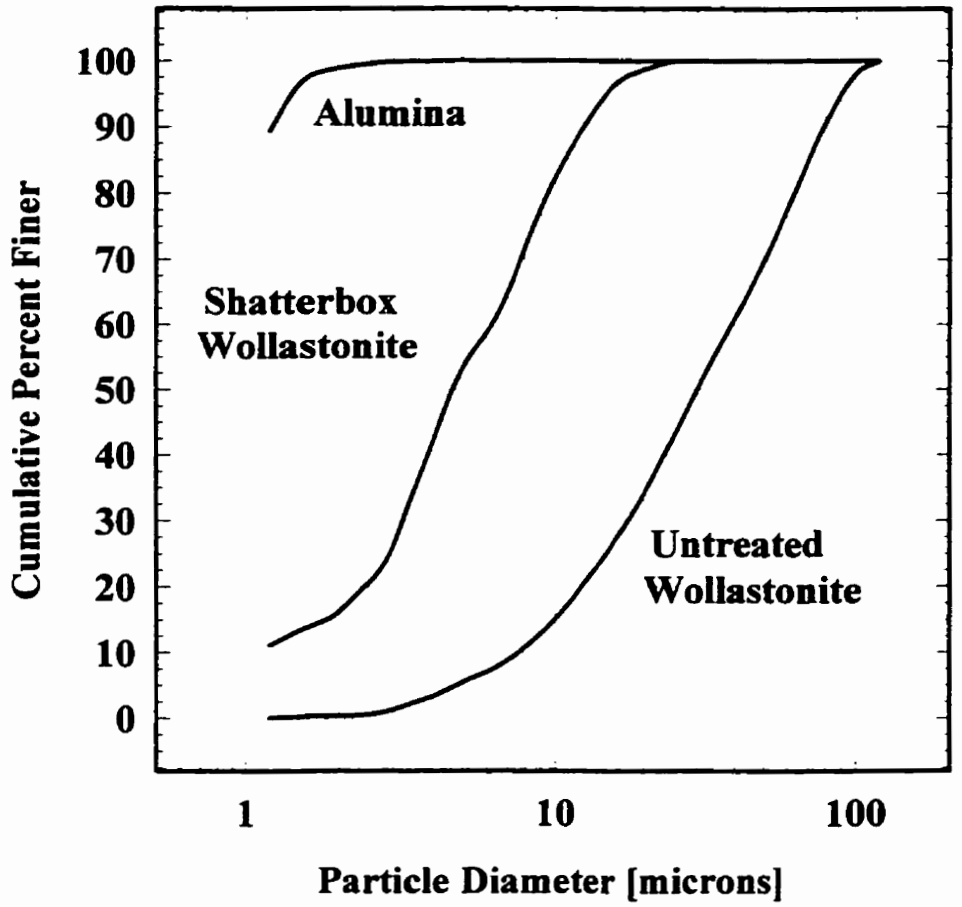

Figure 4-4. Particle size analysis showing the effects of ten minutes of shatterbox treatment on the wollastonite. The mean particle size decreases from ~30 μm to 4.5 μm.

4.2 Rheological Testing

Sedimentation of a 5 vol% alumina suspension was shown to have optimum dispersion characteristics over an acidic pH range of 2.0 to 6.0 (Figure 4-5). Near the known isoelectric point of the alumina powder (pH ≈ 8.0) [127], flocculation produced a very high and loose sediment. Above this pH the dispersion improves but due to the large amount of ammonium hydroxide required, dispersion effectiveness was limited due to the high ion concentration of the water which compresses the double layer at the powder surface. This effect is shown by the height of the sediment in alkaline conditions which does not come close to that of the acidic range which produced little or no sediment.

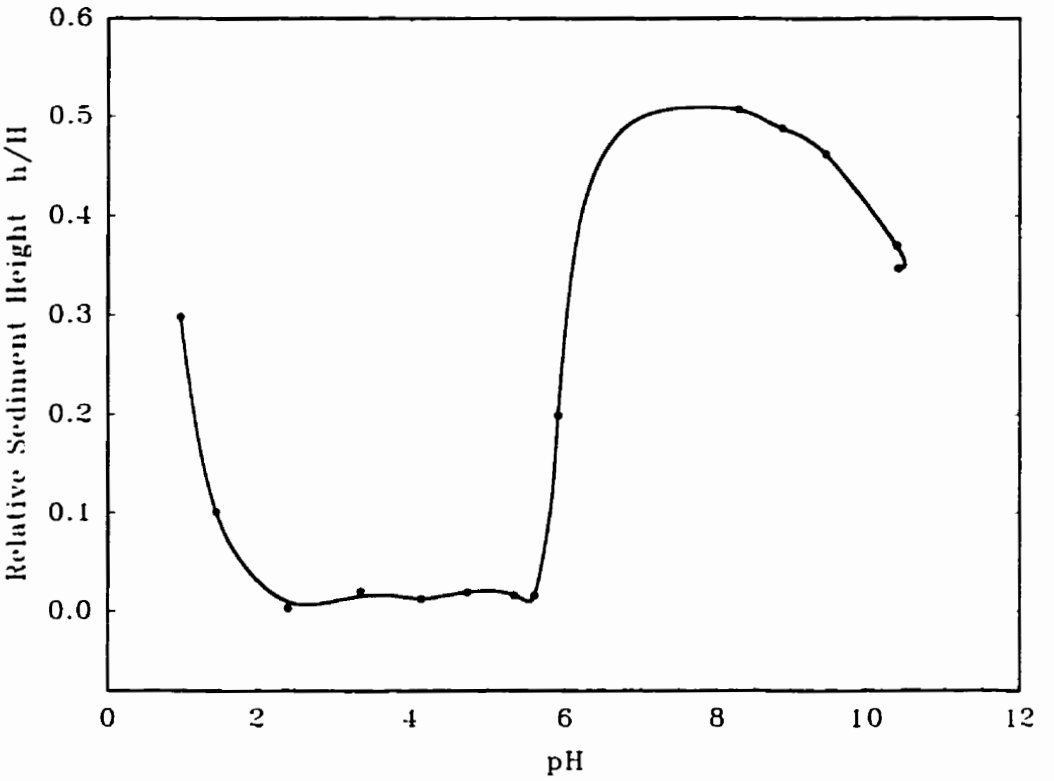

Figure 4-5. Relative sedimentation height of 5 volume % alumina in water depending on pH. Sedimentation times were 20 hours.

Furthermore, previous work [128] had shown that alkaline alumina - wollastonite dispersions had much higher apparent viscosity than acidic range suspensions. In that study, viscosity testing of aqueous alumina suspensions ($\Phi_s = 0.20$) showed that optimum dispersion was between pH 2.0 and 6.0 (Figure 4-6). For these reasons, the acidic pH range was chosen for study.

Alumina, which was used as the control material for this thesis, was prepared as described in §3.2.1(a), and slip cast samples achieved a green density of 2.58 g/cc. A study of anionic and cationic dispersants resulted in an optimized green density of 2.74 g/cc (69 % TD) using 1500 ppm of BETZ 1190 (cationic polyelectrolyte).

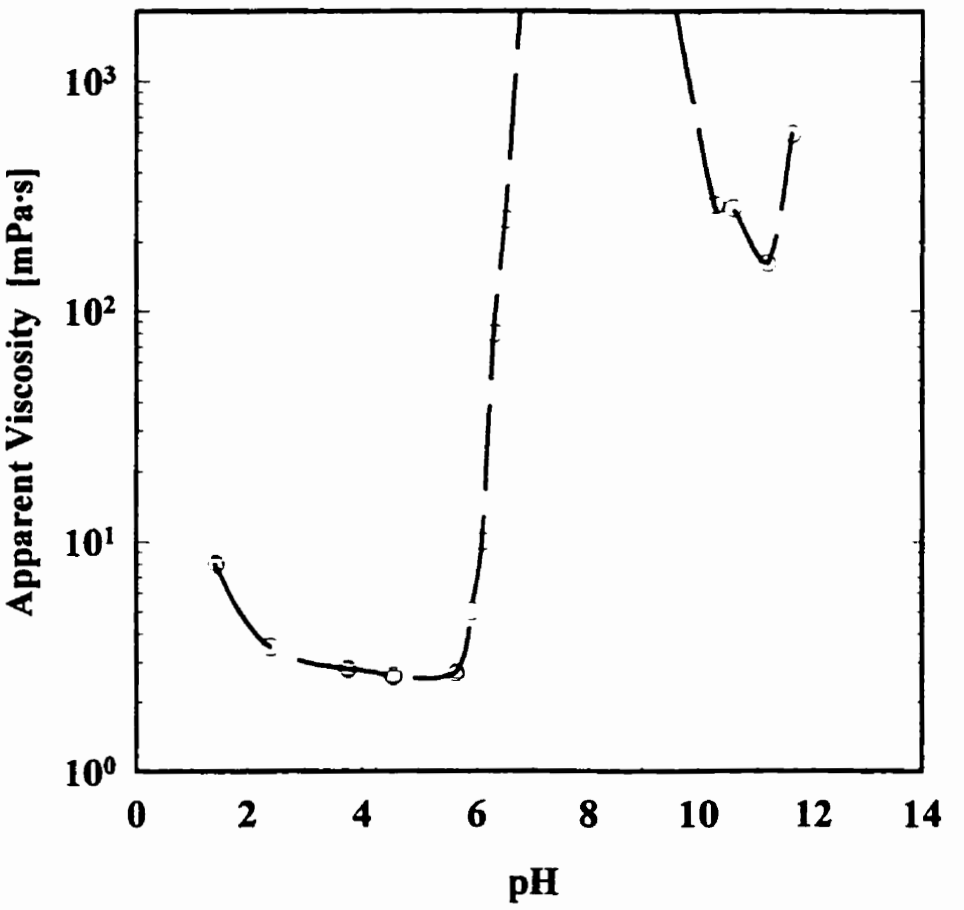

Figure 4-6. Apparent viscosity as a function of pH for alumina suspensions prepared at $\Phi_s = 0.20$ using a shear rate of 79 s^{-1}.

A brief rheological study of a composite suspension containing a lower concentration of wollastonite (90 vol% alumina - 10 vol% wollastonite ≡ 92.5 wt% alumina - 7.5 wt% wollastonite) showed that optimum composite suspension pH shifted to below 3.0 (Figure 4-7). It was observed that the system was stable at this pH for a limited amount of time due to the alkalinity of the reactive wollastonite surface, so it was decided that an organic dispersant was required to improve dispersion conditions.

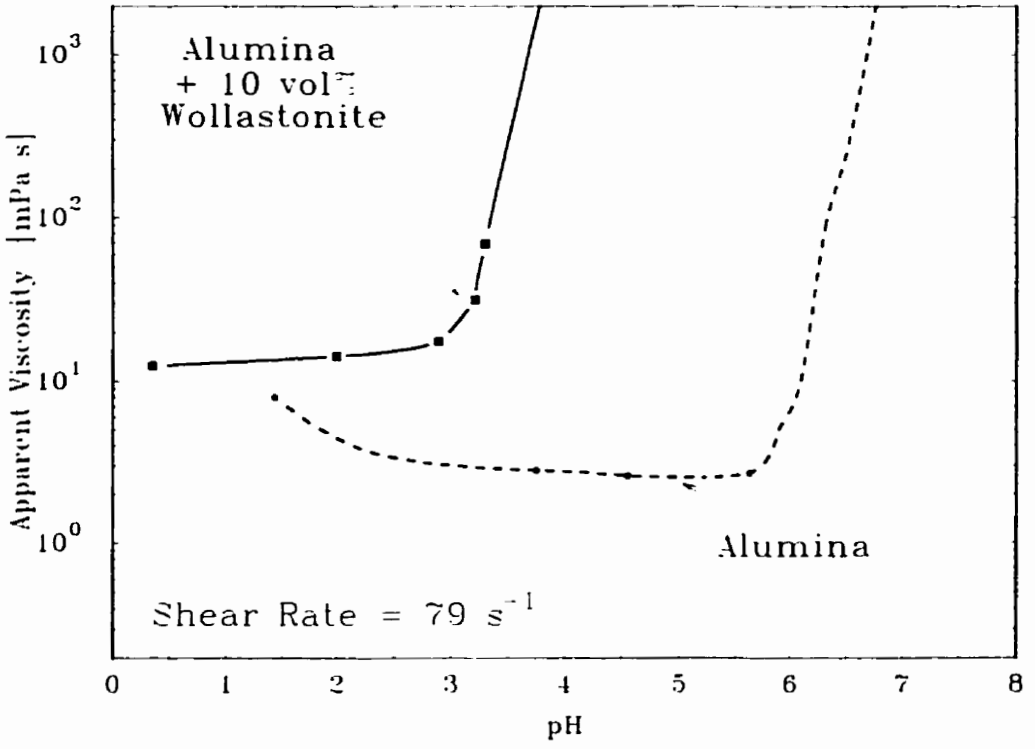

Figure 4-7. Effect of pH on apparent viscosity of alumina ($\Phi_s = 0.20$) and alumina + 10 vol% wollastonite ($\Phi_s = 0.25$) measured at shear rate = 79 s^{-1}.

Initially, several anionic dispersants (Darvan C, Darvan 821A, Dolapix PC-75, and Emphos CS361) were investigated and it was found that best viscosity and slip cast density results were obtained with Darvan C at a concentration of 30 ppm (Figure 4-8).

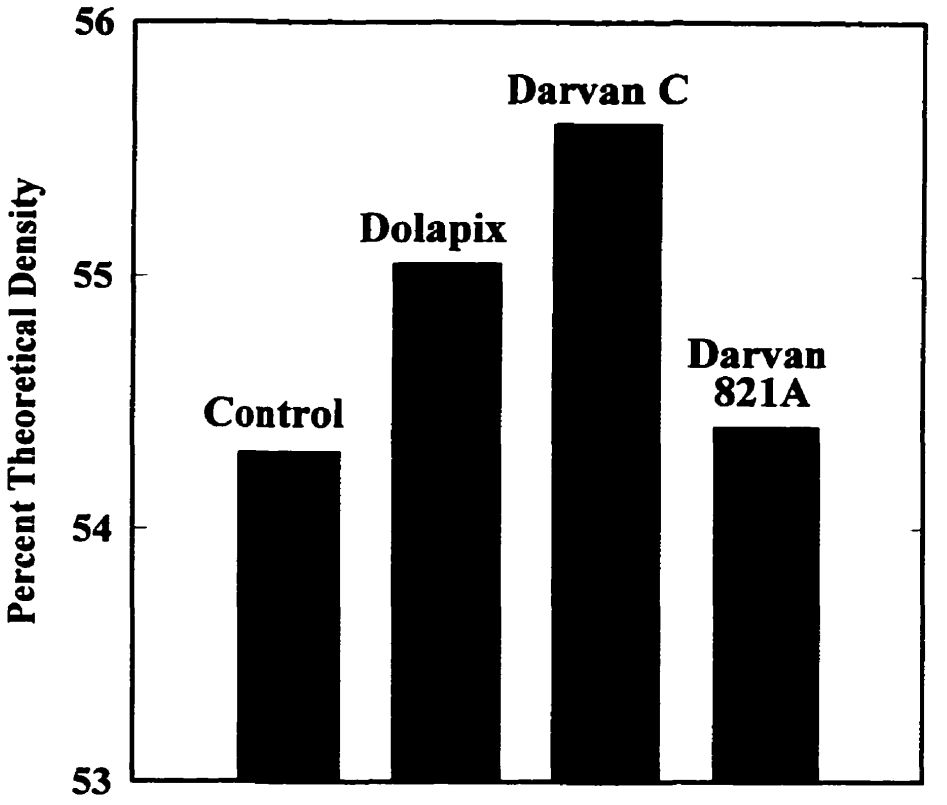

Figure 4-8. Best slip cast densities obtained for alumina + 10 vol% wollastonite using anionic dispersants (Emphos CS361 did not homogenize well enough to be effective).

Recent work by Premachandran *et al.* [122] suggested that a cationic polyelectrolyte, BETZ 1190, would be a more appropriate choice in composite aqueous suspensions, especially when the solids have opposing pH dispersion behavior (due to differing isoelectric pH). They reported that the cationic polyelectrolyte (CPE) shifted the

isoelectric points of each constituent enough to ensure appropriate dispersion conditions. However, acidic suspension conditions were necessary to activate the ionic polymer chains to make the system well-dispersed (Figure 4-9).

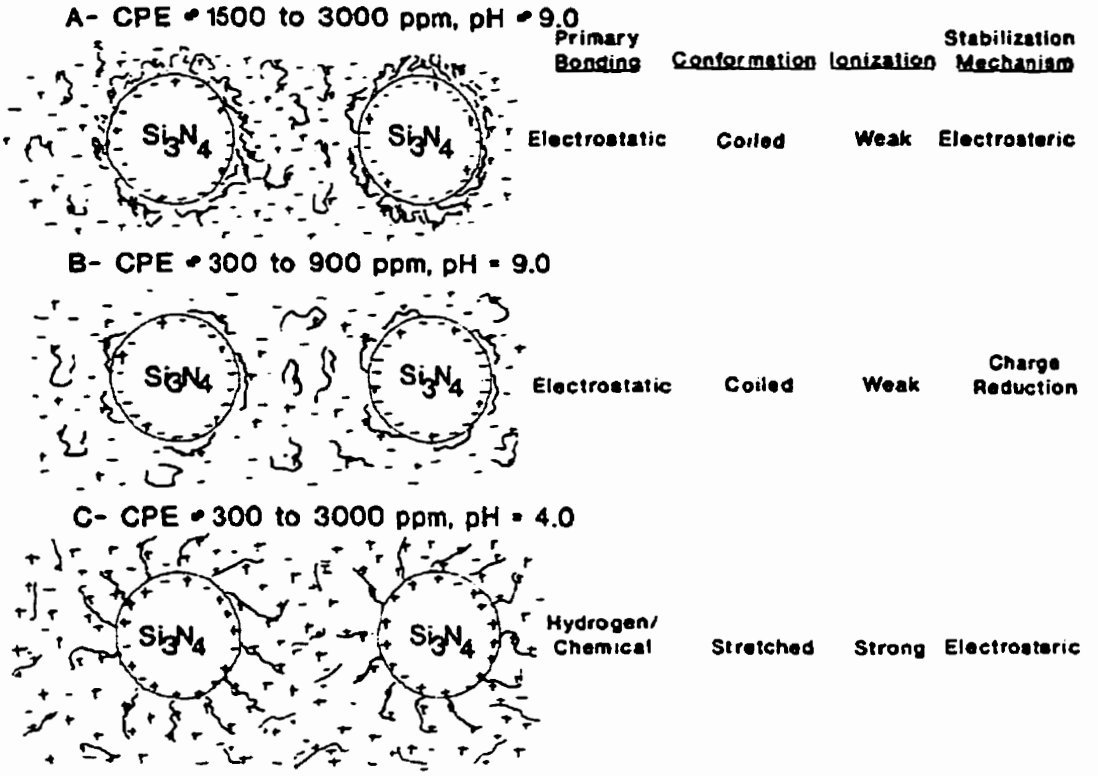

Figure 4-9. Diagram representing the surface action of cationic polyelectrolytes interacting with suspended Si_3N_4 particles at varying CPE concentration and pH.[121]

Initial results showed that a significant improvement in the suspension viscosity was evident when high concentrations of the CPE (3000 ppm) were added.

It was found that the alkalinity of the wollastonite was still managing to shift the system pH high enough to cause flocculation of the CPE treated system. When the pH drifted above 3.0, the polymer chains lost their electrostatic effect and the compressed double layer (due to the high ionic concentration) resulted in a system with limited stability.

It was concluded that only limited amounts of nitric acid should be employed during processing to maintain low ionic concentration. Only just before degassing of the suspension is the acid added to control final casting pH. After 2-3 minutes of degassing, the suspension is poured into the plaster mould and allowed to consolidate for up to 10 minutes. Enough slurry is kept aside to monitor the pH, in order to ensure the suspension remains below pH 3.0.

Figure 4-10 shows the apparent viscosity as a function of CPE concentration at an optimized pH of 2.3 and at a pH of 4.7. These curves show that the optimum concentration of CPE is 1500 ppm. Clearly, the pH and ion concentration are critical in controlling the effectiveness of the polyelectrolyte. This fact is demonstrated by the diagram produced by Malghan et al [121] which is reproduced in Figure 4-9. As the pH reaches a critical level, the ends of the polymer chains become activated and spread out into the solution, which produces a good dispersion. If pH levels become too high, the steric and electrostatic repulsive forces are not effective in separating individual particles.

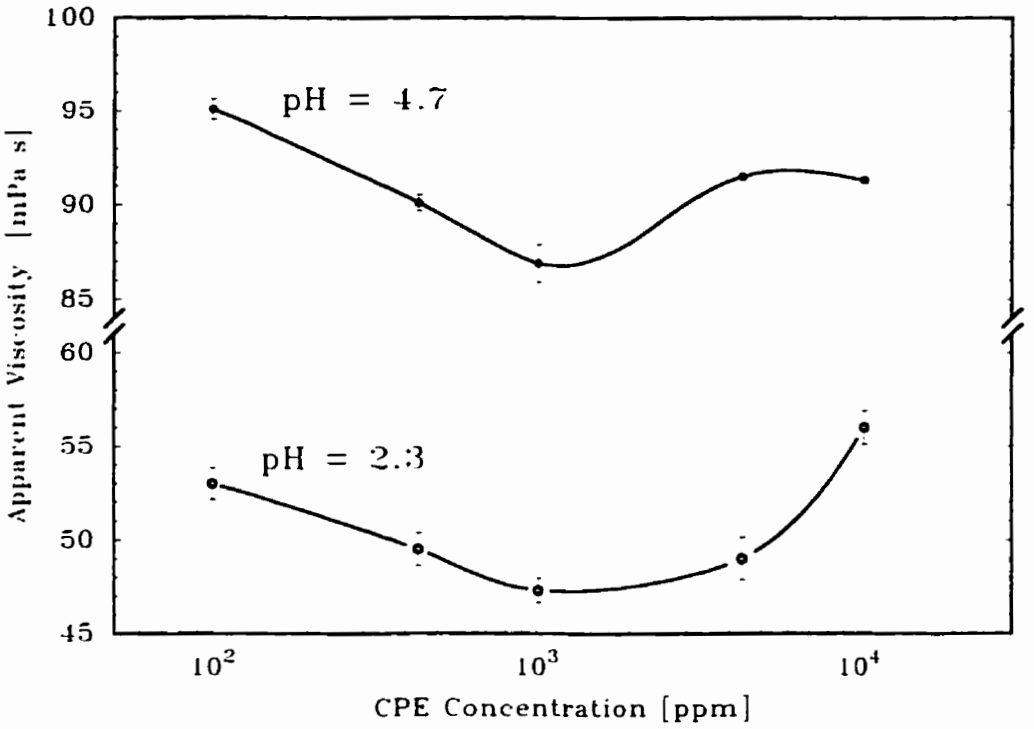

Figure 4-10. Apparent viscosity as a function of cationic polyelectrolyte concentration for alumina - 20 vol% wollastonite suspensions at pH = 2.3 and 4.7 (Φ_s = 0.34).

When the optimized conditions were incorporated to produce composite green bodies through slip casting, it was found that for various fractions of wollastonite present (0-20 vol%), the CPE dispersant was more effective than the best APE dispersant (Darvan C). This is shown in Figure 4-11 which plots the green density for various compositions using either a cationic or anionic polyelectrolyte. Clearly, the best results were obtained using the BETZ 1190 polymer to aid in dispersing the particle suspension.

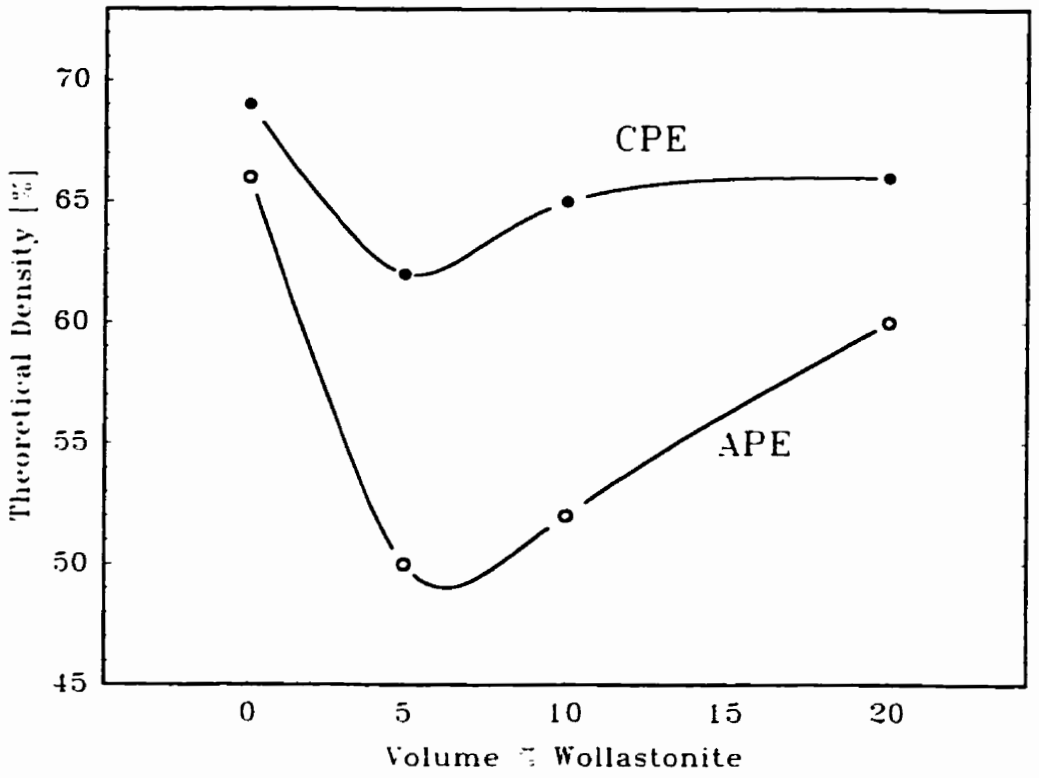

Figure 4-11. Green density as a function of amount of wollastonite in the composite suspension when using a cationic (CPE) or anionic (APE) dispersants.

4.3 Thermal Analysis

4.3.1 Thermodynamic Considerations (F*A*C*T)

Thermodynamic calculations complimented by the ternary phase diagram help to predict the compounds present after sintering. By setting the reaction conditions and compositions, the F*A*C*T software can calculate the compounds and phases present at a given temperature and pressure.

Analysis which considers the amount of wollastonite present in the green body allows computation of equilibrium conditions at prescribed temperatures and pressures. Using one atmosphere of pressure for all computations (simulating sintering in air) and reacting with excess oxygen, the half-reaction is set up as follows:

$$<80>Al_2O_3 + <20>CaSiO_3 + <100>O_2$$

The number in carats represents the mass of the component involved in the reaction. Each model showed no reaction between the oxygen and the condensed matter. As well, although both the phase diagram and the F*A*C*T analysis showed the formation of hibonite, none was found after quenching or devitrification (§4.4.2) of the CAS ceramic; this is likely due to slow nucleation kinetics. As a result, this phase was eliminated from the list of possible products during the thermodynamic computations.

By varying the mass ratio of alumina to wollastonite, a plot of amount of liquid present (assuming CAS liquid density ≅ 2.6 g/cc [51]) at the proposed sintering temperature of 1500 C can be produced (Figure 4-12). This gives an indication of the limited amount of

wollastonite that can be reacted while maintaining structural shape of the green body (limit is 25 vol% liquid for isometric grains [27], limiting wollastonite content to under 10 wt%). However, preliminary studies found that structural integrity was maintained up to 20 wt% wollastonite. The reasons for the discrepancy may be due to slow reaction kinetics (of liquid formation), and the development of non-isometric alumina grains which increases the rigidity of the body. This phenomenon has been shown by other authors [16-23] and was also observed in this study (§4.4.3).

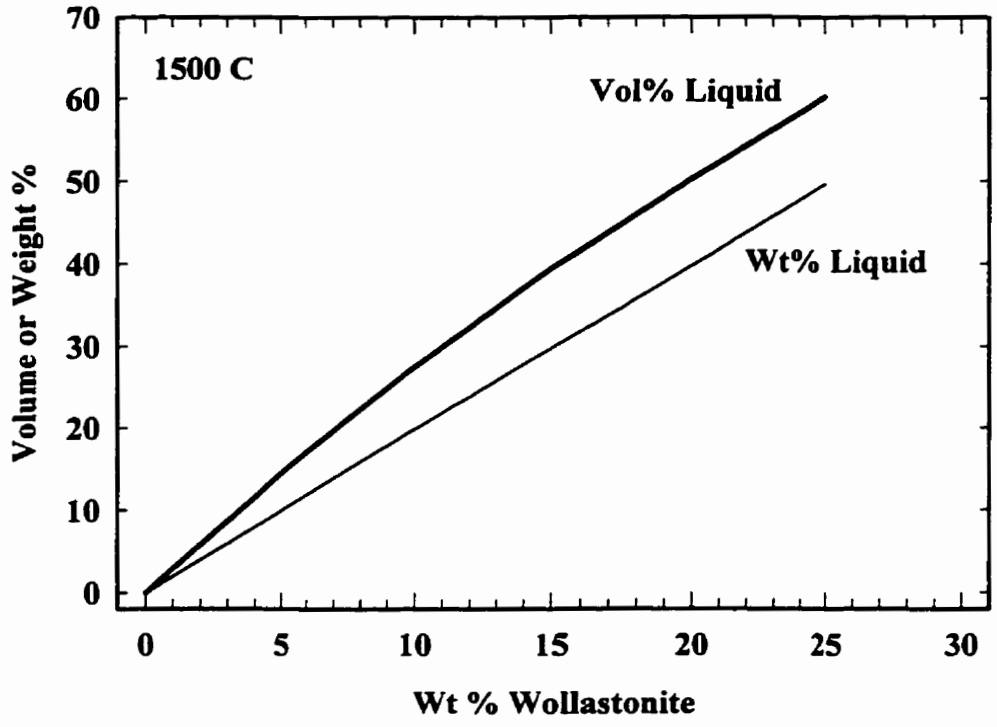

Figure 4-12. Amount of liquid present at 1500 C as a function of the amount of wollastonite present in the green body (assuming CAS liquid density ≅ 2.6 g/cc [51]) according to F*A*C*T thermodynamic calculations.

This thermodynamic analysis can also be used to determine the amount of liquid present just before full crystallisation would be expected (at just over 1400 C according to the phase diagram and the F*A*C*T program). The results are shown in Figure 4-13. For a 100 gram CAS sample with 20 wt% wollastonite there should be 32 grams of liquid and 68 grams of solid (alumina and anorthite) present. It is anticipated that the fast cooling will prohibit the formation of anorthite and gehlenite and, as a result, only crystalline alumina is expected along with a significant amount of glass containing all the CaO and SiO_2 and some proportion of alumina. According to the F*A*C*T results at 20 wt% wollastonite, the liquid contains 47 wt% alumina just before full solidification, the remainder consisting of roughly equal amounts of the CaO and SiO_2 constituents.

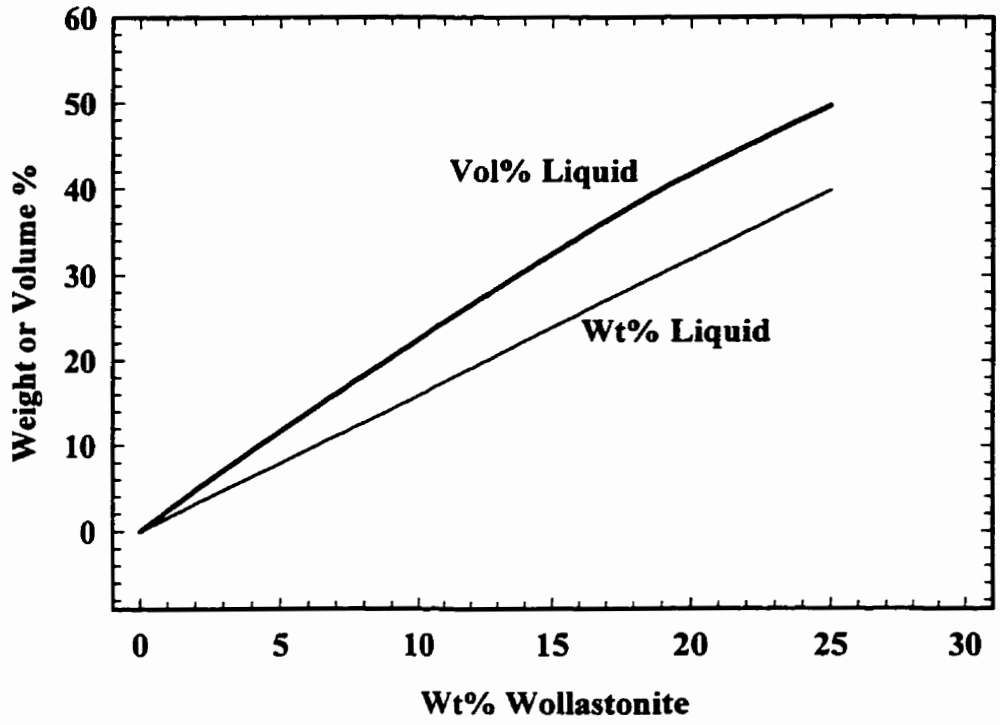

Figure 4-13. Amount of CAS liquid present before complete solidification (≈1402 C) according to F*A*C*T thermodynamic calculations (assuming CAS liquid density ≅2.6).

By varying the equilibrium temperature, an isoplethal study can be constructed for the system. The results of this analysis is shown in Figure 4-14. When hibonite is eliminated from consideration, only alumina, anorthite and gehlenite are expected to form under equilibrium conditions. This agrees with the XRD observations (§ 4.4.2).

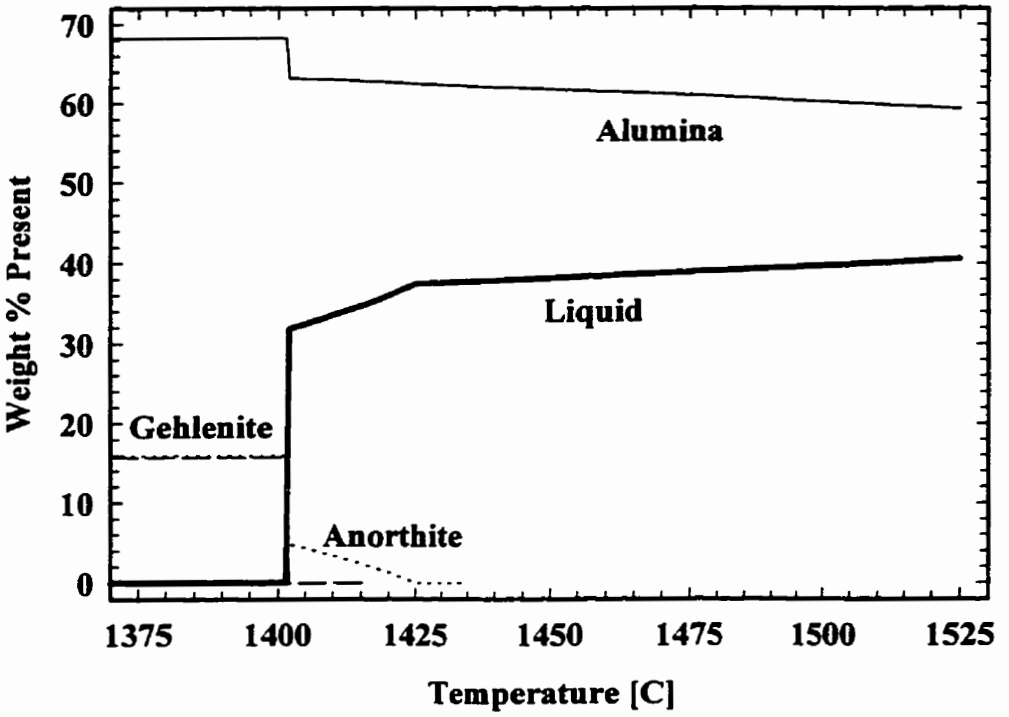

Figure 4-14. Isoplethal study of the alumina + 20 wt% wollasonite composition produced using F*A*C*T calculations showing the expected formation of gehlenite and anorthite (when hibonite is removed from consideration).

4.3.2 Thermogravimetry

By measuring the mass of the CAS sample as a function of temperature, anticipated reactions can be observed. The plot of mass as a function of temperature (Figure 4-15) shows a general decreasing trend as temperature increases. Minor fluctuations in this trend are observed between 1100 C and 1300 C, as can be seen in the plot showing the derivative of the TGA data (dM/dT). At about 1400 C, a decrease in the sample mass and

the dM/dt is apparent. This indicates volatisation of the liquid phase formed at that temperature.

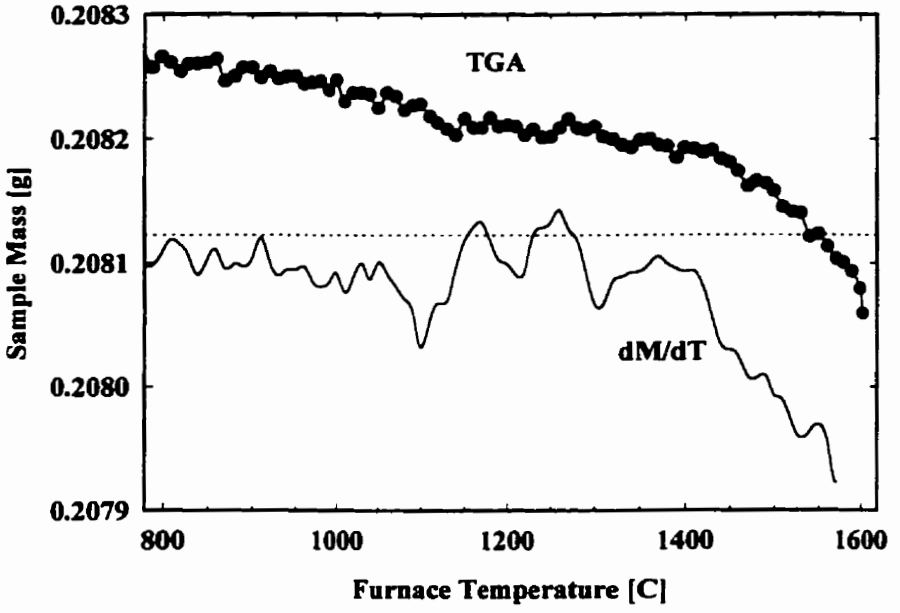

Figure 4-15. Thermogravimetric plot showing sample mass, and change in mass as a function of temperature (the dotted line represents the baseline, constant mass for the change in mass plot).

4.3.3 Differential Thermal Analysis

Differential thermal analysis (DTA) is a useful tool in ceramic materials processing in that reactions which take place under sintering conditions can be investigated to determine the precise reaction temperature, whether it be exothermic or endothermic. Further, as part of this thesis, a technique has been developed to find nucleation temperature of a glass using DTA, which is applicable to the crystallisation of the glass phase formed during the liquid phase sintering stage.

The first aim in the development of the technique is to perform a simple DTA scan on a green sample of a slip cast alumina-wollastonite mixture. The resulting scan is shown in Figure 4-16. Note that no significant peaks are found below 1000 C. At 1100 C exothermic + endothermic peaks corresponding to transformation of wollastonite to pseudo-wollastonite [12, also F*A*C*T thermodynamic database] is found. At 1250 C a double peak (endothermic) commences. This may be due to reaction of the wollastonite with the alumina matrix and formation of an intermediate phase before full dissolution occurs. At 1370 C the final reaction occurs, which is the formation of a liquid phase which dissolves some of the alumina and all of the CaO and SiO_2. This fact is confirmed by XRD analysis of the CAS which was reacted at 1500 C and air-quenched (Figure 4-25, §4.4.2), which shows only the existence of crystalline α-alumina. As well, SEM and EDS examination of the same material shows only alumina grains and a glassy material having a composition of approximately 39 % Al_2O_3 - 29 % SiO_2 - 32 % CaO (§4.4.1).

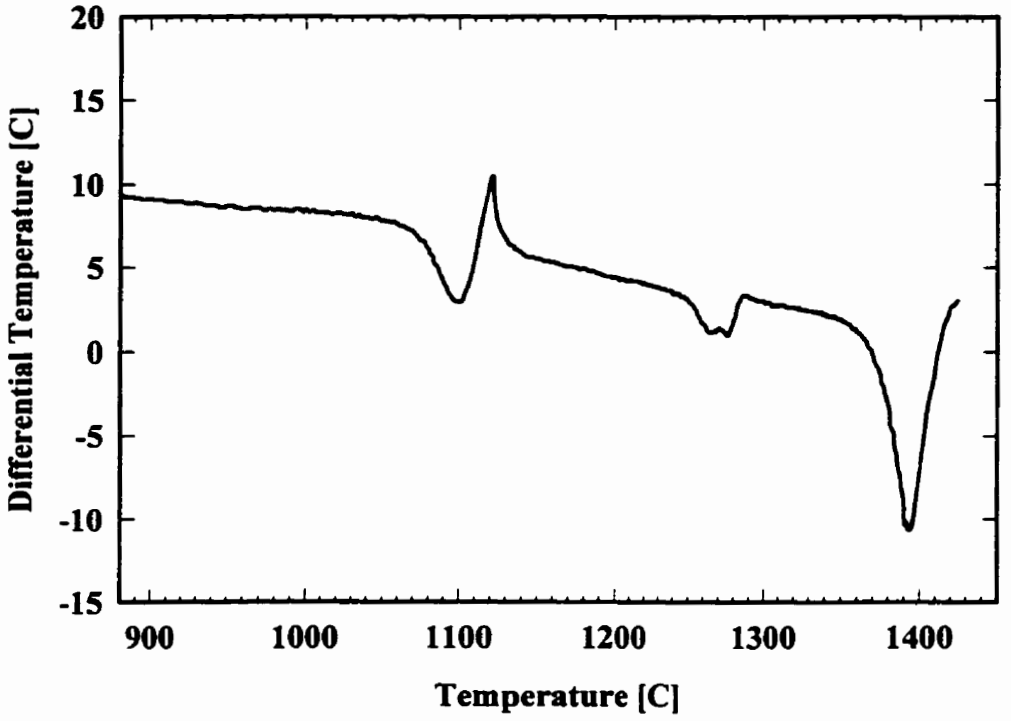

Figure 4-16. DTA scan of an alumina + 20 wt% wollastonite green body using a 10 K/min ramp rate.

After air-quenching, the glass can be crystallised by employing a heat treatment. Thus, a DTA scan of the heat treated CAS glass-ceramic shows a new exothermic peak occurring around 1280 C, which would correspond to formation of new crystalline compounds from within the glass. Previous research on lithium disilicate glass showed that a nucleation heat treatment before crystallisation aided in formation of the crystals. Thus, as noted by Kingery [24], a temperature exists at which homogeneous formation of nuclei within the glass is optimised.

When the heat treatment temperature approaches the optimum for homogenous nucleation, three effects can be observed in the exothermic crystallisation peak of the subsequent DTA scan. First, a growth of the magnitude of the peak can be expected. Second, a shift of the occurrence of the peak toward lower temperatures, and finally, the peak becomes somewhat sharper. All three changes are shown schematically in Figure 4-17. By noting each change individually, when compared to a standard, non-nucleated sample, the optimum nucleation temperature can be found.

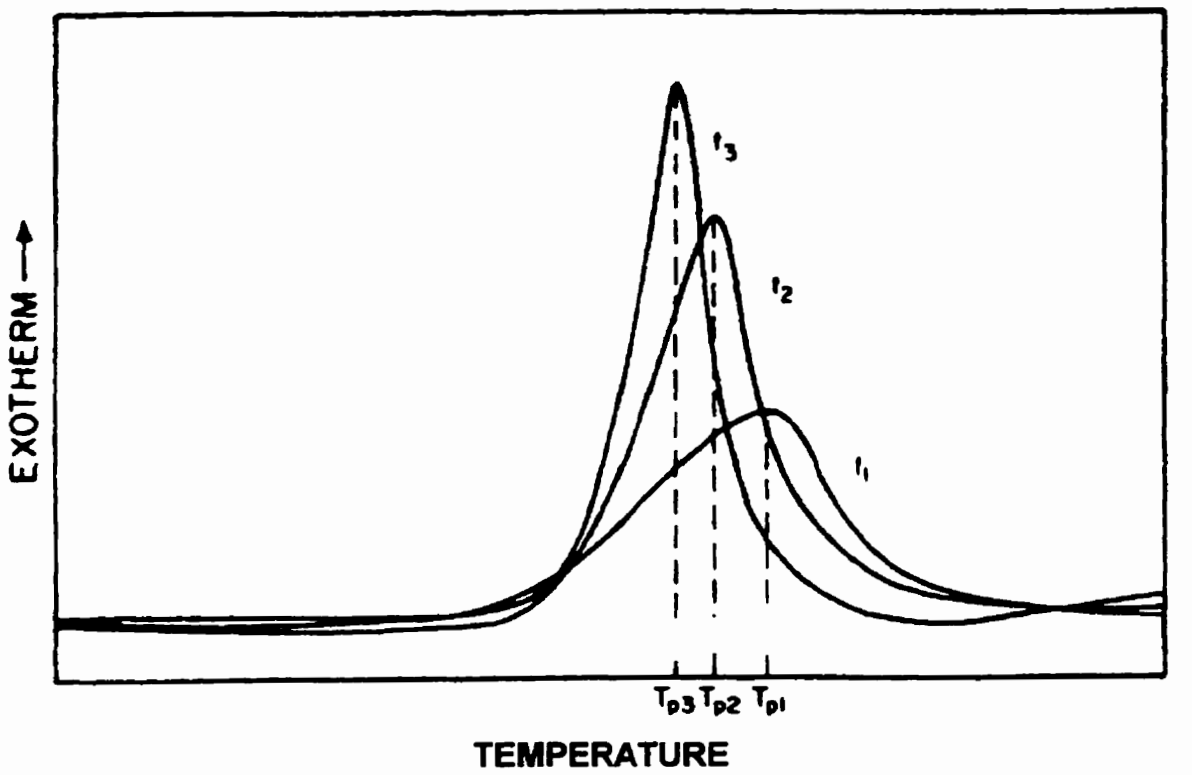

Figure 4-17. Effect of nuclei concentration on DTA crystallisation peak shape.[76]

Samples were tested with nucleation treatment at the specified temperature for two hours directly after RLPS and air-quenching. Once the nucleation stage is complete, the sample is heated at a high, constant rate (24 $K \cdot min^{-1}$ = 0.41 $K \cdot s^{-1}$) and the temperature difference with respect to the alumina reference is recorded as a function of sample temperature. The DTA scan of the sample used as a control for this experiment (no nucleation treatment) is shown in Figure 4-18. When subsequent runs were performed on nucleated samples, noticeable changes in the crystallisation peaks were found.

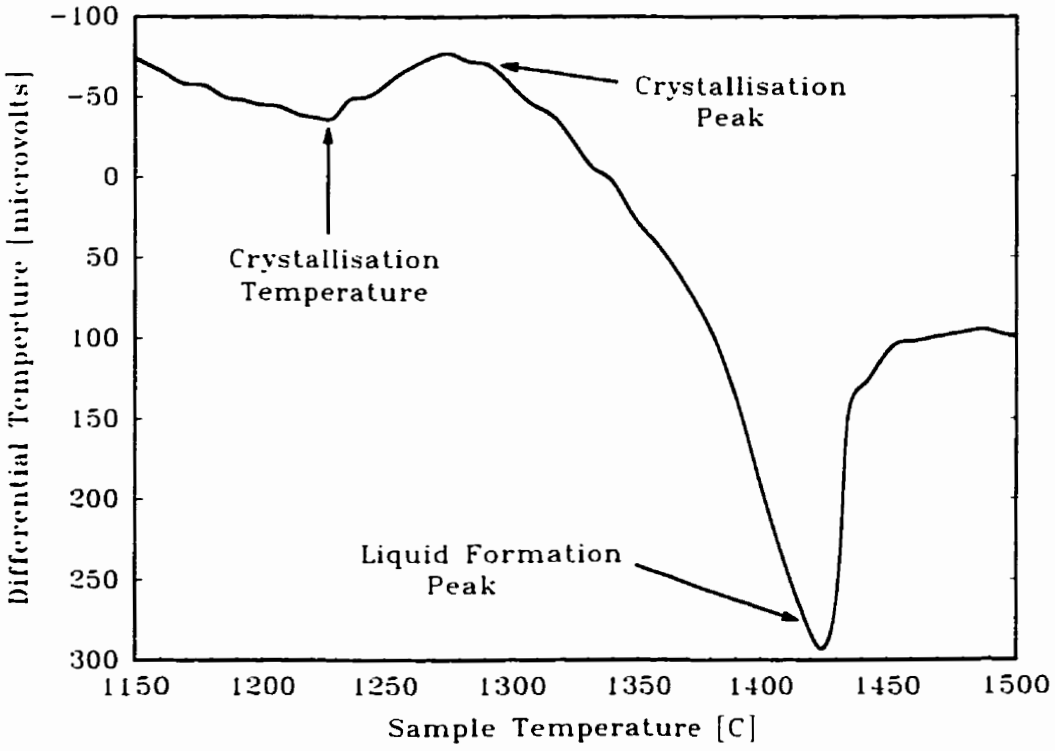

Figure 4-18. DTA scan (0.41 K/s ramp rate) of a quenched CAS ceramic showing the exothermic crystallisation peak and the endothermic peak which indicates formation of a liquid phase.

Figure 4-19 shows how the height of the crystallisation peaks changed as a function of the preceding nucleation temperature. Clearly, a maximum peak height is shown at a nucleation treatment temperature of 1032 C. This is the first indication of a prime nucleation temperature.

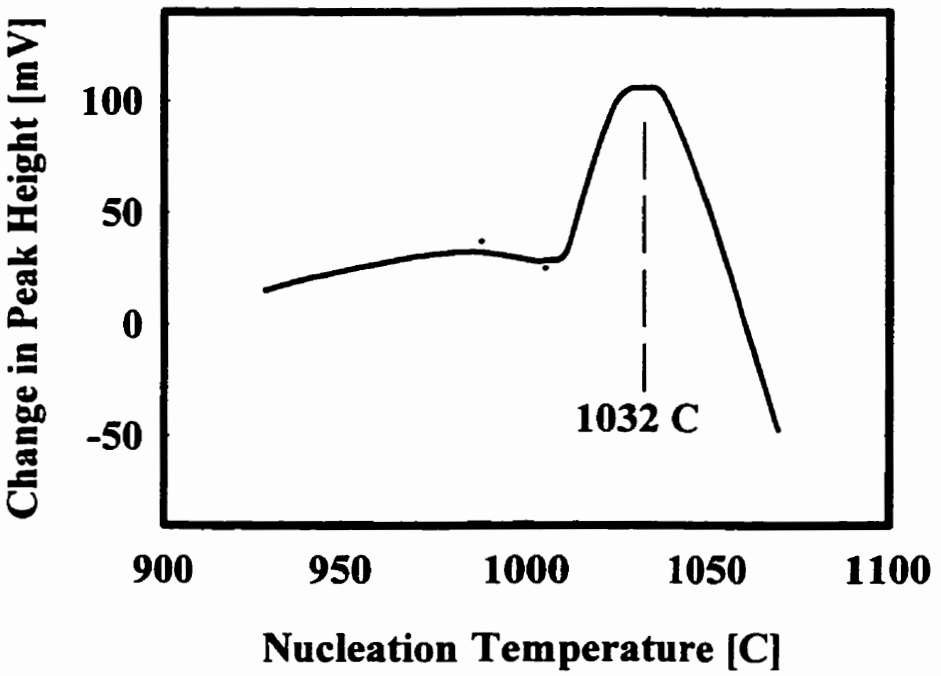

Figure 4-19. Change in crystallisation peak height as a function of nucleation treatment temperature for DTA scans on the quenched CAS glass-ceramic.

By plotting the temperature at which the onset of crystallisation is found with respect to nucleation treatment temperature, Figure 4-20, a maximum at 1032 C is again observed which is further testimony to the finding mentioned above.

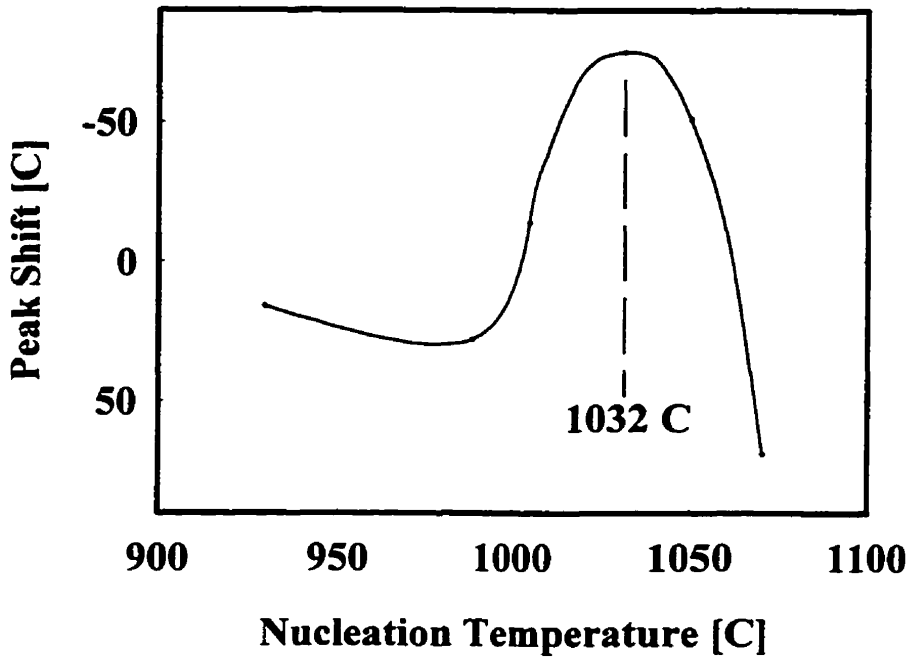

Figure 4-20. Plot of crystallisation peak shift as a function of nucleation treatment temperature for DTA scans of the quenched CAS glass-ceramic.

Thirdly, when a plot of change of peak breadth (full-peak width at half of the observed magnitude, FWHM) as a function of nucleation temperature is made (Figure 4-21), the treatment at 1032 C shows the narrowest peak, again confirming that it is very close to the optimum nucleation temperature. All three analysis methods confirm that the two hours heat treatment at 1032 C produced the best nucleation conditions.

Another graphical method has been suggested [78] by which all three variables are combined to give full and dramatic evidence of the best nucleation treatment. This is done by simply plotting the area under the crystallisation peak as a function of sample temperature during the DTA experiments.

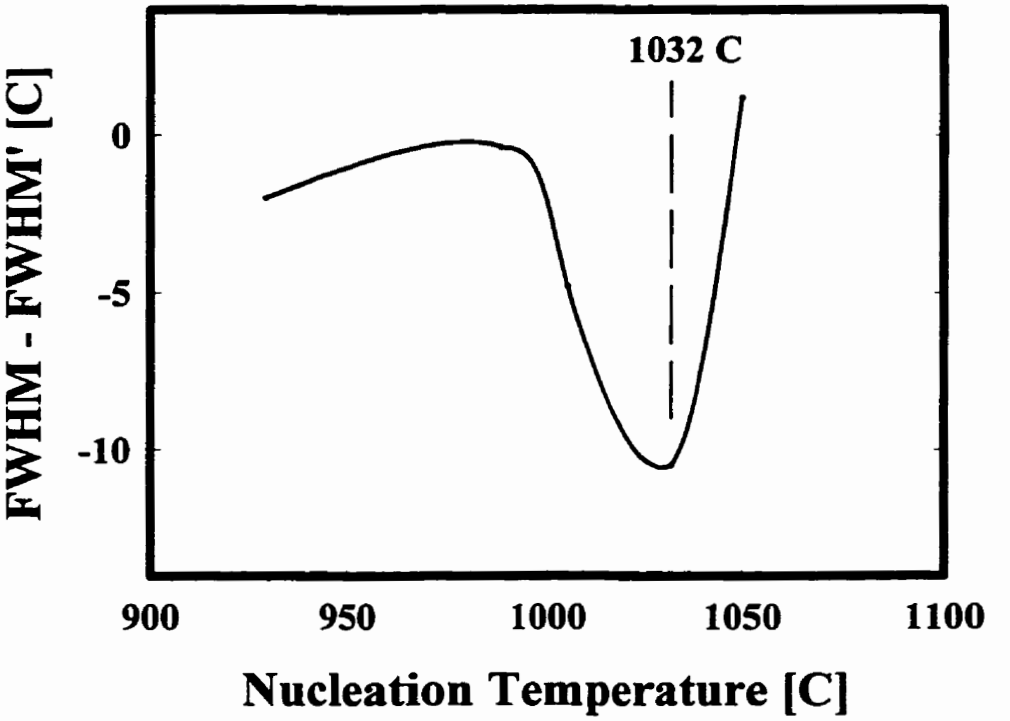

Figure 4-21. Plot of change in crystallisation peak breadth (FWHM = full width at half maximum) when compared with breadth of crystallisation peak of a non-nucleated sample (FWHM') as a function of nucleation treatment temperature using DTA scans of the quenched CAS glass-ceramic.

A simple program was adapted to compute peak area according to temperature (Appendix A). When plotted (Figure 4-22) the results show (1) differences in peak magnitude (total

area instead of peak height), (2) shift of initiation of peak to lower temperatures, and (3) the slopes of the curves indicate the sharpness of the peaks (sharp peaks have steep slopes; broad peaks have gradual slopes). Again, the nucleation treatment at 1032 C shows the most dramatic improvement in crystallisation. Of the methods described, this is the most effective technique to justify the choice of nucleation temperature.

Other work using similar techniques [74,75] reported that most of the nuclei grow within the first 120 minutes and that longer times have less and less effect on the appearance of new nuclei (following a square-root growth relation). Thus, it was decided that a nucleation treatment of four hours would be appropriate to maximize the nuclei population within the glass.

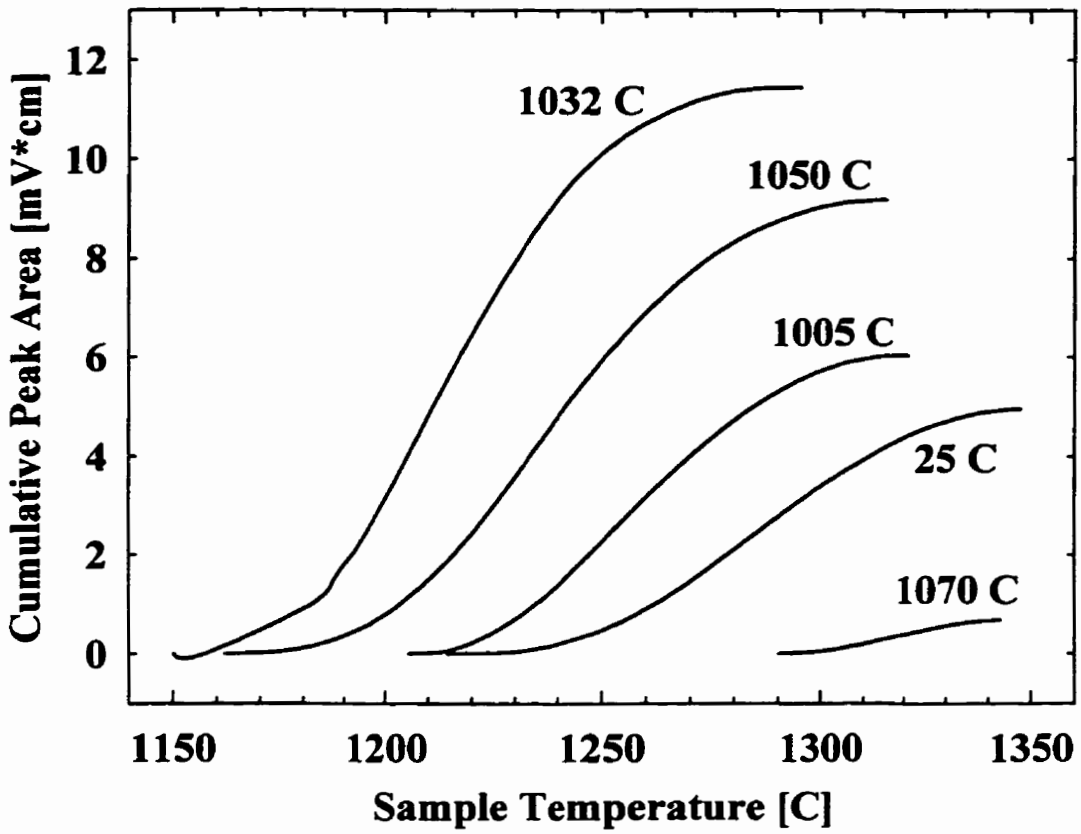

Figure 4-22. Graph of crystallisation peak areas versus actual sample temperature for various DTA scans of the quenched CAS glass-ceramic.

A DTA scan of a quenched CAS ceramic after employing the chosen nucleation treatment temperature of 1032 C is shown in Figure 4-23. Clearly, the crystallisation peak has shifted and grown compared to the non-nucleated quenched CAS material (Figure 4-16). Note also that the new crystallisation temperature is found to be 1180-1200 C. Using these findings, an optimised furnace schedule was prepared for the production of a CAS ceramic (Figure 4-24).

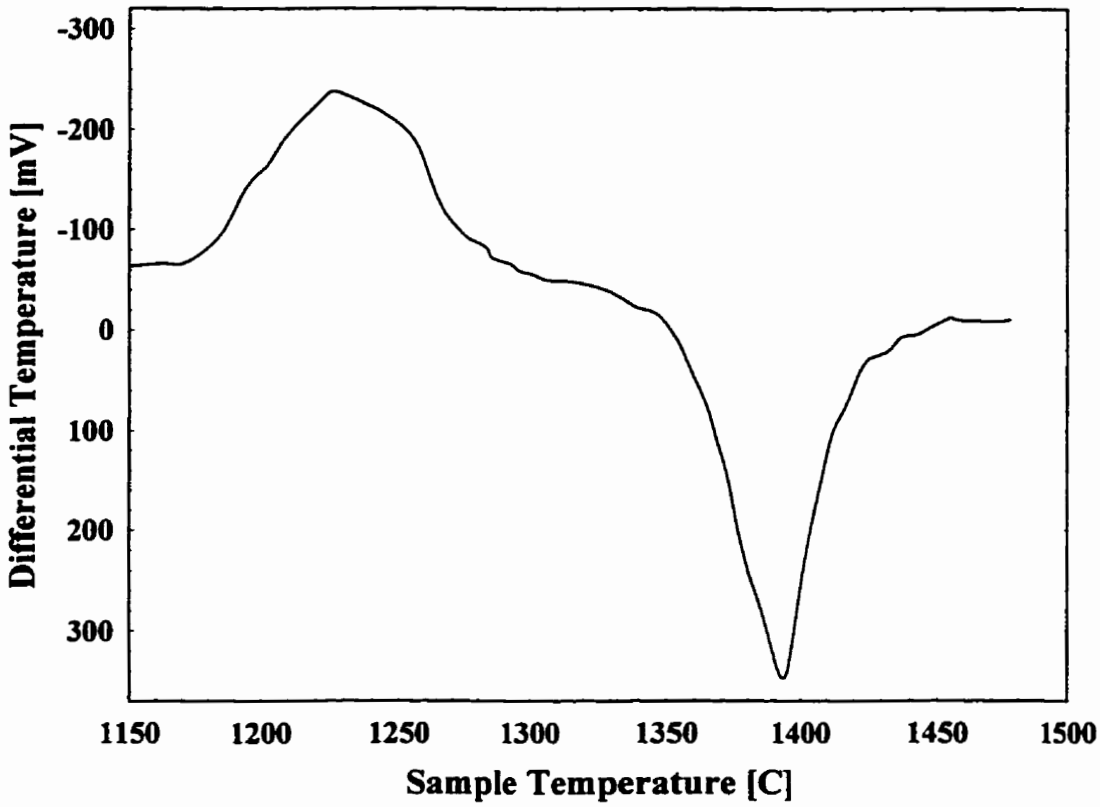

Figure 4-23. DTA scan of a quenched CAS ceramic sample after 4 hours of nucleation heat treatment at 1032 C.

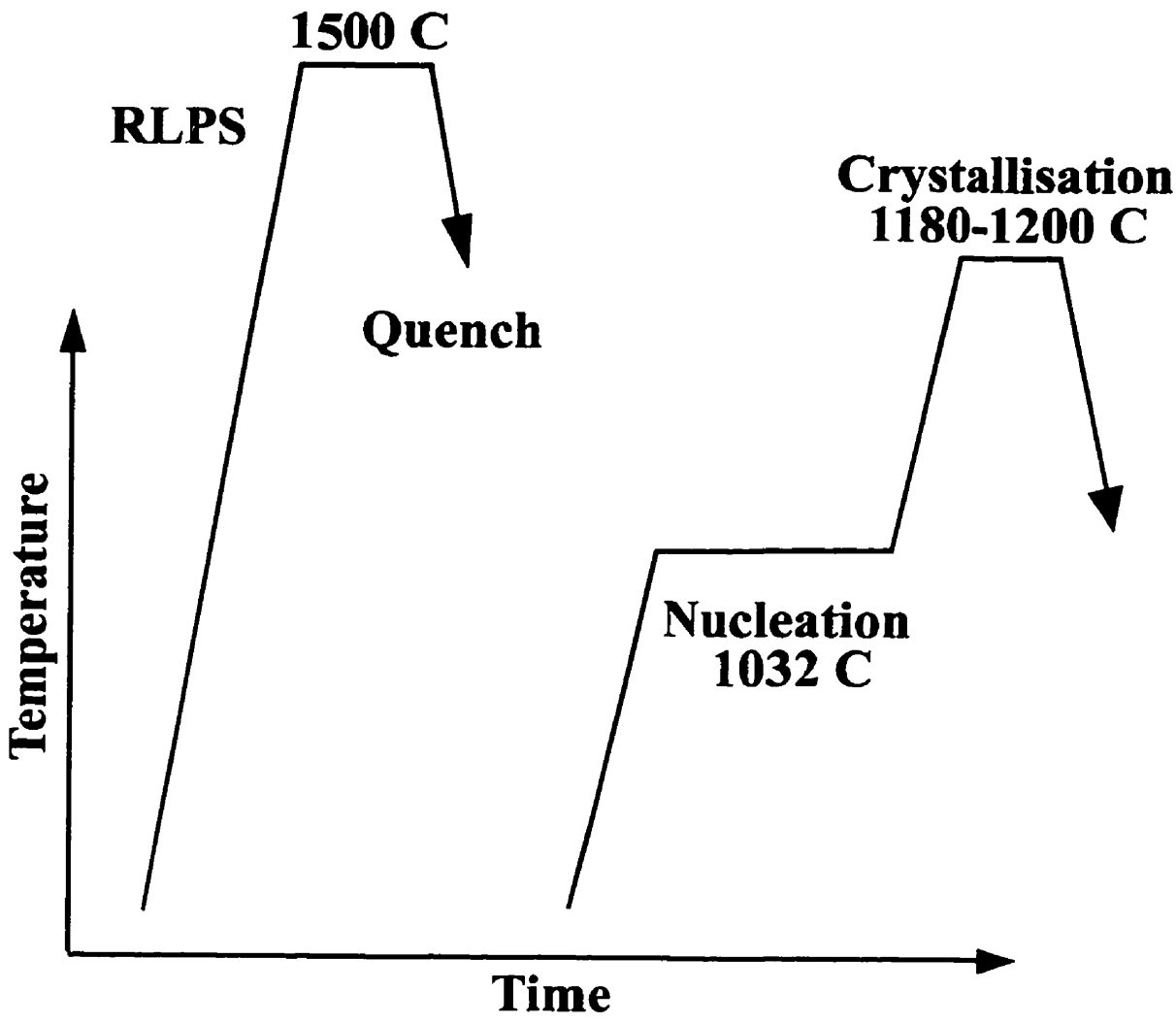

Figure 4-24. Optimised furnace schedule to produce a crystalline CAS ceramic.

4.4 Physical Characterization

4.4.1 Electron Probe Microanalysis (EPMA)

After liquid phase sintering and quenching, the samples were examined under the microprobe and only two distinct phases could be found. The first, which appeared slightly darker and with linear edges (suggesting a crystalline structure) was found to be 100% Al_2O_3, as anticipated. Between the alumina grains was a phase which did not have clear grain boundaries (suggesting a glass), and was characterized as having 39.1 wt% Al_2O_3 - 28.9 % CaO · 32.0 % SiO_2. This finding shows that less alumina was present in the liquid phase than was predicted using thermodynamics (about 48 wt% alumina). This means that the system did not reach chemical equilibrium during the LPS stage. However, this is not a detriment to the final results since longer LPS times would result in exaggerated grain growth and there is no advantage to establishing higher alumina concentrations in the glass.

After devitrification, alumina grains were again confirmed, and appeared unchanged after the secondary heat treatment. However, the glass phase had transformed into grains which were difficult to characterize due to their fine size and the porous nature of the devitrified microstructure. Compositional values did not correspond to any known compounds in the CAS system, and measurement results of anything but large alumina grains were impossible to repeat. Therefore, this characterization technique cannot distinguish the new crystalline compounds, and for this, XRD analysis is more appropriate, though quantitative results are not possible.

4.4.2 X-ray Diffraction

Qualitative analysis is reliably performed using X-ray diffraction. An indication of reaction products of all relevant samples is possible by performing this technique. The results are difficult to display in their entirety, so the plots in this section are bar charts which display the relative peak area and the beam angle at which they occur. As well, these peaks are labeled with the corresponding compound which was responsible for the appearance of the peak.

The green body diffraction results verified that only alumina and wollastonite were present. Diffraction of the quenched CAS sample indicate that the only crystalline product at that stage is alumina (Figure 4-25 (a)). Finally, Figure 4-25 (b) shows that after the devitrification treatment, diffraction peaks are found for alumina, gehlenite and anorthite. The relative sizes of the peaks tend to indicate that, as expected, alumina is the most prevalent compound; however, though relatively equal amounts of the ternary compounds were anticipated, it appeared that more gehlenite was present than anorthite, although this type of quantitative finding is difficult to justify.

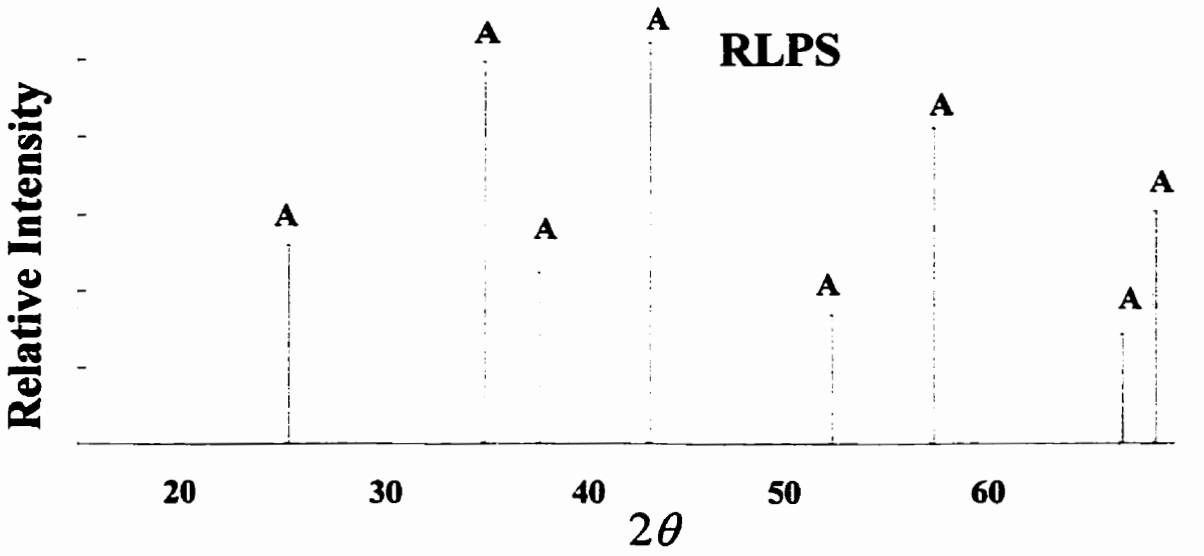

(a)

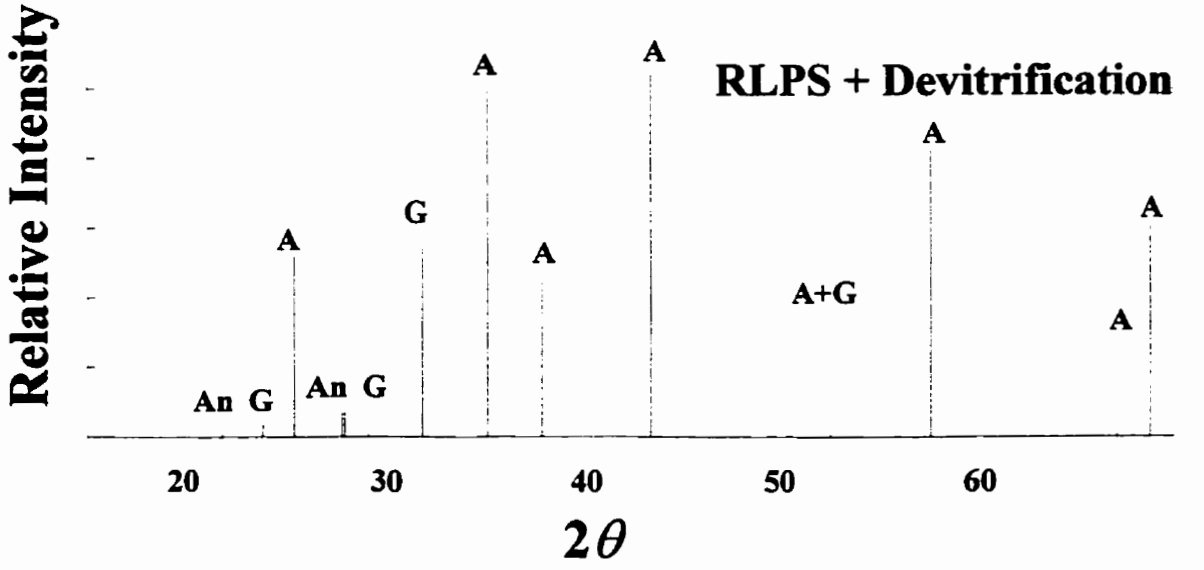

(b)

Figure 4-25. X-ray diffraction plots showing angles of peak occurrences and their relative intensity (a) the quenched CAS ceramic, and (b) the devitrified CAS ceramic.

This could be due to higher diffusivity of CaO inside the glass, which would favor production of gehlenite, the lime-rich compound. However, the higher proportion of gehlenite to anorthite leads to the appearance of free silica in the product (Figure 4-26). This would mean either a crystalline silica or residual glass. The appearance of crystalline silica was not found by XRD, so some residual glass is expected to be present. The residual alumina would tend to crystallize on the surface of existing alumina grains during the devitrification treatment.

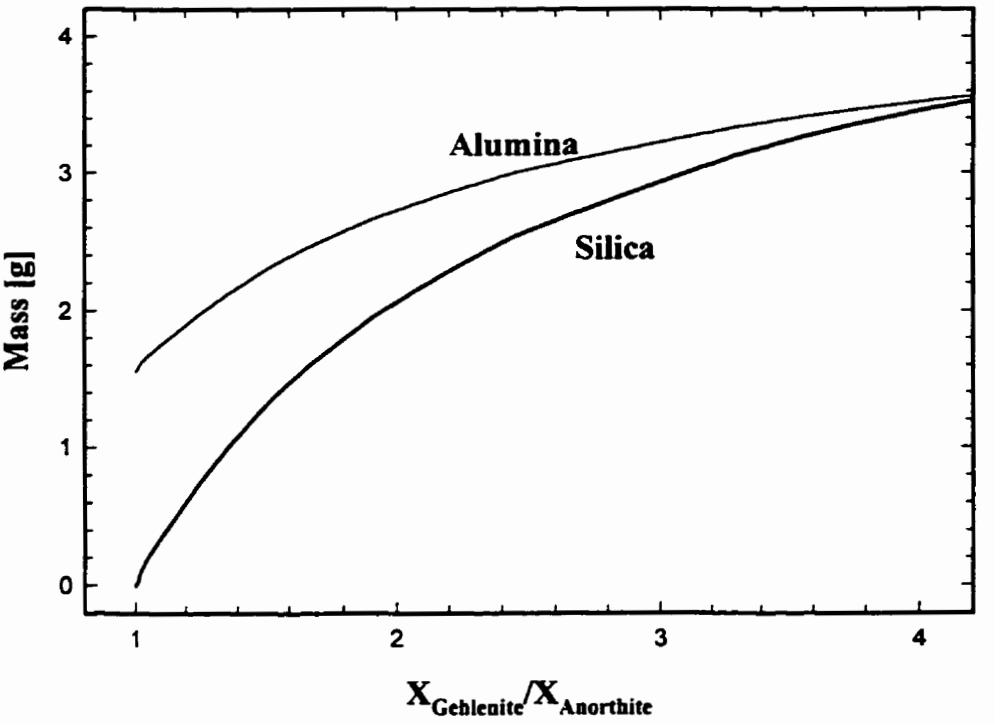

Figure 4-26. Residual products of a 100g devitrified CAS sample versus the molar ratio of gehlenite to anorthite products based on the EPMA measured composition of the parent glass.

4.4.3 Microscopy

Microscopic analysis was exclusively performed under an SEM using polished samples coated by either carbon or Au-Pd. Samples which were not polished included fracture surface specimens and green body specimens, which would break apart with any traditional sample preparation methods. The green body of the alumina - 20 wt% wollastonite is shown in Figure 4-27. The bright grains are the wollastonite powder.

Figure 4-27. SEM micrograph of the raw surface of an alumina + 20 wt% wollastonite green body.

Alumina samples which were sintered at 1560 C for 5 h and thermally etched for 2 h at 1500 C showed that the average grain size was approximately 3μm. CAS quenched

samples had no recognizable features under an SEM since the atomic number contrast of the components of the glass were close to that of the alumina, and because there were no clear grain boundaries visible. As a result, a chemical etch was performed using boiling phosphoric acid for 30 seconds. The glass in the microstructure easily dissolved in the acid, which enabled clear examination of the microstructure of the platelike alumina grains (Figure 4-28).

Figure 4-28. SEM backscatter micrograph of a quenched CAS ceramic which was heavily etched in boiling phosphoric acid to remove the glass from the microstructure.

As mentioned above, the structure of an unetched, polished surface of the quenched CAS ceramic revealed no compositional contrast and no grain boundaries. However, on a raw

(unpolished) surface there is considerable relief which makes it easy to see the alumina grains within the glass matrix (Figure 4-29).

Figure 4-29. SEM image of an unpolished quenched CAS ceramic surface revealing the platelet alumina grains and CAS glass.

The glass was analyzed using EPMA and was found to have a composition of 40 wt% alumina, 29 wt% CaO, and 31 wt% SiO_2. Alumina grains were confirmed to be 100 wt% alumina.

This sample was then heat treated using the devitrification schedule (1032 C for 4 hours + 1200 C for 4 hours) and re-examined. The same area of the sample shows no difference in

the alumina grains but the areas which formerly contained glass now seem to have crystalline structures visible (Figure 4-30).

Figure 4-30. SEM micrograph of the same area as Figure 4-21 after the devitrification treatment.

A closer look at the devitrification impact on the microstructure is shown in Figure 4-31. The dentritic crystals are easy visible in Figure 4-31(b). Clearly, the devitrification treatment has resulted in surface crystallization of some of the glass. This did not confirm if the crystallization occurred in the bulk of the glass.

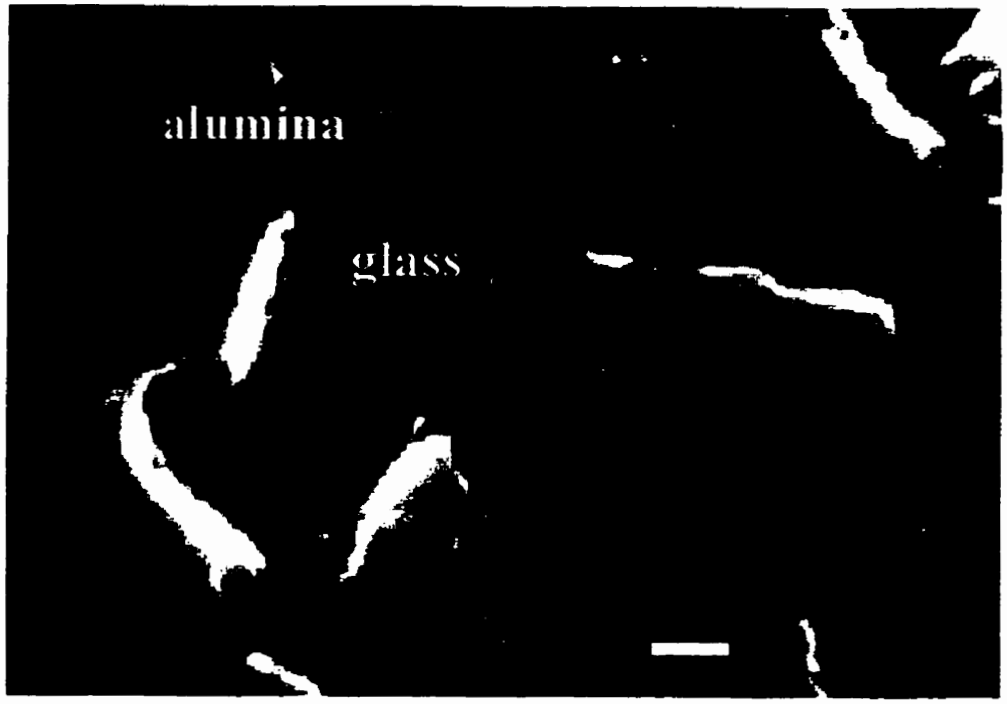

(a)

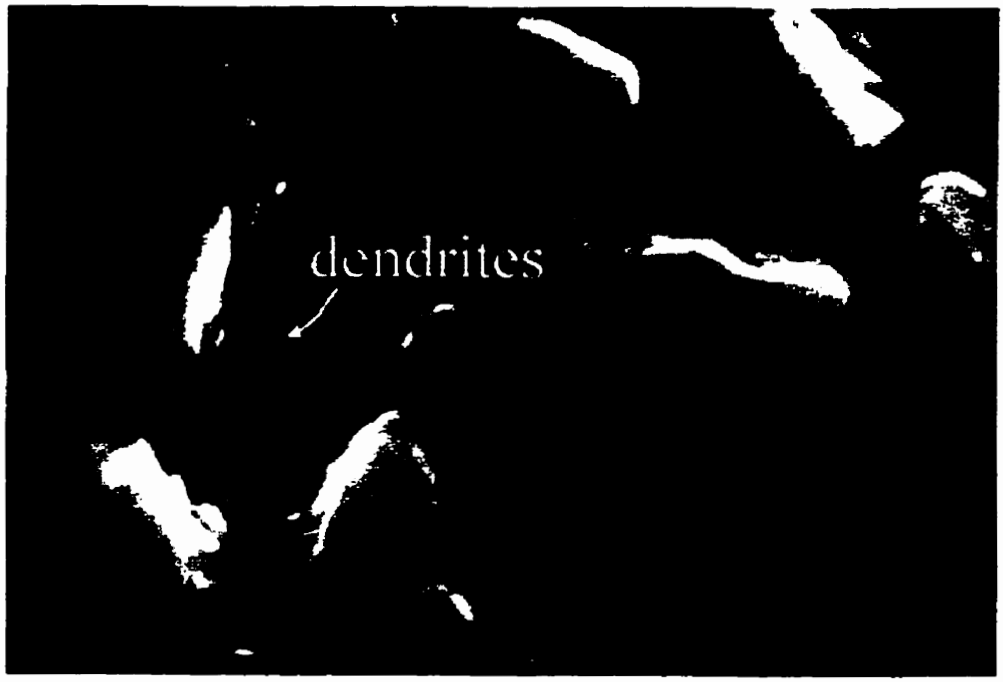

(b)

Figure 4-31. High magnification of (a) Figure 4-29 (before heat treatment), and of (b) Figure 4-30 showing dendritic crystals formed after devitrification (bars = 1μm).

By examining a polished surface of the devitrified CAS ceramic it was clear that the matrix glass was removed and all that remained was a light colored material present only at alumina grain boundaries (Figure 4-32). Since the X-ray diffraction proved that the devitrification treatment produced gehlenite and anorthite, it can be assumed that these compounds make up the newly visible phase. Unfortunately, the new crystalline phase was too fine to resolve using EPMA. Alumina grains within the CAS materials were found to be approximately 2μm with an aspect ratio of (2-2.5):1.

It is important to note the large amount of void space in the devitrfied CAS ceramic. This seems to be a result of the difference in density of the glass in comparison with the crystalline compounds. Unfortunately, exact determination of the relative amounts of phases present was not possible. As a result, only thermodynamic predictions using overall sample compositions and apparent alumina and glass amounts in the samples can be used to calculate a theoretical density. Assuming 57 vol% alumina (3.98 g/cc) is present in the CAS quenched material (determined using EPMA of the amount of alumina dissolved in the glass ≅ 13% of total, and confirmed by statistical analysis of the polished CAS sample images viewed under the SEM), and knowing the glass (2.6 g/cc approx. [51]) constitutes the rest of the material, the theoretical quenched CAS density is 3.39 g/cc. The measured density of the quenched CAS was only 2.89 g/cc which means that the theoretical density is only 85.3%. This finding shows that the LPS stage can not easily promote full densification due to the growing aspect ratio of the alumina grains.

If the devitrification fully crystallised the glass, the expected theoretical density of the CAS ceramic would be 3.54 g/cc. The measured bulk density of the CAS ceramic was found to be 3.05 g/cc, yielding a theoretical density of 86.2%. However, the low density is an advantage in many applications (especially in transportation related fields). As well, the unique microstructure may have beneficial crack deflection and crack blunting properties which result in higher fracture toughness.

Figure 4-32. Micrograph of polished CAS surface after devitrification.

4.5 Physical Properties

4.5.1 Shrinkage

Since the powder compact and the final densified CAS ceramic is assumed to be isotropic the shrinkage during liquid phase sintering and devitrification is assumed to be the same in all directions. However, this may be affected by (1) non-uniform pore distribution which is characteristic of green bodies formed during slip casting of most dispersed fine powder suspensions or by (2) gravity effects during liquid phase sintering which may cause higher size reductions in the direction of the gravitational force while reducing the degree of shrinkage in the directions normal to the force.

This effect was confirmed by liquid phase sintering various alumina + 20 wt% wollastonite green body pieces (ρ_{green} = 1.98 g/cc; ρ_{LPS} = 2.89 g/cc) and observing dimensional changes. According to predictions using the CAS ternary phase diagram, and the F*A*C*T thermodynamics software, about 40 wt% liquid phase will form at the process temperature of 1500 C. However, an estimate of CAS liquid density = 2.6 g/cc, based on published densities of similar glasses, gives a volumetric amount of liquid of 50 vol% (Figure 4-12). Microscopy, and EPMA of the quenched CAS ceramic proved that only about 40 vol% of glass (and thus liquid) was present. Higher amounts than this quantity would likely result in loss of green body macrostructure (forming a semi-solid "puddle" at 1500 C), which did not occur.

It was found that average linear shrinkage normal to the gravitational force was 16.5% while the shrinkage parallel to gravity was 22.9%. Therefore, particle rearrangement during sintering was aided by gravitation; this effect is important in processes which rely on near-net shape production.

4.5.2 Thermal Expansion

After devitrification of the CAS material, it was desired to characterize the thermal expansion property, in order to evaluate the susceptibility of the material to thermal shock. Once again, alumina was used as a control. The curve of linear expansion as a function of sample temperature is given in Figure 4-33.

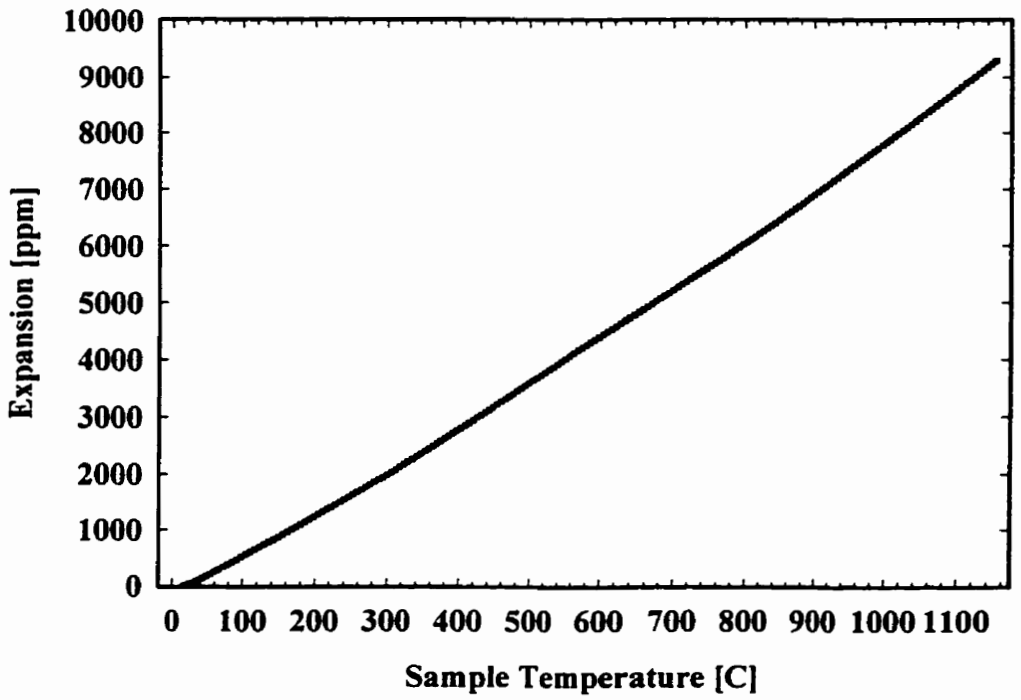

Figure 4-33. Expansion of the CAS ceramic as a function of temperature.

By determining the slope of the curve for various temperatures, the coefficient of linear thermal expansion can be plotted as a function of temperature (Figure 4-34). This graph shows the results found for the CAS ceramic as well as the alumina control sample and the published data for α-alumina.[119] Unfortunately, only one specimen of the CAS material was available for measurement, whereas the alumina control data was an average of two sample results.

The results show two interesting details. First is the leveling off of the CTE of the CAS sample between 450 and 750 C. This phenomenon is not easily explained, although it may be due to the presence of residual glass within the microstructure. The second, more practical result, is the fact that over a broad temperature range, the CAS ceramic exhibits lower thermal expansion than the alumina control. This suggests that, compared to alumina, the material is less sensitive to thermal shock, as thermal strain should be reduced over a given temperature change.

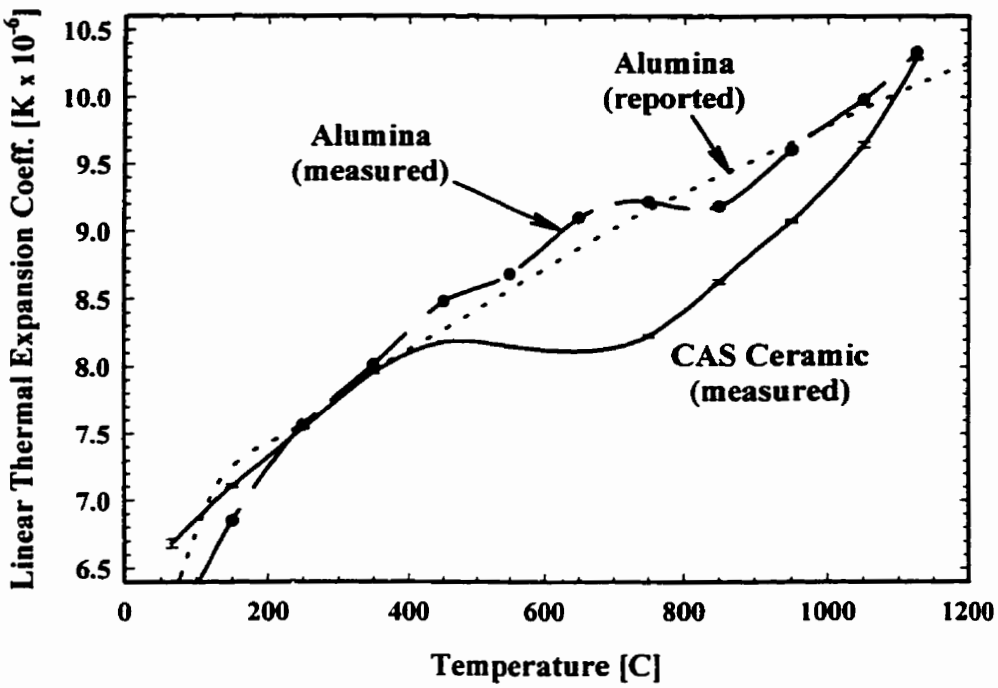

Figure 4-34. Coefficient of thermal expansion versus temperature for the CAS devitrified ceramic compared to published values for α-alumina.[119]

4.6 Mechanical Properties

The most important properties of a new ceramic intended for structural applications are the mechanical properties such as hardness, fracture toughness and strength.

4.6.1 Ultrasonic Measurements

Using ultrasonic test equipment, the Young's modulus (E) and Poisson's ratio (ν) were easily measured using small representative samples (at least two specimens) of each material. The results are presented in Table 4-1. Note the excellent agreement with published values for materials of similar composition.

Table 4-1. Results of ultrasonic measurements of Young's modulus and Poisson's ratio on ceramic samples. Materials in italics are reported values for similar materials (Alumina = >99% Al_2O_3 [108]; Aluminous porcelain = >50% Al_2O_3 (with glass) [108]; and C-780 class alumina = 80% Al_2O_3, 5% porosity [108,129])

	Alumina	*Alumina*	CAS quenched	*Aluminous Porcelain*	CAS devitrified	*C-780 Class* (@80% Al_2O_3)
E [GPa]	388.9 ± 6.48	*380*	145.9 ± 4.80	*100-180*	170.2 ± 2.57	*200*
G [GPa]	164.3 ± 1.01	*160*	61.47 ± 1.95	---	69.42 ± 1.06	*80*
K [GPa]	204.6 ± 12.12	*230*	77.55 ± 2.99	---	103.4 ± 1.65	*135*
ν	0.183 ± 0.013	*0.20 - 0.22*	0.186 ± 0.003	---	0.226 ± 0.002	*0.235*

Although dynamic modulus results obtained using ultrasonics are often somewhat higher than values measured using traditional means [108], values for the alumina control samples corresponded well with published data [4,108]. Since both the quenched and devitrified CAS materials have about 14% porosity, the theoretical elastic modulus can be estimated using the following relation [108],

$$E = E_o\left(1 - 1.9v + 0.9v^2\right) \qquad (4\text{-}6)$$

where E_o is the elastic modulus of the fully dense material and v is the volume fraction of porosity. By this relation, the full density values of E are 194 GPa for the quenched CAS

and 226 GPa for the devitrified CAS. The latter agrees well with the full density value for the 80% alumina C-780 data listed as 220 GPa.[129]

Clearly, there is a decrease in elastic properties with the quenched CAS and the devitrified CAS ceramics in comparison with alumina. In the case of the quenched material this can be explained by the presence of a large amount of the amorphous CAS. Predictably, the elastic moduli increase after the devitrification treatment. However, since a great quantity of porosity is present in the bulk of the devitrified CAS, the modulus values are still about half of the fully dense alumina.

Finally, it should be noted that devitrification causes a noticeable increase in Poisson's ratio, which may be a result of the increased bulk porosity in the microstructure.

4.6.2 Vickers Hardness

Hardness testing was easily performed using polished ceramic specimens. Diamond indentations were performed at loads of 5 and 50 kg. An example of a Vickers hardness indent is shown in Figure 4-35.

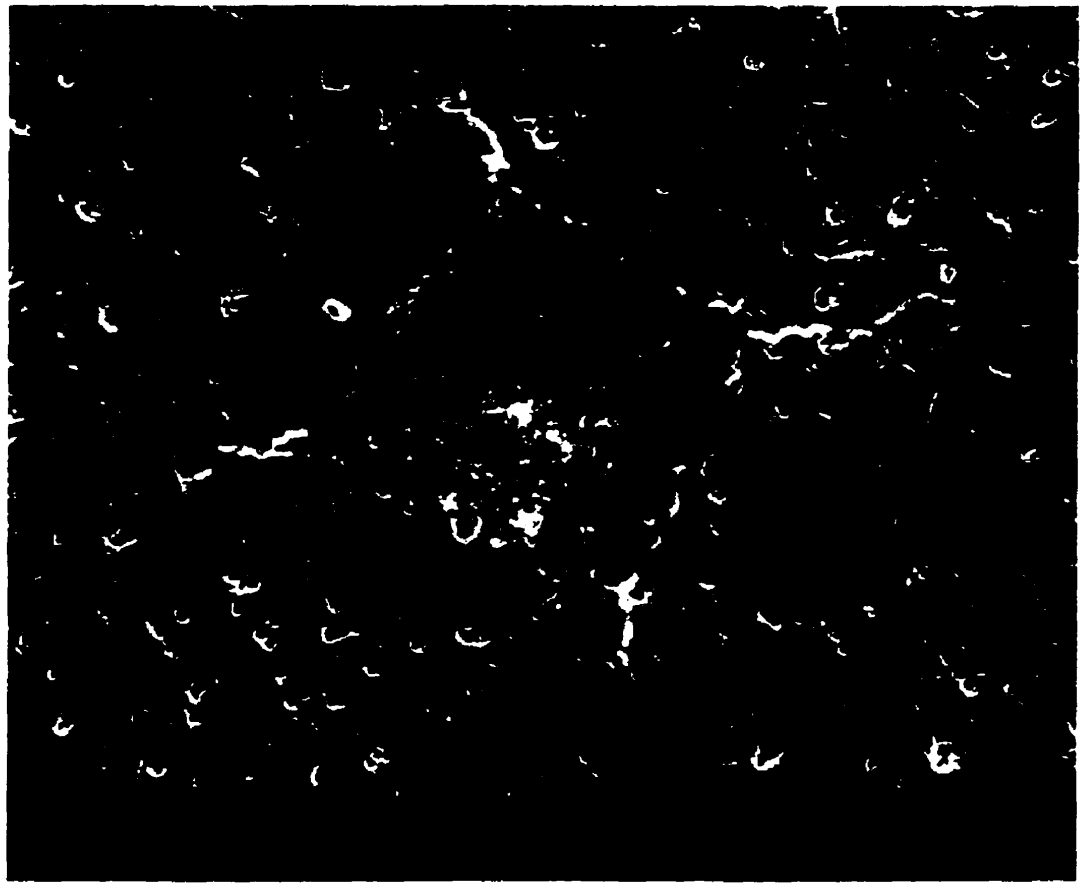

Figure 4-35. SEM micrograph of a Vickers diamond indent formed on a CAS sample under a 49 N load.

The hardness values of the alumina standard, the quenched CAS ceramic and the devitrified CAS samples are given in Table 4-2. It can be assumed that the hardness of the CAS is due primarily to the alumina grains in the microstructure, since the devitrification process has little or no effect on the observed hardness values. The hardness values for both the alumina and the devitrified CAS fall within the reported ranges for each specific material type (>99% alumina and C-780 Class respectively [108,129]).

Table 4-2. Vickers hardness for ceramic samples at various indentation loads. Ten indents were measured and averaged at each load.

Material	H_v, 49 N load [GPa]	H_v, 490 N load [GPa]
Alumina	17.4	14.57
CAS Devitrified	8.31	9.35

The devitrified sample removes the glass and leaves behind crystalline products in the alumina grain boundaries and a large amount of void space. As a result, the prime mechanical contribution to the overall properties is from the platelike alumina grains which constitute approximately 60 vol% of the material. When accounting for this proportion it can be seen that the CAS hardness corresponds to the amount of crystalline alumina present.

4.6.3 Indentation Toughness

Toughness values were computed using several K_c models [83,85-87] applied to the alumina standard, the quenched CAS and the devitrified CAS ceramics. An example of an 490 N indent on the CAS ceramic is shown in Figure 4-36, while Figure 4-37 shows a similar indent on an alumina specimen. Most models depend on the crack length and the applied load, while others include indent size or Young's modulus. A summary of the toughness variables is given in Table 4-3.

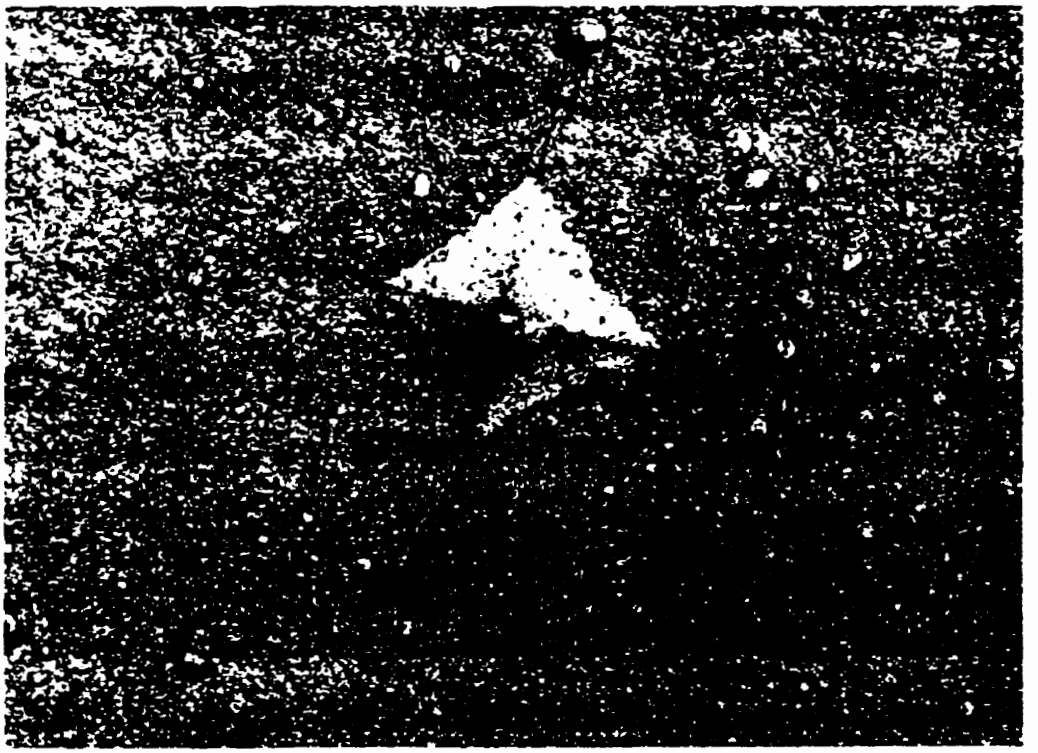

Figure 4-36. Negative SEM image of a Vickers indent (490 N) on a devitrified CAS sample.

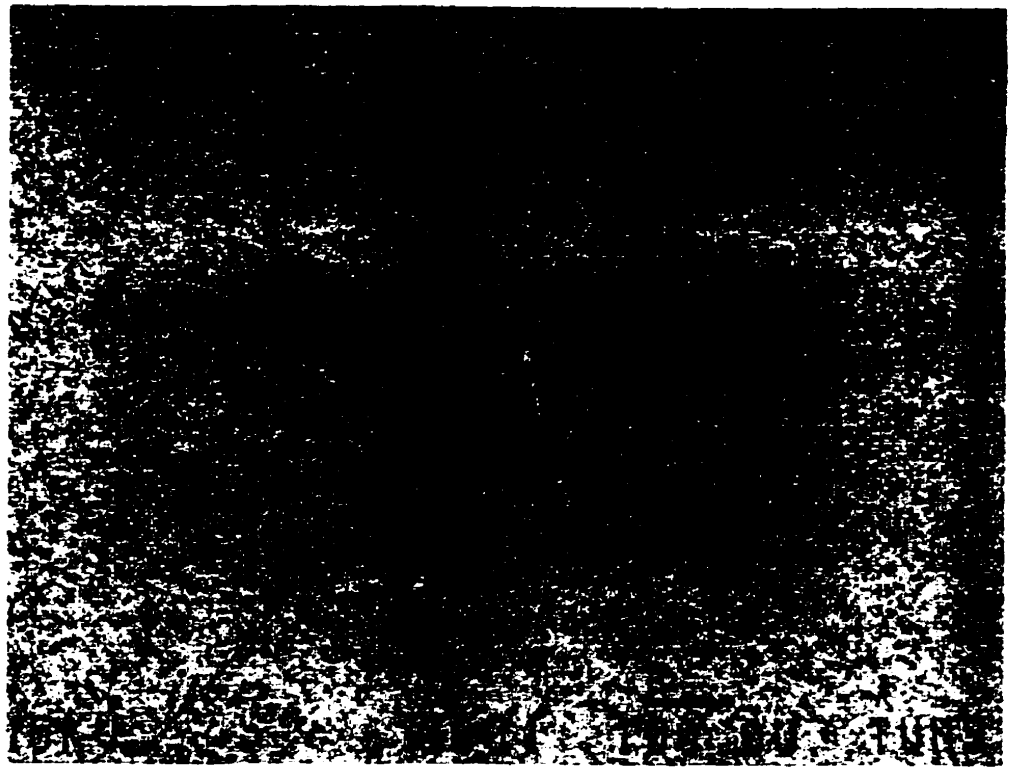

Figure 4-37. Negative SEM image of a Vickers indent formed on an alumina sample under a 490 N load.

Table 4-3. Indent properties for alumina and CAS ceramics. At least ten indents were measured for each sample.

Material	indent size, a [μm]	crack length, c [μm]	Load, P [N]	E/H_v	$P/c^{3/2}$ [$Nm^{-1.5}$]	c/a
Alumina	123.7	613.7	490	26.69	32.23	4.96
CAS quenched	76.4	157.9	98	18.75	24.70	2.07
CAS devitrified	156	420	490	18.20	56.90	2.70

By incorporating the above results, several estimations of mode I fracture toughness are possible (Table 4-4).

Table 4-4. Calculated K_c values for alumina and CAS ceramics using four indentation fracture models. Values in parentheses represent improvement in toughness values over the alumina material using the same model.

Fracture Toughness K_c, [MPa·m$^{1/2}$]	Alumina	CAS quenched	CAS devitrified
K_c, EC model	2.66	4.07 (+53.2%)	4.69 (+76.6%)
K_c, JL model	3.95	5.55 (+40.2%)	6.22 (+57.2%)
K_c, MS model	2.97	3.84 (+29.6%)	4.37 (+47.4%)
K_c, ME model	3.15	4.22 (+34.0%)	4.31 (+52.8%)
K_c, AC model	2.66	3.42 (+28.5%)	3.89 (+45.9%)
K_c (mean)	**3.08**	**4.22 (+37.1%)**	**4.80 (+55.8%)**

Moreover, they show excellent agreement when compared to published vales of fracture toughness for dense alumina of similar grain size (3μm), K_{Ic}=3.0 MPa·m$^{1/2}$.[87] Although the values differ to a degree between models, they all show significant improvement over the alumina control material.

Table 4-5 groups relative toughness values for broad classes of ceramic materials. Allowance should be made for departures from this grouping as a consequence of variations in microstructure in individual products. The K_c results given above tend to show that the devitrified CAS is approaching the high toughness category which includes zirconia toughened alumina.

Table 4-5. Grouping of ceramic materials by fracture toughness.[108]

K_{Ic} [$MNm^{3/2}$]	Ceramic types
<1 .0	Most single-crystal materials . Glasses of all types. Some glass-ceramics, particularly those of a very fine grain size or of high glass content.
1.0-2. 5	Most glass-ceramics. Most porcelains and other clay-based materials. Some alumina ceramics, particularly those of fine grain size designed for acid resistance. Some oxide ceramics, such as MgO.
2.5-5.0	Most alumina ceramics. Most dense non-oxide ceramics, B4C, SiC, Si3N4. Reaction-bonded silicon nitride. Many porous ceramics
5.0-15	Transformation-toughened ceramics based on alumina or zirconia. Low binder content hardmetals.
> 15	High binder content hardmetals . Some fibre-reinforced ceramics. Carbon fibre-reinforced carbon.

4.6.4 Modulus of Rupture

Measurement of ceramic strength is commonly reported using four point bend test results and is denoted as modulus of rupture (MOR). Ceramic specimens (machined according

to ASTM standard C 1161-94; specification B [107]; five specimens per material) were tested at a constant strain rate of 0.50 mm/min. The resulting strength data is given in Table 4-6.

Table 4-6. Modulus of rupture values for alumina and the crystallized CAS ceramic.

Material	Modulus of Rupture [MPa]	Strain at Failure [%]	Young's Modulus [GPa]
Alumina	497.5 ± 45.6	0.1325 ± 0.0096	331.0 ± 13.5
CAS devitrified	121.4 ± 12.6	0.0817 ± 0.0041	120.5 ± 12.9

It can be shown that although there is an expected discrepancy between the measurements of dynamic elastic modulus and the elastic modulus measured in the flexural test, both fall within the expected range (Figure 4-38).

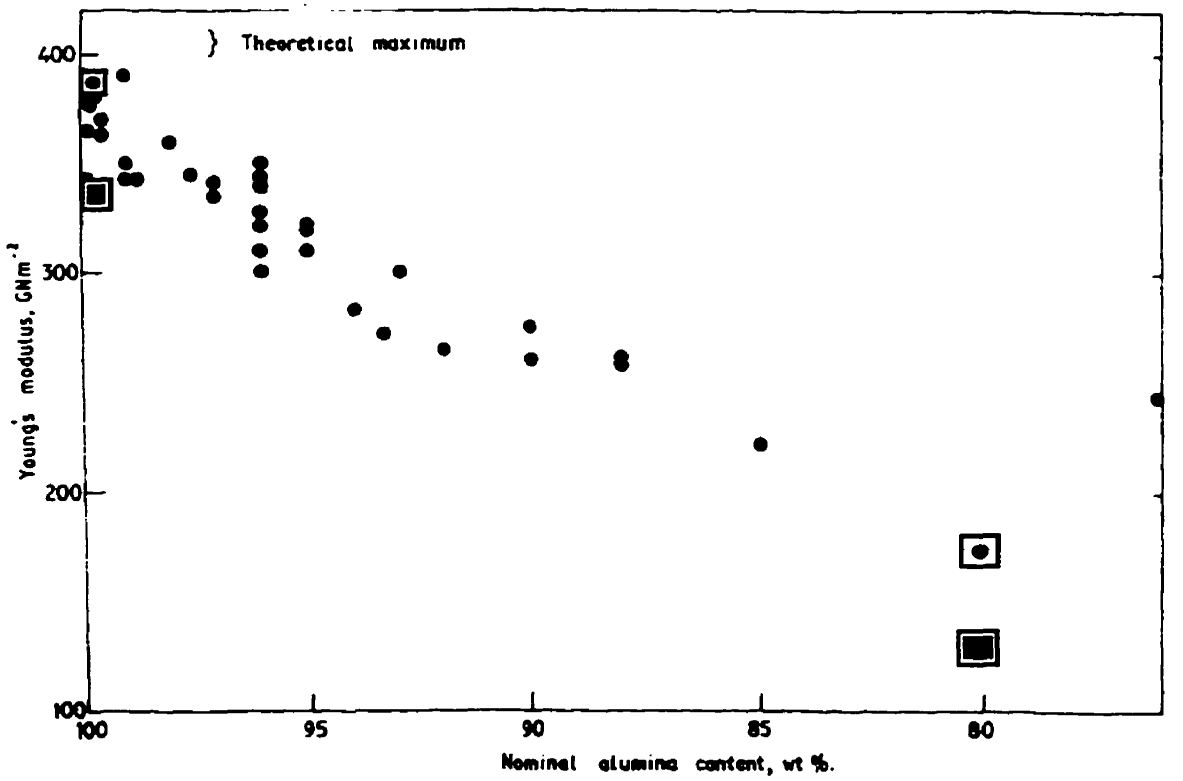

Figure 4-38. Plot of Young's modulus versus alumina content of the ceramic. Included are measurements made in this study; the boxed circles represent values measured using ultrasonic equipment, and the boxed squares show flexural values [108].

As well, the measured bend strength of the ceramics shows that the alumina has higher than anticipated strength, while the CAS ceramic falls within the projected range for high alumina ceramics as shown in Table 4-7. However, this guide is meant to be very general and includes data from many sources, using differing measurement parameters and sample quality.

Table 4-7. Grouping of ceramic material types by short-term strength.[108]

Very high strength, >400MPa
Hot-pressed silicon nitride, silicon carbide, boron carbide and alumina; Zirconia-toughened alumina, optimally-aged partially-stabilized zirconia; All-tetragonal zirconia; Sintered sialons and sintered silicon nitrides; Cemented carbides.
High strength, 200-400MPa
Most sintered aluminas of fine grain size; High-density reaction-bonded silicon nitride; Fine-grained reaction-bonded silicon carbide; Sintered silicon carbide; Thermally-strengthened soda-lime glass.
Medium strength, 100-200MPa
Aluminous porcelains of high alumina content, mullite ceramics, low-loss steatite and forsterite; Medium- to coarse-grained high-alumina ceramics and reaction-bonded silicon carbides; Low-density reaction-bonded silicon nitride; Beryllia, stabilized zirconia, titania; Opaque glass-ceramics; Single-crystal sapphire.
Low strength, 50-100MPa
Quartz and cristobalite porcelains, aluminous porcelains, normal steatite, vitreous cordierite; Coarse-grained porous silicon carbides; Magnesia ceramics, magnesium titanate; Glasses in the polished or flame-finished state; Transparent glass-ceramics, machinable glass-ceramics; Fired pyrophyllite; Single-crystal quartz.
Very low strength, < 50MPa
Porous electrical refractories, porous steatite and forsterite, porous cordierite; Glasses in the ground surface condition; Talc, machinable alumina, sintered fused silica.

These results show that the primary source of strength within the ceramic appears to be the contribution of the alumina grains within the microstructure. The low hardness values appear to be due to the large void space between the grains of the devitrified CAS material. The removal of the glass appears to have little or no impact on many of the physical or mechanical properties, though anecdotal evidence tends to support the theory that impact toughness is greatly improved after the devitrification treatment.

The lath or platelike structure of the liquid phase sintered alumina seems to improve toughness by crack deflection. This finding confirms previous results reported for this type of alumina grain shape. The fracture surface when viewed under an SEM appears to have a rough texture, and the crack front follows the edges of the alumina grains, as evidenced by the flat texture of the unbroken alumina crystals (Figure 4-39). Though the strength has decreased because of the porosity of the microstructure, the corresponding increase in fracture toughness will make the resulting ceramic very applicable to aggressive physical environments.

Figure 4-39. Secondary electron SEM image of a devitrified CAS ceramic fracture surface.

4.6.5 Thermal Shock

When accounting for thermal shock, the tensile data is not readily obtainable, so an estimate is used by referring to published values for similar materials (alumina = 255 MPa [4] and C-780 Class ceramic (85% Al_2O_3) = 115 MPa [129]); the thermal expansion coefficient is taken from 600 C. The values of the thermal shock parameter, R, are 61 K for alumina and 65 K for the devitrified CAS; meaning that the CAS can withstand slightly higher changes in temperature without developing catastrophic thermal stresses

within the microstructure. This finding is very preliminary and needs to be verified through tensile strength measurement and actual thermal shock experimentation. Note also that the tensile values employed may weight the thermal shock data unfairly, and published values of R for alumina prove this (R = 90 K reported in reference [108]). However, C-780 Class alumina ceramic reports R as high as 180 K.[129]

As a result, it can only be stated that the lower thermal expansion and elastic modulus of the devitrified CAS do not overcome the high inherent strength of pure alumina when accounting for relative thermal shock performance.

4.6.6 Abrasive Wear Resistance

In an abrasive wear application, a decrease in hardness coupled with increased toughness would be ideal in minimizing wear rates. One relation is given by [109],

$$p_{crit} \propto \left(\frac{K_c}{H}\right)^2 \tag{4-7}$$

where p_{crit} is the critical contact groove size. When hardness and toughness data for the CAS ceramic and the alumina control are contrasted using this relation, it was found that the CAS ceramic can withstand six times the critical contact groove size of alumina.

Another wear relation is given by [109],

$$L_{crit} \propto K_c \cdot \left(\frac{K_c}{H}\right)^3 \tag{4-8}$$

where L_{crit} is the critical contact load. Data for hardness and toughness of alumina and the CAS ceramic, when compared using the load relation (4-8), suggest that, under similar conditions, the devitrified composite CAS has 22 times the abrasion load resistance compared to full density alumina.

Thus, it is expected that this CAS would have properties which make it amenable to anti-abrasion applications, which is not unexpected, since similar C-780 Class ceramics are used for wear parts, milling media, and abrasion-resistant linings.[129] Uniquely, however, the devitrified CAS incorporates a large amount of low-cost wollastonite as a raw material, which lowers the cost of the final product. As well, the comparatively short firing time at 1500 C reduces manufacturing energy costs.

A review of the properties of alumina and the CAS ceramic is provided in Table 4-8.

Table 4-8. Summary of CAS ceramic properties compared to alumina.

Material	H_V [GPa]	K_c [MPa $m^{1/2}$]	E [GPa]	ρ [g/cc]	MOR [MPa]	$\alpha_{600\ C}$ [K^{-1} x10^{-6}]
Alumina	14.6	3.08	388.9	3.97	497	8.7
CAS Ceramic	9.35	4.80	170.2	3.02	121	8.1

5. DISCUSSION

Great strides have been made over the past few decades in resolving the brittle nature of ceramics. Most often, these solutions involve incorporation of a secondary phase which limits crack propagation and thus increases overall toughness. The resulting ceramic matrix composite (CMC) may have new properties which make it suitable for a wide range of applications.

All of these reinforcement techniques require special processing techniques and expensive man-made raw materials which result in a high cost final product. As well, often the final size and shapes of the product are limited when special production techniques are employed (e.g., hot-isostatic pressing for many whisker or fibre based composites).

It was felt that an innovative approach was required to produce a ceramic with high strength and toughness, using a simple processing method and inexpensive raw materials. The low-cost mineral wollastonite ($CaO{\cdot}SiO_2$) was considered to be an ideal candidate for investigation as a secondary ingredient in an alumina-based ceramic, due to its relatively low cost (produced using large scale mineral processing techniques at approximately $25/tonne) and compatibility with alumina systems. For instance, the CaO-Al_2O_3-SiO_2 system includes slags, glass materials, cements, and new types of glass-ceramics produced for high strength applications.

By introducing wollastonite into an alumina matrix (greater than 50 wt% alumina), reactions at high temperatures are expected. The phase diagram for the system predicts that above 1400 C the equilibrium structure will contain only crystalline alumina and liquid whose quantity and composition will depend on the amount of wollastonite initially present. This presence of a liquid has both benefits and drawbacks since it will dramatically increase densification rates but will inevitably result in the presence of a mechanically weak glass within the microstructure. This problem can be counteracted using post-sintering heat treatments.

To preserve a structural shape during liquid-phase sintering, it is necessary to maintain the amount of liquid present in the structure to below about 25 vol%. This restricts the amount of wollastonite to about 20 wt% in the initial green body. This composition was the one chosen for most of the characterization.

Wet processing and slip casting were felt to be the best techniques to produce a green body due to their flexible nature and adaptability to high volume production. The challenge was to determine the optimum processing conditions necessary to produce a homogenous dense composite body.

The first step was to find the pH range which would be appropriate to produce a good aqueous dispersion. Initial work showed that between pH 2 and 6 colloidal alumina (grain size = 0.5 microns) produced little or no sediment in a 5 vol% solids suspension after 20 hours. This indicated that Brownian motion and inter-particle repulsion was sufficient to

maintain a stable suspension within this range of pH. This range was verified using viscosity testing of dense aqueous suspensions of alumina (>35 vol% solids).

When the wollastonite was introduced, its alkaline nature tended to shift the suspension pH into the flocculation range and probably caused some hetero-flocculation. Thus a greater amount of acid was necessary, and the electrical double layer (which acted to repel individual particles) became compressed due to the high ionic content of the fluid. As a result, poor and unstable suspension conditions were inevitable.

Thus, a polymeric dispersant was necessary to provide a steric hinderance to prevent particle flocculation. Several anionic polyelectrolytes were evaluated (Darvan C, Darvan 821A, Emphos CS361, and Dolapix PC75) and best results were found using Darvan C at about 30 ppm at pH 3.0. This recipe resulted in a maximum green density of 53 % of theoretical.

New research suggested that a cationic polyelectrolyte normally used as a flocculant in water purification, BETZ 1190 (quaternized polyamine epoxychlrohydrin), when used in high concentrations (>1000 ppm) was an effective dispersant in chemical systems, particularly for systems involving two constituents with different surface properties. Using this recommendation, the maximum density improved to over 60% using 1500 ppm CPE at pH = 3.0.

From here, it was necessary to find an appropriate high temperature sintering technique which would result in a high density, crystalline product. According to the phase diagram

and thermodynamic calculations, it was predicted that a liquid phase would form above 1400 C. This fact was confirmed using thermogravimetric analysis (TGA) and differential thermal analysis (DTA). Scanning electron microscopy combined with EPMA and X-ray diffraction proved that the structure of the composite sintered above this temperature contained only laths (or platelet) of alumina grains and glass. Indentation testing of such a material showed very low toughness values as a result of the glass within the microstructure.

Slow cooling of the ceramic at the anticipated solidification temperature produced limited and unpredictable amounts of hibonite ($CaO{\cdot}6Al_2O_3$). A post-sintering heat treatment had limited success in crystallizing the glass after 12 hours at 1200 C.

Methods to crystallize glass structures (devitrification) normally involve treating the glass at a temperature which promotes the formation of crystal nuclei within the bulk of the glass, followed by a crystallization treatment at a slightly higher temperature. Unfortunately, nucleation temperature is not apparent using standard thermal analysis.

Some researchers have found that by varying the nucleation treatment conditions it was possible to observe changes in the crystallization peak produced using high heating rate DTA. When few nuclei were present (a poor nucleation treatment) the observed crystallization peak was shallow, broad and commenced at a high temperature. When nucleation was optimized, the crystallization peak shifted to lower temperatures and was much higher and sharper than other peaks. Thus, indirectly, a proper nucleation treatment temperature can be found.

Using this method it was found that the optimum devitrification technique was to sustain a nucleation temperature of 1032 C for four hours, followed by crystallization for four hours at 1200 C. Though it was difficult to verify using microscopy and EPMA, X-ray diffraction results showed that the treatment resulted in the formation of crystalline gehlenite ($2CaO{\cdot}Al_2O_3{\cdot}SiO_2$) and anorthite ($CaO{\cdot}Al_2O_3{\cdot}2SiO_2$). The presence of hibonite, though expected, was not confirmed. This may be a result of slow formation kinetics. A summary of the production sequence is given in Figure 5-1.

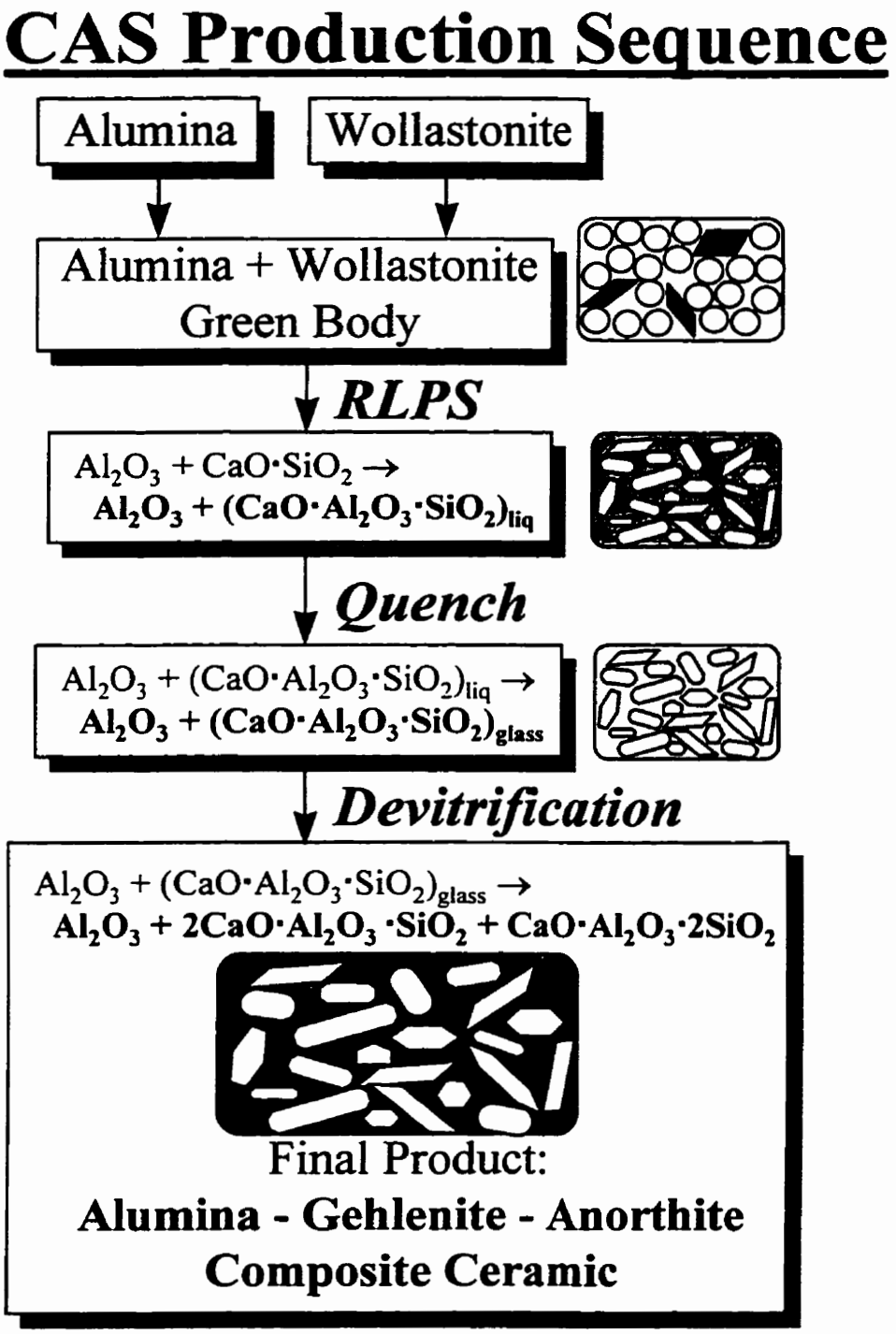

Figure 5-1. Summary of the CAS ceramic production method.

Fracture surfaces of the new "CAS" (C = CaO, A = Al_2O_3, S = SiO_2) ceramic show that cracks follow a long, intergranular path along faceted surfaces of the alumina grains.

Vickers hardness combined with modulus of rupture data show that the porous nature of the devitrified CAS ceramic is weaker than similar grain size alumina. However, using a Vickers diamond indentation technique to evaluate ceramic toughness, it was found that the new product has a noticeable improvement in toughness (56%). Toughness is one of the most vital aspects of a ceramic's performance, so this benefit outweighs the poorer strength and hardness.

In fact, the combination of lower hardness and higher fracture toughness make it attractive for anti-abrasion applications. At the same time the use of 20 wt% of the low cost wollastonite and the reduced energy costs anticipated with the fast firing cycle at 1500 C make devitrified CAS a cost competitive material for applications where abrasive wear is a prime concern.

6. SUMMARY AND CONCLUSIONS

1) Wollastonite can be crushed to a smaller grain size using a shatterbox mill with an alumina mortar/pestle. Mean particle size of the grains was reduced from 30 μm to 4.5 μm after 10 minutes of crushing. Longer crushing times did not significantly reduce the size as the material began to heat up and cake against the sides of the pestle. Crushing in this way also reduced the aspect ratio of the larger grains from 10:1 down to 3:1.

2) Alumina slips containing 0.45 μm grains were optimized at a pH of 4.0 and with a maximum green density of 2.74 g/cc (69 %TD). These samples were fired to 99 %TD at 1520 C for 8 hours with a grain size of 3μm.

3) Combining the material in an aqueous suspension produced a slip with poor pH control due to the alkaline nature of wollastonite. The window of pH dispersion, based on viscosity tests, was found to change from pH 2-6 for alumina to pH 1-3 for alumina + wollastonite.

4) Use of a polymeric dispersant was required to improve dispersion stability. Several anionic polyelectrolyte dispersants were tested: Emphos CS361, Dolapix PC-75, Darvan 821A and Darvan C, the latter being the most effective. The concentration was optimized at 30 ppm, with an optimum green density of an alumina + 10 vol% wollastonite body of 55.6 %TD.

5) Subsequent testing using a high concentrations (>1000 ppm) of a cationic polyelectrolyte, BETZ 1190, showed higher green densities of the alumina + 10 vol% wollastonite system were achievable: 2.49 g/cc = 65 %TD at 1500 ppm BETZ 1190, at pH 2.3.

6) Using F*A*C*T thermodynamic software and database, it was determined that above 1400 C the system would contain only crystalline alumina and a liquid phase at equilibrium. The amount of liquid was dependent upon the amount of wollastonite in the body and therefore, to maintain body structure during liquid phase sintering, it was decided to limit the wollastonite to 20 wt%. As well, the LPS temperature was set at 1500 C to ensure appearance of the liquid phase without producing an excessive amount.

7) The thermodynamic software also predicted the appearance of gehlenite and anorthite in a crystallised product.

8) A simple DTA apparatus was prepared and a DTA scan of green alumina + wollastonite bodies showed the transformation of wollastonite to pseudo-wollastonite at about 1100 C, followed by a small undefined endothermic peak at 1250 C, and finally an alumina dissolution peak after the appearance of a liquid phase at 1370 C.

9) Air-quenching of the alumina + 20 wt% wollastonite system from 1500 C formed a CAS (lime-alumina-silica) glass. This material was measured by DTA and showed evidence of a crystallisation peak at 1280 C.

10) Nucleation heat treatments over a broad temperature range produced noticeable changes in the DTA crystallisation peak (peak height, peak width, and peak shift to lower temperatures). Using these observations it was determined that optimum bulk (homogenous) nucleation occurred at 1032 C. The glass phase could be subsequently crystallised by heat treating at 1200 C.

11) Thus the optimised furnace schedule was: i) heat to 1500 C, ii) maintain for 15 minutes, iii) cool quickly to <900 C, iv) heat to 1032 C for four hours, v) quickly ramp to 1200 C, vi) maintain 1200 C for four hours, vii) cool to room temperature.

12) Electron probe microanalysis showed that the parent glass in the quenched CAS ceramic consisted of 39% alumina + 29% calcia + 32% silica. Anorthite and gehlenite crystallisation products in the devitrified CAS ceramic were too fine to be verified with this method.

13) X-ray diffraction of the products showed that the only crystalline phase present after liquid phase sintering was alumina. After nucleation and crystallisation gehlenite and anorthite were found with the alumina in the devitrified product.

14) Scanning electron microscopy of a polished liquid phase sintered CAS sample showed no observable grain structure. After nucleation and crystallisation the alumina

grains were clearly visible along with a significant amount of porosity (14 %). As well as brighter phase along grain boundaries is the crystallization products (gehlenite and anorthite). Images of a non-polished surface before and after the crystallisation treatment showed a distinct appearance of a dendtritic product between alumina grains where the CAS glass was formerly present.

15) Thermal expansion data showed that the devitrified CAS ceramic had slightly lower thermal expansion than alumina between 450C and 1050 C. For example at 600 C the CTE for alumina and the devitrified CAS is 9.0×10^{-6} and 8.1×10^{-6} K^{-1} respectively. This result, combined with strength data implies that alumina and the devitrified CAS have similar thermal shock resistance, although more extensive testing would be required to verify this.

16) Ultrasonic measurements of elastic modulus and Poisson's ratio showed good agreement with materials of the same class given in various literature sources. Alumina had a dynamic Young's modulus of 389 GPa compared to 170 GPa for the devitrified CAS.

17) Vickers hardness (10 kg load) of the alumina was 14.6 GPa, while the devitrified CAS was 9.35 GPa.

18) Using measurements of cracks generated at Vickers indents under defined loads, it was found that the devitrified CAS has a toughness of 4.80 $MPa{\cdot}m^{1/2}$ compared to

3.08 MPa·$m^{1/2}$ for the alumina. This 56% improvement in toughness was shown to be principally due to the new shape of the alumina grains combined with the porous microstructure.

19) Flexural strength using a four point load showed very high strength for the alumina (498 MPa) compared to the devitrified CAS (121 MPa).

20) The results of the wet processing experiments showed that suitable homogeneous bodies consisting of alumina and wollastonite could be formed using slip casting with the aid of a polymeric dispersant.

21) It was found that the liquid phase sintering (LPS) technique allowed for slip cast bodies with low green density, since the liquid diffusion during sintering removes most porosity. The final porosity of 14% reflects the change in the microstructure during devitrification (the lower density CAS glass forming into higher density crystalline phases).

22) Given the above mentioned properties, it was suggested that this new reduced-cost material is ideal for applications in which abrasive wear resistance is critical. Indeed, using two wear relations it was shown that the devitrified CAS has much better wear resistance than common alumina ceramics.

7. REFERENCES

1) Bowen, H.K., "Basic Research Needs on High Temperature Ceramics for Energy Applications", *Materials Science and Engineering*, **44**, pp 1-56 (1980).

2) Evans, A.G. "Perspective on the Development of High-Toughness Ceramics", *Journal of the American Ceramic Society*, **73** [2], pp. 187-206 (1990).

3) Becher, P.F., "Microstructural Design of Toughened Ceramics", *Journal of the American Ceramic Society*, **74** [2], pp. 255-269 (1991).

4) Richerson, D.W., Modern Ceramic Engineering, G. Boothroyd and G.E.Deiter eds., Marcel Dekker, Inc., New York (1982).

5) Schioler, L.J., and Stiglich, J.J., "Ceramic Matrix Composites: A Literature Review", *American Ceramic Society Bulletin*, **65** [2], pp. 289-292 (1986).

6) Prewo, K.M., Brennan, J.J., and Layden, G.K., "Fibre Reinforced Glasses and Glass-Ceramics for High Performance Applications", *American Ceramic Society Bulletin*, **65** [2], pp. 305-313, 322 (1986).

7) Cranmer, D.C., "Overview of Technical, Engineering, and Advanced Ceramics"; Hench, L.L., "Medical and Scientific Products"; Haertling, G.H., "Electrooptic Ceramics and Devices"; Bocko, P.L., and Whitney, R.K., "Information Display"; Shaw, R.R., "Electronic Processing and Electronic Devices"; and Miska, H.A., "Aerospace and Military Applications" all from Engineered Materials Handbook - Volume 4: Ceramics and Glasses, ASM International, Metals Park, OH (1992).

8) Mangin, C.G.E., Neely, J.E., and Clark, J.P., "The Potential for Advanced Ceramics in Automotive Engine Applications", *JOM*, June, pp. 23-27 (1993).

9) Caley, W.F., Kipouros, G.J., and Kingston, P.W., "The Potential Application of Natural Minerals in Ceramic and Metal-Matrix Composites", *CIM Bulletin*, **86** [968], pp.116-121 (1993).

10) Bryden, R.H., Deveau, E.M., Konsztowicz, K.J., and Caley, W.F., "Industrial Minerals as Strengthening Agents in Ceramic Matrix Composites", in proceedings: Developments and Applications of Ceramics and New Metal Alloys, 32nd CIM Conference of Metallurgists, pp. 357-362 (1993).

11) Fattah, H., "Wollastonite - New aspects promise growth", *Industrial Minerals*, [326], November, pp.21-43 (1994).

12) MacKinnon, A., "Wollastonite in Southeastern Ontario", *Ontario Geological Survey - Open File Report 5715*, (1990).

13) Springer, J., "Ontario Wollastonite: Uses, Markets and Ontario's Potential as a Future Producer", *Industrial Mineral Background Paper #17*, Mineral Development Section, Ministry of Northern Development and Mines, Queens Printer of Ontario (1994).

14) Janeway, P.A. (editor), "Materials Handbook for Refractories, Traditional, Advanced Ceramics", *Ceramic Industry*, **140** [1], pp. 37-118 (1993).

15) Griffith, A.A., "The Phenomenon of Rupture and Flow in Solids", *Philosophical Transactions of the Royal Society of London Serials A*, **221** [4], p. 163 (1920).

16) Park, S.-Y., "Influence of a Liquid Phase on the Microstructure Development of Al_2O_3", *Journal of Materials Science*, **15**, pp. 878-880 (1996).

17) Kaysser, W.A., Sprissler, M., Handwerker, C.A., and Blendell, J.E., "Effect of a Liquid Phase on thc Morphology of Grain Growth in Alumina", *Journal of the American Ceramic Society*, **70** [5], pp. 339-43 (1987).

18) Hansen, S.C., and Philips, D.S., "Grain Broundary Microstructures in a Liquid-Phase Sintered Alumina (α-Al_2O_3)", *Philosophical Magazine A*, **47** [2], pp. 209-234 (1983).

19) Song, H., and Coble, R., "Morphology of Platelike Abnormal Grains in Liquid-Phase-Sintered Alumina", *Journal of the American Ceramic Society*, **73** [7], pp. 2086-2090 (1990).

20) Song, H., and Coble, R., "Origin and Growth Kinetics of Platelike Abnormal Grains in Liquid-Phase-Sintered Alumina", *Journal of the American Ceramic Society*, **73** [7], pp. 2077-2085 (1990).

21) Koyama, T., Nishiyama, A., and Niihara, K., "Effect of a Small Amount of Liquid-Forming Additives on the Microstructure of Al_2O_3 Ceramics", *Journal of Materials Science*, **28**, pp. 5953-5956 (1993).

22) Koyama, T. , Nishiyama, A., and Niihara, K., "Effect of Grain Morphology and Grain Size on the Mechanical Properties of Al_2O_3 Ceramics", *Journal of Materials Science*, **29**, pp. 3949-3954 (1994).

23) Boccaccini, A.R., "Sintering of Glass Matrix Composites Containing Al_2O_3 Platelet Inclusions", *Journal of Materials Science*, **29**, pp. 4273-4278 (1994).

24) Kingery, W.D., Bowen, H.K., and Uhlmann, D.R., Introduction to Ceramics, John Wiley & Sons, New York, (1976).

25) Veasey, T.J., "Recent Developments in the Production of Glass-Ceramics", *Mineral Science and Engineering*, **5** [2], pp. 92-107 (1973).

26) McHale, A.E., "Engineering Properties of Glass-Ceramics", from Engineered Materials Handbook - Volume 4: Ceramics and Glasses, ASM International, Metals Park, OH (1992).

27) Bergeron, C.G., and Risbud, S.H., Introduction to Phase Equilibria in Ceramics, American Ceramic Society, Columbus, OH, p. 116 (1984).

28) Norton, F.H., Elements of Ceramics, 2nd edition, Addison Wesley Publishing, Reading, MA (1974).

29) Flinn, R.A. and Trojan, P.K., "Ceramic Structures and Their Properties", in: Engineering Materials and Their Applications, 3rd ed, Houghton Mifflin Company, Boston, MA (1986).

30) Morris, W. (editor), The American Heritage Dictionary of the English Language, American Heritage Publishing and Houghton Mifflin Co., Boston, MA (1970).

31) Bradstreet, S.W., "Oxide Ceramics", Chapter 8 in High-Temperature Materials and Technology, John Wiley & Sons, New York (1967).

32) Kanzaki, S., Ohashi, M., and Tabata, H., "Mullite-Silica Ceramics for Insulating Substrate Material", from Ceramic Transactions - Volume 6: Mullite and Mullite Matrix Composites, American Ceramic Society, Westerville, OH, pp. 389-399 (1990).

33) Levin, E.M., Robbins, C.R., and McMurdie, H.F., Phase Diagrams for Ceramists, American Ceramic Society, Columbus, OH, p. 104 (1964).

34) Lea, F.M., The Chemistry of Concrete, 3rd edition, Edward Arnold (pub), Glasgow (1970).

35) Roth, R.S., Negas, T., and Cook, L.P., Phase Diagrams for Ceramists, Volume IV, American Ceramic Society, Columbus, OH, p.95 (1981).

36) Gentile, A.L., and Foster, W.R., *Journal of the American Ceramic Society*, **46** [2], p. 76 (1963).

37) Shelby, J.E., "Formation and Properties of Calcium Aluminosilicate Glasses", *Journal of the American Ceramic Society*, **68** [3], pp. 155-158 (1985).

38) Beall, G.H., "Refractory Glass-Ceramics", Chapter 2 in High Temperature Oxides - Part IV: Refractory Glasses, Glass-Ceramics, and Ceramics, Academic Press, New York (1971).

39) Stookey, S.D., "Method of Making Ceramics and Product Thereof", *US Patent 2,920,971*, January 12 (1960).

40) Topping, J.A., "Glass-Ceramics from the System CaO - Al_2O_3 - SiO_2", *American Ceramic Society Bulletin*, **56** [6], pp. 574, 577 (1977).

41) Monteiro, R.C.C., Glasser, F.P., and Lachowski, E.E., "Crystallization of CaO - Al_2O_3 - SiO_2 and CaO - MO - Al_2O_3 - SiO_2 (M = Mg, Zn)", *Journal of Materials Science*, **24**, pp. 2839-2844 (1989).

42) Sletson, L.C., and Reed, J.S., "Microstructure Development in a Vitrified Anorthite Porcelain", *American Ceramic Society Bulletin*, **67** [8], pp. 1403-1408 (1988).

43) Vassileva, V., Gatev, E., Lepkova, D., and Grunova, P., "X-ray Quantitative Phase Analysis of Anorthite in Electric Insulation Ceramics", *Journal of Materials Science Letters*, **9**, pp. 741-742 (1990).

44) Dan, T.K., Chand, N., and Rohatgi, P.K., "Effect of Glass, Rice-Husk Ash and Wollastonite on Transverse Strength of Porcelain", *Journal of Materials Science Letters*, **6**, pp. 277-280 (1987).

45) Sainamthip, P., and Reed, J.S., "Fast-Fired Wall Tile Bodies Containing Wollastonite", *American Ceramic Society Bulletin*, **66** [12], pp. 1726-1731 (1987).

46) Kokubo, T., Ito, S., Shigematsu, M., Sakka, S., and Yamamuro, T., "Fatigue and Life-time of Bioactive Glass-Ceramic A-W Containing Apatite and Wollastonite", *Journal of Materials Science*, **22**, pp. 4067-4070 (1987).

47) Jean, J.-H., Lin, S.-C., and Chang, C.-R., "Low-Temperature, Low-Dielectric, Crystallizable Glass Composite", *IEEE Transactions on Components, Packaging, and Manufacturing Technology - Part B*, **18** [4], pp. 751-754 (1995).

48) Wirth, D.G., "Ceramic Substrates", from Engineered Materials Handbook - Volume 4: Ceramics and Glasses, ASM International, Metals Park, OH (1992).

49) Tummala, R.R., "Ceramic and Glass-Ceramic Packaging in the 1990's", *Journal of the American Ceramic Society*, **74** [5], pp. 895-908 (1991).

50) Thorp, J.S., Akhtaruzzaman, M. and Evans, D., "The Dielectric Properties of Alumina Substrates for Microelectronic Packaging", *Journal of Materials Science*, **25**, pp. 4143-4149 (1990).

51) Schercliff, H.R., Vekinis, G., and Beaumont, P.W.R., "Direct Observation of the Fracture of CAS-Glass/SiC Composites - Part I: Delamination", *Journal of Materials Science*, **29**, pp. 3577-3856 (1994).

52) Worthem, D.W., and Ellis, J.R., "Thermomechanical Fatigue of Nicalon/CAS Under In-Phase and Out-of-Phase Cyclic Loadings", *Ceramic Engineering and Science Proceedings*, **14** [7-8], pp. 292-299 (1993).

53) Allen, R.F., and Bowen, P., "Fatigue and Fracture of a SiC/CAS Continuous Fibre Reinforced Glass Ceramic Matrix Composite at Ambient and Elevated Temperatures", *Ceramic Engineering and Science Proceedings*, **14** [7-8], pp. 265-272 (1993).

54) Chamberlain, A., Pharaoh, M.W., and Lewis, M.H., "Novel Silicate Matrices for Fibre Reinforced Ceramics", *Ceramic Engineering and Science Proceedings*, **14** [9-10], pp. 939-946 (1993).

55) Butkus, L.M., and Holmes, J.W., "Thermomechanical Fatigue Behavior of a Silicon Carbide Fiber-Reinforced Calcium Aluminosilicate Composite", *Journal of the American Ceramic Society*, **76** [11], pp. 2817-2825 (1993).

56) Weber, C.H., Löfvander, J.P.A., and Evans, A.G., "Creep Anisotropy of a Continuous-Fiber-Reinforced Silicon Carbide/Calcium Aluminosilicate Composite", *Journal of the American Ceramic Society*, **77** [7], pp. 1745-1752 (1994).

57) Avetikov, V.G., Zin'ko, F.T., and Zasedateleva, N.A., "High-Frequency Ceramics Based on Wollastonite", *Steklo Keram*, **17** [3], pp. 25-29 (1960).

58) Schwartz, B., "Review of Multilayer Ceramics for Microelectronic Packaging", *Journal of Physics and Chemistry of Solids*, **45** [10] pp. 1051-1068 (1984).

59) Goodwin, J.W., "Rheology of Ceramic Materials", *American Ceramic Society Bulletin*, **69** [10], pp. 1694-1698 (1990).

60) Blanc, R., "Rheology of Concentrated Dispersions", *Journal de Physique*, **47** [2] pp. C1/65 - C1/71 (1986).

61) Sacks, M.D., Khadilkar, C.S., Scheiffele, G.W., Shenoy, A.V., Dow, J.H., and Sheu, R.S., "Dispersion and Rheology in Ceramic Processing", from Advances in Ceramics,

Volume 21: Ceramic Powder Science, American Ceramic Society, Westerville, OH, pp. 495-515 (1987).

62) Barnes, H.A., Hutton, J.F., and Walters, K., "Rheology of Suspensions", Chapter 7 from An Introduction to Rheology, Elsevier Science Publishers, New York (1989).

63) Hirata, Y., Aksay, I.A., Kurita, R., Hori, S., and Kaji, H., "Processing of Mullite with Powders Processed by Chemical Vapor Deposition", from Ceramic Transactions - Volume 6: Mullite and Mullite Matrix Composites, American Ceramic Society, Westerville, OH (1990).

64) Hunter, R.J., "Rheological and Sedimentation Behavior of Strongly Interacting Colloidal Systems", from Modern Trends of Colloid Science in Chemistry and Biology, Birkhäuser Verlag Basel, Boston (1985).

65) van de Ven, T.G.M., and Mason, S.G., "The Microrheology of Colloidal Dispersions VII. Orthokinetic doublet formation of spheres", *Colloid and Polymer Science*, **255** [5], pp. 468-479 (1977).

66) Schilling, C.H., and Aksay, I.A., "Slip Casting", from Engineered Materials Handbook - Volume 4: Ceramics and Glasses, ASM International, Metals Park, OH (1992).

67) Schilling, C.H., and Aksay, I.A., "Slip Casting of Advanced Ceramics and Composites", from Transactions of the Canadian University - Industry Council on Advanced Ceramics (3rd Workshop), P.S. Nicholson (editor), February 24-25 (1987).

68) Novich, B.E., and Pyatt, D.H., "Consolidation Behavior of High-Performance Ceramic Suspensions", *Journal of the American Ceramic Society*, **73** [2], pp. 207-212 (1990).

69) Haerle, A.G., and Haber, R.A., "Real-time Monitoring of Cake Thickness During Slip Casting", *Journal of Materials Science*, **28**, pp. 5679-5683 (1993).

70) Roosen, A., and Bowen, H.K., "Influence of Various Consolidation Techniques on the Green Microstructure and Sintering Behavior of Alumina Powders", *Journal of the American Ceramic Society*, **71** [11], pp. 970-977 (1988).

71) Kim, J.-J., Kim, B.-K., Song, B.-M., Kim, D.-Y., and Yoon, D.N., "Effect of Sintering Atmosphere on Isolated Pores During the Liquid-Phase Sintering of MgO-$CaMgSiO_4$", *Journal of the American Ceramic Society*, **70** [10], pp. 734-737 (1987).

72) Campbell, D.E., and Hagy, H.E., "Glasses and Glass-Ceramics" Chapter 2 from CRC Handbook of Materials Science, CRC Press, Cleveland, OH, pp. 323-339 (1974).

73) Haber, R.A., and Anderson, R.M., "Engineering Properties of Glass-Matrix Composites", from Engineered Materials Handbook - Volume 4: Ceramics and Glasses, ASM International, Metals Park, OH (1992).

74) Marotta, A., Buri, A., and Branda, F., "Nucleation in Glass and Differential Thermal Analysis", *Journal of Materials Science*, **16**, pp. 341-344 (1981).

75) Ray, C.S., and Day, D.E., "Determining the Nucleation Rate Curve for Lithium Disilicate Glass by Differential Thermal Analysis", *Journal of the American Ceramic Society.*, **73** [2], pp. 439-442(1990).

76) Weinberg, M.C., "Interpretation of DTA Experiments Used for Crystal Nucleation Rate Determinations", *Journal of the American Ceramic Society,* **74** [8], pp. 1905-1909 (1991).

77) Henderson, D.W., "Thermal Analysis of Non-Isothermal Crystallization Kinetics in Glass Forming Liquids", *Journal of Non-Crystalline Solids*, **30**, pp. 301-315(1979).

78) Speyer, Thermal Analysis of Materials, Marcel Dekker Inc., New York (1994).

79) Todor, D.N., Thermal Analysis of Minerals, Abacus Press, Kent, UK (1976).

80) Smykatz-Kloss, W., Differential Thermal Analysis, Springer Verlag, New York (1974).

81) Mecholski, J.J., "Evaluation of Mechanical Property Testing Methods for Ceramic Matrix Composites", *American Ceramic Society Bulletin*, **65** [2], pp. 315-322 (1986).

82) Quinn, G.D., and Baratta, F., "Flexure Data - Can It Be Used for Ceramics Part Design?", *Advanced Materials & Processes*, [12] pp. 31-35 (1985).

83) Quinn, G.D., Salem, J., Bar-on, I., Cho, K., Foley, M., and Fang, H., "Fracture Toughness of Advanced Ceramics at Room Temperature", *Journal of Research of the National Institute of Standards and Technology*, **97** [5], pp. 579-607 (1992).

84) Anderson, R.M., "Testing Advanced Ceramics", *Advanced Materials & Processes*, [3], pp. 31-36 (1989).

85) Anstis, G.R., Chantikul, P., Lawn, B.R., and Marshall, D.B., "A Critical Evaluation of Indentation Techniques for Measuring Fracture Toughness: I, Direct Crack Measurements", *Journal of the American Ceramic Society*, **64** [9], pp. 533-538 (1981).

86) Ponton, C.B., and Rawlings, R.D., "Vickers Indentation Fracture Toughness Test - Part 1: Review of Literature and Formulation of Standardised Indentation Toughness Equations", *Materials Science and Technology*, **5** [9], pp. 865-872 (1989).

87) Ponton, C.B., and Rawlings, R.D., "Vickers Indentation Fracture Toughness Test - Part 2: Application and Critical Evaluation of Standardised Indentation Toughness Equations", *Materials Science and Technology*, **5** [10], pp. 961-975 (1989).

88) Evans, A.G., and Charles, E.A., *Journal of the American Ceramic Society*, **59** [7-8], pp. 371-372 (1976).

89) Lankford, J., *Journal of Materials Science Letters*, 1, pp. 493-495 (1984).

90) Miyoshi, T., Sagawa, N., and Sassa, T., *Transactions of the Japanese Society of Mechanical Engineering*, **51A**, p. 2489 (1989).

91) Marshall, D.B., and Evans, A.G., "Reply to Comment on Elastic/Plastic Indentation Damage in Ceramics: The Median/Radial Crack System", *Journal of the American Ceramic Society*, **64** [12], pp. C-182-183 (1981).

92) Overbeek, J.T.G., "Recent Developments in the Understanding of Colloid Stability", *Journal of Colloid Interface Science*, **58**, p.408 (1977).

93) Speers, R.A., Tung, M.A, Durance, T.D., and Stewart, G.G., "Colloidal Aspects of Yeast Flocculation: A Review", *Journal of the Institute of Brewing*, **98**, pp. 525-531 (1992).

94) van de Ven, T.G.M, "Basic Concepts of Colloid Science", lecture notes from: North American Societies of Rheology Short Course, October 21-22 (1989).

95) Holcomb, D.N., and Tung, M.A., "Rheology" excerpt from Encyclopedia of Food Science and Technology, John Wiley & Sons, New York (1991).

96) Ferguson, J., and Kemblowski, Z., "Suspensions", Chapter 6 from Applied Food Rheology, Elsevier Applied Science, London (1990).

97) Barnes, H.A., Hutton, J.F., and Walters, K., "Rheology of Suspensions", Chapter 7 from An Introduction to Rheology, Elsevier Science Publishers, New York (1989).

98) Steffe, J., Rheological Methods in Food Process Engineering, Freeman Press, East Lansing, MI (1992).

99) Levin, E.M., Robbins, C.R., and McMurdie, H.F., Phase Diagrams for Ceramists - 1969 supplement, American Ceramic Society, Columbus, OH, p.138 (1969).

100) German, R.M., "Fundamentals of Sintering", from Engineered Materials Handbook - Volume 4: Ceramics and Glasses, ASM International, Metals Park, OH (1992).

101) Kwon, O.-H., "Liquid-Phase Sintering", from Engineered Materials Handbook - Volume 4: Ceramics and Glasses, ASM International, Metals Park, OH (1992).

102) Marion, J.E., Hseuh, C.H., and Evans, A.G., "Liquid-Phase Sintering of Ceramics", *Journal of the American Ceramic Society*, **70** [10], pp. 708-713 (1987).

103) Kwon, O.-H., and Messing, G.L., "A Theoretical Analysis of Solution-Precipitation Controlled Densification During Liquid Phase Sintering", *Acta Metallurgica et Materialia*, **39** [9], pp. 2059-2068 (1991).

104) Cullity, B.D., Elements of X-ray Diffraction, 2nd edition, Addison-Wesley Publishing Company, Reading, MA (1978).

105) Weast, R.C. (editor), CRC Handbook of Chemistry and Physics, CRC Press, Boca Raton, FL (1988).

106) Babikov, O.I., Ultrasonics and its Industrial Applications, Consultants Bureau, New York (1960).

107) ASTM Committee C-28, "Standard Test Method for Flexural Strength of Advanced Ceramics at Ambient Temperature" from Annual Book of ASTM Standards: Vol. 15.01, C 1161-94, pp. 309-315 (1995).

108) Morrell, R., Handbook of Properties of Technical & Engineering Ceramics - Part 1: An Introduction for the Engineer and Designer, Her Majesty's Stationery Office, London (1989).

109) Rigney, D.A., Fundamentals of Friction and Wear of Materials, American Society for Metals, Metals Park, Ohio (1981).

110) Bryden, R.H., Dispersion Stability of Wollastonite-Ceramic Aqueous Suspensions, M.A.Sc. Thesis, Technical University of Nova Scotia, Halifax, NS (1993).

111) Bryden, R.H., and Caley, W.F., "Processing of an Alumina - Wollastonite Composite" in Proceedings of the 8th World Ceramics Congress, TECHNA Srl, Firenza, Italy (1995).

112) Ekdawi, N., and Hunter, R.J., "Sedimentation of Disperse and Coagulated Suspensions at High Particle Concentrations", *Colloids and Surfaces*, **15**, pp. 147-159 (1985).

113) Anon., More Solutions to Sticky Problems, Brookfield Corporation, rheometry manual (1985).

114) Moreno, R., "The Role of Slip Additives in Tape-Casting Technology: Part I - Solvents and Dispersants", *American Ceramic Society Bulletin*, **71** [10], pp. 1521-1531 (1992).

115) Kelso, J.F., and Ferrazzoli, T.A., "Effect of Powder Surface Chemistry on the Stability of Concentrated Aqueous Dispersions of Alumina", *Journal of the American Ceramic Society*, **72** [4], pp. 625-627 (1989).

116) Richards, V.L., "Adsorption of Dispersants on Zirconia Powder in Tape-Casting Slip Compositions", *Journal of the American Ceramic Society*, **72** [2], pp. 325-327 (1989).

117) Hirata, Y., Kamikakimoto, J., Nishimoto, A., and Ishihara, Y., "Interaction Between α-Alumina Surface and Polyacrylic Acid", *Journal of the Ceramic Society of Japan*, **100** [1], pp. 7-12 (1992).

118) Cesarano, J., and Aksay, I.A., "Processing of Highly Concentrated Aqueous α-Alumina Suspensions Stabilized with Polyelectrolytes" *Journal of the American Ceramic Society*, **71** [12], pp. 1062-1067 (1988).

119) Sheppard, L.M. (editor), Ceramic Source 1992-1993, Volume 8, American Ceramic Society, Westerville, OH (1992).

120) Konsztowicz, K.J., private communication (1991).

121) Malghan, S.G., Premachandran, R.S., and Pei, P.T., "Mechanistic Understanding of Silicon Nitride Dispersion Using Cationic and Anionic Polyelectrolytes", *Powder Technology*, **79**, pp. 43-52 (1994).

122) Premachandran, R.S., and Malghan, S.G., "Dispersion Characteristics of Ceramic Powders in the Application of Cationic and Anionic Polyelectrolytes", *Powder Technology*, **79**, pp. 53-60 (1994).

123) Griffiths, R., Calculations in Ceramics, MacLaren, London (1966).

124) Eriksson, G., and Pelton, A.D., "Critical Evaluation and Optimization of the Thermodynamic Properties and Phase Diagrams of the CaO-Al_2O_3, Al_2O_3-SiO_2, and CaO-Al_2O_3-SiO_2 Systems", *Metallurgical Transactions B*, **24B**, pp.807-816 (1993).

125) Dillinger, L., "Metallographic Preparation of Ceramic and Cermet Materials", *Met-Tips No. 19*, Leco Corporation, St. Joseph, MI (1983).

126) Lawn, B.R., and Marshall, D.B., "Hardness, Toughness, and Brittleness: An Indentation Analysis", *Journal of the American Ceramic Society*, **62** [7-8], pp. 347-350 (1979).

127) Requena, J., Moreno, R., and Moya, J.S., "Alumina and Alumina/Zirconia Multilayer Composites Obtained by Slip Casting", *Journal of the American Ceramic Society*, **72** [8], pp. 1511-1513 (1989).

128) Bryden, R.H., Konsztowicz, K.J., Caley, W.F., and Kingston, P.W., "Dispersion Stability of Alumina - Wollastonite Aqueous Suspensions", *Journal of Materials Science Letters*, **11**, pp. 1633-1635 (1992).

129) Morrell, R., "Group A9: Electrical and Engineering Alumina - Nominal Al_2O_3 content 80-86%", from Handbook of Properties of Technical & Engineering Ceramics - Part 2: Data Reviews - Section I: High Alumina Ceramics, Her Majesty's Stationery Office, London, pp. 223 (1989).

APPENDIX A - BASIC Programs

Note that these computer programs were written and compiled using Microsoft® QuickBasic 5.0, and successfully run on an IBM compatible 286/12 MHz/1 Mb/VGA.

Numerical Peak Integration

```
100 DIM x#(1500), y#(1500)
200 CLS
210 INPUT "enter input file: ", filein$
220 OPEN filein$ FOR INPUT AS #1
300 i% = 1
310 DO UNTIL EOF(1)
320 INPUT #1, x#(i%), y#(i%)
330 i% = i% + 1
340 LOOP
350 i% = i% - 1
400 PRINT "limits of integration"
410 INPUT "  Enter left x-axis limit:  ", leftlim#
420 INPUT "  Enter right x-axis limit: ", rightlim#
500 low# = 1E+30
510 high# = -1E+30
520 FOR j% = 1 TO i%
530 IF x#(j%) >= liftlim# AND x#(j%) < low# THEN
540 low# = x#(j%)
550 ml% = j%
560 END IF
570 IF x#(j%) <= rightlim# AND x#(j%) > high# THEN
580 high# = x#(j%): mr% = j%
590 END IF
600 NEXT j%
700 IF y#(ml%) >= y#(mr%) THEN
```

```
710 ylow% = mr%
720 ELSE
730 ylow% = ml%
740 END IF
800 accum# = 0
810 FOR j% = 1 TO i% - 1
820 IF x#(j%) >= x#(ml%) AND x#(j%) <= x#(mr%) THEN
830 rect# = (x#(j% + 1) - x#(j%)) * (y#(j%) - y#(ylow%))
840 tri# = .5 * (x#(j% + 1) - x#(j%)) * (y#(j% + 1) - y#(j%))
850 accum# = accum# + rect# + tri#
855 PRINT x#(j%), accum#
860 END IF
870 NEXT j%
900 xyz# = (ABS(x#(ml%) - x#(mr%)) * ABS(y#(ml%) - y#(mr%)) * .5)
910 area = accum# - xyz#
1000 PRINT ""
1010 PRINT "peak area:  "; area
1020 CLOSE #1
1030 END
```

Numerical First-Derivative Program

```
100 DIM x#(1500), y#(1500)
200 CLS
300 INPUT "Enter input filename: ", fin$
400 INPUT "enter output filename: ", fout$
500 OPEN fin$ FOR INPUT AS #1
600 OPEN fout$ FOR OUTPUT AS #2
1000 i% = 1
1010 DO UNTIL EOF(1)
1015 x#(i%) = 0: y#(i%) = 0
1020 INPUT #1, x#(i%), y#(i%)
1030 i% = i% + 1
1040 LOOP
1050 i% = i% - 1
1100 '
1110 PRINT ""
1120 INPUT "Enter numer of points to be averaged: ", pts%
1130 IF pts% / 2 = INT(pts% / 2) THEN
1140 PRINT "value needs to be an odd number"
1150 GOTO 1100
1160 END IF
1170 p = pts%
```

```
1190 '
1300 h% = (pts% - 1) / 2
1310 FOR J% = h% + 1 TO i% - h%
1320 sumx# = 0: sumy# = 0: sumxy# = 0: sumx2# = 0
1330 FOR k% = J% - h% TO J% + h%
1340 sumx# = sumx# + x#(k%)
1350 sumy# = sumy# + y#(k%)
1360 sumxy# = sumxy# + x#(k%) * y#(k%)
1370 sumx2# = sumx2# + x#(k%) ^ 2
1380 NEXT k%
1390 slope = (sumxy# - (sumx# * sumy#) / p) / (sumx2# - (sumx# ^ 2) / p)
1400 WRITE #2, x#(J%), y#(J%), slope
1410 NEXT J%
1430 '
1500 CLOSE #1
1510 CLOSE #2
1999 END
```

Brookfield LVTD-II Data Input Program

```
120 CLS : SCREEN 12
125 t = 0: e = 0: DIM a(5000): DIM B(5000): DIM c(5000): DIM g(5000): DIM vi(500):
    DIM si(500): DIM ri(500)
126 DIM so(500): DIM ro(500): DIM vo(500): DIM dt(500): DIM ssx(5000)
127 DIM sro(500): DIM sssdo(100): GOTO 190
128 LOCATE 6, 8: PRINT
    "═══════════════════════════════════════════════════════════
    ═══════"
129 LOCATE 7, 8: PRINT "|                                                    |"
130 LOCATE 8, 8: PRINT "|    Brookfield Viscometer LVTDV-II  Data Collection
    Program    |"
132 LOCATE 9, 8: PRINT "|                                                    | "
134 LOCATE 10, 8: PRINT "| Licensed to TUNS Dept of Mining and Metallurgical
    Engineering |"
135 LOCATE 11, 8: PRINT "|                                                    |"
136 LOCATE 12, 8: PRINT "|                        by                          |"
137 LOCATE 13, 8: PRINT "|                                                    |"
138 LOCATE 14, 8: PRINT "|                    Ray Bryden                      |"
140 LOCATE 15, 8: PRINT "|                                                    |"
```

```
142 LOCATE 16, 8: PRINT
        "═══════════════════════════════════════════════════════════
        ═══════"
145 FOR q = 0 TO 500
146 ssx(q) = 0
147 NEXT q
180 CLS
190 f$ = "c:\visc\test.prn"
222 GOSUB 1000
225 OPEN "com2:1200,n,7,2,cs0,ds0,cd" FOR RANDOM AS #1
226 OPEN f$ FOR OUTPUT AS #2
227 TIMER ON
228 start = TIMER
230 ds$ = "": x = 0: y = 1: lold = 220: l = 0: o = 0: zh = 1: hoff = 1: ww = 1: ee = 0: j = 0:
        ff = 1
231 WHILE k$ <> CHR$(27): KEY(1) ON: KEY(10) ON: KEY(8) ON: KEY(3) ON:
        KEY(4) ON: KEY(7) ON: KEY(6) ON: KEY(30) ON: KEY(31) ON: KEY(5)
        ON
232 ON KEY(5) GOSUB 234
233 GOTO 236
234 ff = 1: RETURN
236 ON KEY(1) GOSUB 1500
237 ON KEY(10) GOSUB 1000
```

```
238 ON KEY(8) GOSUB 2000
239 ON KEY(3) GOSUB 241
240 GOTO 244
241 zh = -1: hoff = 0: RETURN
243 ON KEY(4) GOSUB 245
244 GOTO 246
245 zh = 1: hoff = 1: RETURN
246 ON KEY(6) GOSUB 248
247 GOTO 249
248 ww = 1
249 ON KEY(7) GOSUB 251
250 GOTO 252
251 ww = 0: ff = 0
252 IF EOF(1) THEN 450
253 WHILE LOC(1) < 40
254 WEND
255 ds$ = INPUT$(LOC(1), #1)
260 ds$ = RIGHT$(ds$, LEN(ds$) - 1)
265 lf = INSTR(ds$, CHR$(10))
270 IF lf THEN ds$ = LEFT$(ds$, lf - 1) + MID$(ds$, lf + 1)
310 w$ = MID$(ds$, 7, 1): IF w$ <> "%" THEN CLOSE #1: CLOSE #2: SOUND 200,
        9: LOCATE 1, 10: PRINT "Please wait ...": GOTO 225
315 tor = VAL(MID$(ds$, 3, 4))
```

```
320 cpv$ = MID$(ds$, 9, 4)
325 cpe$ = MID$(ds$, 14, 1)
330 cps$ = STR$(VAL(cpv$) * 10 ^ VAL(cpe$))
335 cps = VAL(RIGHT$(cps$, LEN(cps$) - 1))
340 shv$ = MID$(ds$, 18, 4)
345 she$ = MID$(ds$, 23, 1)
350 shs$ = STR$(VAL(shv$) * 10 ^ VAL(she$))
355 shs = VAL(RIGHT$(shs$, LEN(shs$) - 1))
360 rpm = VAL(MID$(ds$, 27, 3))
365 mdl$ = MID$(ds$, 34, 2)
370 spd = VAL(RIGHT$(ds$, 2))
371 ON KEY(30) GOSUB 373
372 GOTO 374
373 ee = 1
374 ON KEY(31) GOSUB 376
375 GOTO 377
376 ee = 0
377 d = TIMER - start: IF (sold + d) > 600 THEN sold = 0: o = 4
378 s = sold + d
380 a = 15: IF tor < 10 THEN a = 14: IF o = 4 THEN a = 10
382 IF (d - 1) > 60 / (rpm + .000000001#) AND d > 61 THEN SOUND 750, 2
385 IF (d - 1) > 60 / (rpm + .000000001#) AND n = 1 AND d > 61 THEN GOSUB 1500
388 IF rpm <> rpmold THEN GOSUB 600
```

```
390 zh = zh + 1: IF zh = 0 AND hoff = 0 THEN GOSUB 2500
391 IF zh > 3 THEN zh = -1
392 IF ee = 1 THEN SOUND (tor + 11) * 10, 4
396 IF j = 1 THEN j = 0: GOTO 400
398 IF (ww = 1 OR ff = 1) AND d > 7 THEN GOSUB 3000
400 l = 20 + (1 - tor / 100) * 200
405 LINE (20 + s, l)-(20 + s, lold), a
410 LOCATE 1, 8: PRINT "data string : "; ds$; "    t :"; INT(d * 10) / 10; "sec  "
415 rpmold = rpm: visold = cps: torold = tor: shsold = shs: lold = l
435 ds$ = ""
450 k$ = INKEY$
455 WEND
460 CLOSE #1
462 CLOSE #2
465 CLS
470 LOCATE 12, 32
475 PRINT "Program stopped": KEY(1) OFF: KEY(10) OFF
480 END
600 start = TIMER: sold = s
610 n = 1: j = 1
615 LINE (s + 18, 223 + o)-(s + 22, 232 + o), 0, BF
620 LINE (s + 19, 224 + o)-(s + 21, 231 + o), 11 + o, BF
680 RETURN
```

```
1000 CLS : COLOR 7
1005 LINE (24, 24)-(628, 228), 1, BF: LINE (18, 18)-(622, 222), 8, BF
1010 LINE (18, 18)-(622, 222), 7, B
1012 FOR x = 0 TO 10
1014 LINE (20, 20 + x * 20)-(620, 20 + x * 20), 1, , &HA0A
1016 NEXT x
1030 FOR x = 0 TO 5
1040 LINE (20 + x * 120, 21)-(20 + x * 120, 220), 12, , &HA0A0
1050 NEXT x
1070 FOR x = 0 TO 5
1090 LINE (80 + x * 120, 21)-(80 + x * 120, 220), 14, , &HA0A
1110 NEXT x
1115 LINE (26, 266)-(326, 466), 4, BF: LINE (19, 259)-(321, 461), 7, B
1120 LINE (20, 260)-(320, 460), 0, BF
1123 CIRCLE (16, 475), 3, 15, , , 2: CIRCLE (21, 477), 1, 15: LINE (23, 473)-(25, 471),
        15: LINE (25, 471)-(25, 478), 15
1125 LINE (120, 471)-(120, 478), 15: LINE (118, 473)-(120, 471), 15
1130 LINE (216, 473)-(218, 471), 15: LINE (218, 471)-(218, 478), 15: CIRCLE (224,
        475), 3, 15, , , 2
1132 LINE (313, 473)-(315, 471), 15: LINE (315, 471)-(315, 478), 15: CIRCLE (321,
        475), 3, 15, , , 2: CIRCLE (327, 475), 3, 15, , , 2
1140 FOR x = 0 TO 4
1150 LINE (20, 260 + x * 50)-(320, 260 + x * 50), 7, , &HA0A
```

```
1160 NEXT x
1163 FOR x = 0 TO 3
1165 FOR y = 2 TO 9
1170 LINE (20, 260 + x * 50 + (1 - (LOG(y)) / 2.303) * 50)-(320, 260 + x * 50 + (1 -
        (LOG(y)) / 2.303) * 50), 8
1175 NEXT y
1180 NEXT x
1182 FOR x = 0 TO 3
1183 FOR y = 2 TO 9
1185 LINE (20 + x * 100 + ((LOG(y)) / 2.303) * 100, 260)-(20 + x * 100 + ((LOG(y)) /
        2.303) * 100, 460), 8
1187 NEXT y
1188 NEXT x
1190 FOR x = 0 TO 3
1200 LINE (20 + x * 100, 260)-(20 + x * 100, 460), 7, , &HA0A
1210 NEXT x
1213 LINE (355, 242)-(626, 265), 5, BF: LINE (349, 236)-(620, 259), 0, BF
1215 LINE (347, 236)-(620, 259), 7, B
1225 LINE (355, 270)-(626, 469), 5, BF: LINE (349, 264)-(620, 463), 0, BF
1230 LINE (347, 264)-(620, 463), 7, B
1240 LOCATE 4, 1: PRINT "%"
1250 LOCATE 6, 1: PRINT "T"
1260 LOCATE 7, 1: PRINT "o"
```

```
1270 LOCATE 8, 1: PRINT "r"
1280 LOCATE 9, 1: PRINT "q"
1290 LOCATE 10, 1: PRINT "u"
1300 LOCATE 11, 1: PRINT "e"
1304 LOCATE 16, 45: PRINT "SR     Visc     SS     st dev  t"
1306 LINE (146, 242)-(146, 248), 14: LINE (212, 242)-(212, 248), 10
1308 LINE (137, 245)-(155, 245), 3: LINE (203, 245)-(221, 245), 4
1310 LOCATE 16, 3: PRINT "Viscosity [cps]"
1320 LINE (1, 308)-(3, 307), 15: LINE (3, 307)-(3, 313), 15: CIRCLE (11, 310), 3, 15, , ,
     2: CIRCLE (7, 310), 3, 15, , , 2: CIRCLE (15, 310), 3, 15, , , 2
1322 LINE (13, 458)-(15, 456), 15: LINE (15, 456)-(15, 463), 15
1323 LINE (8, 408)-(10, 407), 15: LINE (10, 407)-(10, 413), 15: CIRCLE (14, 410), 3,
     15, , , 2
1324 LINE (4, 358)-(6, 357), 15: LINE (6, 357)-(6, 363), 15: CIRCLE (14, 360), 3, 15, , ,
     2: CIRCLE (10, 360), 3, 15, , , 2
1325 LOCATE 16, 30: PRINT "Sh-Str [mPa]"
1350 LOCATE 28, 4: PRINT "Sh-Rate [1/s] " + CHR$(26)
1360 c = 0: p = 0: sold = 0
1362 LOCATE 5, 80: PRINT "B"
1364 LOCATE 6, 80: PRINT "r"
1366 LOCATE 7, 80: PRINT "o"
1368 LOCATE 8, 80: PRINT "o"
1370 LOCATE 9, 80: PRINT "k"
```

```
1372 LOCATE 10, 80: PRINT "f"
1374 LOCATE 11, 80: PRINT "i"
1376 LOCATE 12, 80: PRINT "e"
1378 LOCATE 13, 80: PRINT "l"
1380 LOCATE 14, 80: PRINT "d"
1382 LOCATE 16, 80: PRINT "D"
1384 LOCATE 17, 80: PRINT "V"
1386 LOCATE 19, 80: PRINT "I"
1388 LOCATE 20, 80: PRINT "I"
1410 RETURN
1500 sf = 1.32
1530 IF spd = 25 THEN sf = .22
1540 IF spd = 31 THEN sf = .34
1550 IF spd = 34 THEN sf = .28
1560 sr = sf * rpm: IF sr <= .102 THEN sr = .102
1561 IF d < 10 THEN 1578
1562 ssa = 0: ssd = 0: kk = 0
1563 FOR q = 10 TO d
1565 ssa = ssa + ssx(q): kk = kk + 1
1566 NEXT q
1567 ssa = ssa / kk
1568 FOR q = 10 TO d
1570 ssd = ssd + (ssx(q) - ssa) ^ 2
```

```
1572 NEXT q
1574 sssd = (ABS(ssd) / (kk - 1)) ^ .5
1576 shsa = ssa: cpsa = ssa * 100 / sr
1577 IF ssa < .1 THEN cpsa = .1: ssa = .1
1578 logsr = LOG(sr) / 2.303
1580 logv = LOG(cpsa) / 2.303
1590 logss = LOG(shsa * 100) / 2.303: BEEP
1595 GOTO 1620
1600 CIRCLE ((20 + (logsr + 1) * 100), (260 + (1 - logv / 4) * 200)), 3, 7
1610 CIRCLE ((20 + (logsr + 1) * 100), (260 + (1 - logss / 4) * 200)), 2, 10
1620 LINE (16 + s, l - 5)-(24 + s, l + 5), 13, B
1630 LOCATE 18 + c, 45: PRINT "                    "
1650 LOCATE 18 + c, 45: PRINT INT(sr * 100) / 100: LOCATE 18 + c, 51: PRINT
     INT(cpsa * 10) / 10
1652 LOCATE 18 + c, 58: PRINT INT(shsa * 1000) / 10: LOCATE 18 + c, 66: PRINT
     INT(sssd * 1000) / 10: LOCATE 18 + c, 73: PRINT INT(d)
1660 c = c + 1: p = p + 1: IF c > 10 THEN c = 0
1662 ro(p) = shsa: vo(p) = cpsa: so(p) = INT(shsa * 10000) / 100: dt(p) = d: sro(p) = sr:
     sssdo(p) = sssd
1665 vi(p) = 260 + (1 - logv / 4) * 200: ri(p) = 20 + (logsr + 1) * 100: si(p) = 260 + (1 -
     logss / 4) * 200
1668 n = 0: PRINT #2, p; sro(p), INT(vo(p) * 100) / 100; INT((sssdo(p) / sro(p)) *
     10000) / 100, so(p); INT(sssdo(p) * 10000) / 100, INT(dt(p) * 10) / 10
```

```
1670 IF p = 1 THEN 1800
1673 IF ri(p) < ri(p - 1) AND (ABS(ri(p) - ri(p - 1))) > 80 THEN 1800
1675 IF (ABS(ri(p) - ri(p - 1))) > 80 THEN 1800
1680 LINE (ri(p), vi(p))-(ri(p - 1), vi(p - 1)), 3
1690 LINE (ri(p), si(p))-(ri(p - 1), si(p - 1)), 4
1800 RETURN
2000 FOR q = 1 TO p
2010 PRINT #2, q, ro(q), vo(q), so(q), INT(dt(q) * 10) / 10: BEEP
2020 NEXT q: PRINT #2, "end of data": PRINT #2,
2030 RETURN
2500 sf = 1.32
2530 IF spd = 25 THEN sf = .22
2540 IF spd = 31 THEN sf = .34
2550 IF spd = 34 THEN sf = .28
2560 sr = sf * rpm: IF sr <= .102 THEN sr = .102
2562 IF cps <= 1.01 THEN cps = 1.01
2564 IF shs <= .01 THEN shs = .01
2570 logsr = LOG(sr) / 2.303
2580 logv = LOG(cps) / 2.303
2590 logss = LOG(shs * 100) / 2.303: BEEP
2650 LOCATE 18 + c, 46: PRINT p + 1: LOCATE 18 + c, 50: PRINT ": "; INT(sr * 100)
     / 100
2652 LOCATE 18 + c, 60: PRINT cps: LOCATE 18 + c, 68: PRINT shs * 100: LOCATE
     18 + c, 73: PRINT INT(d)
```

```
2660 c = c + 1: p = p + 1: IF c > 10 THEN c = 0
2662 ro(p) = shs: vo(p) = cps: so(p) = shs: dt(p) = d
2665 vi(p) = 260 + (1 - logv / 4) * 200: ri(p) = 20 + (logsr + 1) * 100: si(p) = 260 + (1 -
     logss / 4) * 200
2668 n = 0
2670 IF p = 1 THEN 2800
2680 ON KEY(4) GOSUB 2700
2690 GOTO 2800
2700 hoff = 1
2800 RETURN
3000 sf = 1.32
3030 IF spd = 25 THEN sf = .22
3040 IF spd = 31 THEN sf = .34
3050 IF spd = 34 THEN sf = .28
3060 sr = sf * rpm: IF sr <= .102 THEN sr = .102
3062 IF cps <= 1.01 THEN cps = 1.01
3064 IF shs <= .01 THEN shs = .01
3066 ssx(d) = shs
3070 logsr = LOG(sr) / 2.303
3080 logv = LOG(cps) / 2.303
3090 logss = LOG(shs * 100) / 2.303
3093 IF rpm < .2 THEN 3200
3095 IF ff = 1 THEN 3100
```

```
3098 GOTO 3105
3100 LINE ((18 + (logsr + 1) * 100), (260 + (1 - logv / 4) * 200))-((19 + (logsr + 1) *
100), (260 + (1 - logv / 4) * 200)), 14
3105 IF ww = 1 THEN 3110
3108 GOTO 3200
3110 LINE ((20 + (logsr + 1) * 100), (260 + (1 - logss / 4) * 200))-((21 + (logsr + 1) *
        100), (260 + (1 - logss / 4) * 200)), 10
3200 RETURN
```

IMAGE EVALUATION
TEST TARGET (QA-3)

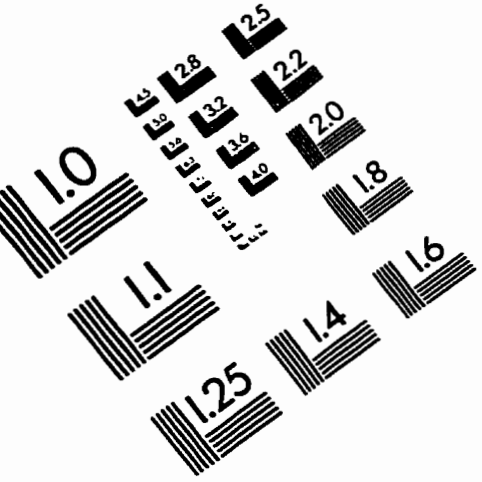

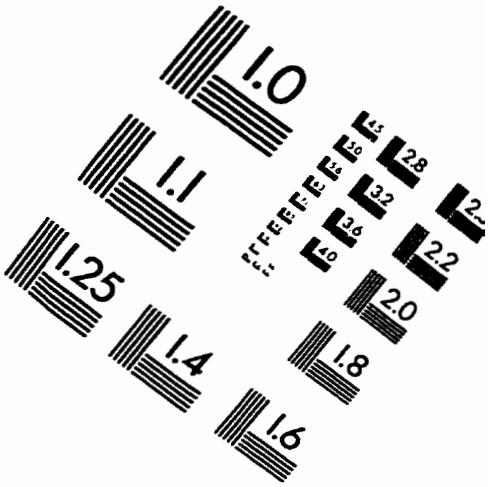

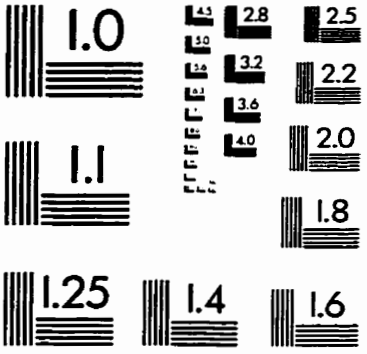

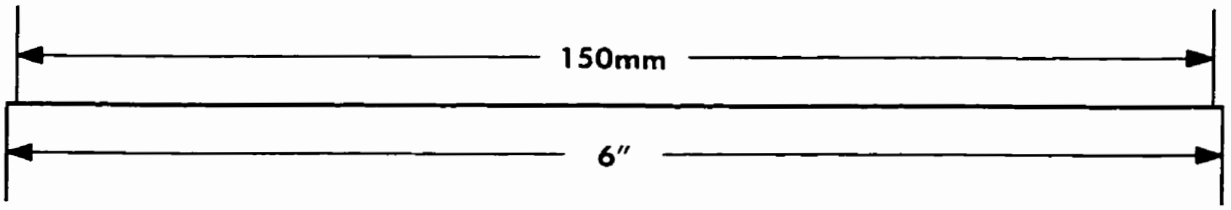

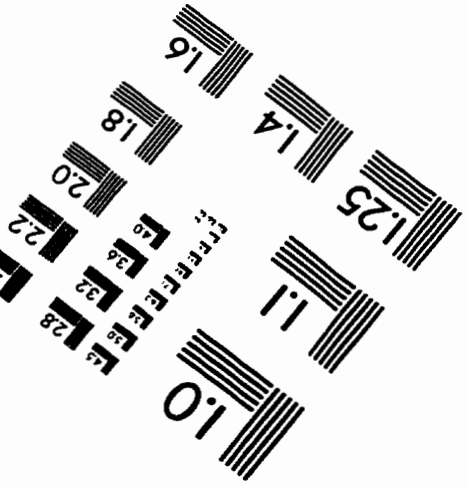

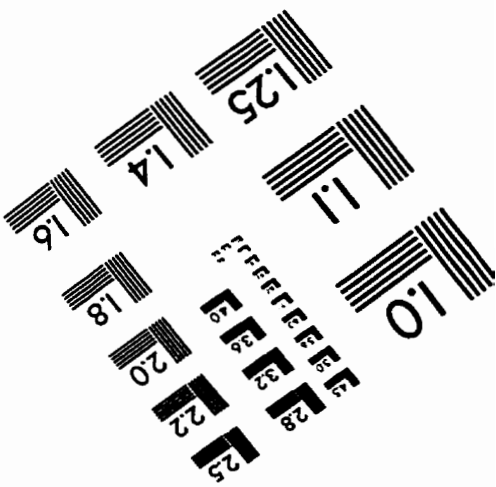

APPLIED IMAGE, Inc
1653 East Main Street
Rochester, NY 14609 USA
Phone: 716/482-0300
Fax: 716/288-5989